LARGE-EDDY SIMULATIONS OF WIND FARMS UNDER DIFFERENT ATMOSPHERIC STRATIFICATION CONDITIONS

by

Gerard Cortina Marín

A dissertation submitted to the faculty of
The University of Utah
in partial fulfillment of the requirements for the degree of

Doctor of Philosophy

Department of Mechanical Engineering

The University of Utah

May 2018

The University of Utah Graduate School

STATEMENT OF DISSERTATION APPROVAL

The dissertation of **Gerard Cortina Marín**
has been approved by the following supervisory committee members:

Marc Calaf ,	Chair(s)	**06 Dec 2017** Date Approved
Eric R. Pardyjak ,	Member	**06 Dec 2017** Date Approved
Meredith M. Metzger ,	Member	**06 Dec 2017** Date Approved
James R. Stoll II ,	Member	**06 Dec 2017** Date Approved
Raúl B. Cal ,	Member	**06 Dec 2017** Date Approved

by **Tim Ameel** , Chair/Dean of
the Department/College/School of **Mechanical Engineering**
and by **David B. Kieda** , Dean of The Graduate School.

ABSTRACT

The continuous growth in energy demand together with the awareness of greenhouse gases and their implication on climate change has pushed our society to design new environmentally sustainable sources of energy. An example of this is the rapid growth that wind and solar energy production has experienced, thanks to the installation of large wind and solar farms. As a result of their large dimensions and their corresponding mechanisms to harvest energy, these energy systems are prone to interact with the atmospheric boundary layer, which is defined as the lowest part of the troposphere that is directly influenced by the presence of the earth surface, and therefore, it directly influences the energy harvesting of large scale wind farms. Hence, understanding the interaction mechanisms between wind farms and the atmospheric boundary layer is of crucial importance to properly determine their optimal performance. Specifically, this work focuses on the development of new understanding regarding wind energy and its interaction with the atmospheric boundary layer, with the main goal to help in developing more efficient wind energy harvesting systems. In detail the objectives of my PhD work are: (i) create new understanding regarding wind turbines' inflow as it relates with time alignment of the turbines; (ii) determine the dominant turbine wake recovery processes under different atmospheric stratification conditions; (iii) develop a useful analytical predictor model to estimate large scale wind farms power output. These objectives will be met through four specific tasks that comprise Chapters 2 to 5 of this dissertation. High-resolution numerical simulations of the atmospheric boundary layer are used in all tasks.

For my wife Alba, my parents Teresa and Jordi my brother Marc, and all my family and friends.

CONTENTS

LIST OF FIGURES

LIST OF TABLES

ACKNOWLEDGEMENTS

After an intensive period of five years, today is the day: writing this note of thanks is the finishing touch on my dissertation. Writing this dissertation has had a big impact on me, which I would like to reflect next on the people who have supported and helped me so much throughout this period:

First of all, my sincere gratitude to my advisor Marc Calaf for his patient guidance, encouragement and advice he has provided throughout my time as his student. You have set an example of excellence as a researcher, mentor, instructor, and role model. I feel honored to have worked with Marc. Continuous support of my PhD study and research, for his motivation, enthusiasm, and immense knowledge. I could not have imagined having a better advisor and mentor for my PhD study. It has been a period of intense learning for me, not only in the scientific arena, but also on a personal level. My sincere thanks also goes to Dr. Ral Bayon Cal: your tireless work ethic, curiosity, concern for others and sincerity have been an example to me. Your attention to detail and sincere concern for my well-being helped me to become a much more capable researcher. Your friendship was an invaluable asset throughout the consecution of our research work, numerous meetings and academic discussions. Besides my advisor and Dr. Cal, I would like to thank the rest of my thesis committee, Dr. Eric Pardyjak, Dr. Rob Stoll and Dr. Meredith Metzger. Special thanks also for Dr. Metzger and Dr. Pardyjak for the collaboration, academic discussions and invaluable assets throughout the consecution of our experimental research project conducted in Colorado with collaboration of the NREL national laboratory. Moreover I would like to thank Dr. Ashley Spear and Jeppesen Feliciano for the collaborative project that we developed during the lasts months, not included in this dissertation but also with high impact on structural analysis in wind turbines. During these years, I was teacher assistant in five courses taught by Prof. Rob Stoll, Prof. Henry Fu and Prof. Marc Calaf. All of them have been amazing instructors and great mentors. I want to thank Prof. Peters for her constant enthusiasm and encouragement.

I also had the privilege to work with Varun Sharma and Fabien Margairaz and benefited from his valuable inputs on the research topics that we worked together; his discussions, ideas, and feedbacks have been absolutely invaluable. I thank my fellow labmates: Fabien, Travis, Byron, Jeppesen, Yohhan, Nipun, Derek, Chao, Alexei, Emina, Lam and others who have been visiting temporally. To Naseem Ali, I miss our interesting and long-lasting chats, for the stimulating discussions, for the sleepless nights we were working together, and for all the fun we have had in the last years and Christmas in Portland. Also, I would like to thank my friends in Catalonia for supporting the fact that I had to leave them for several years and miss so many times together and at the same time apologize for not being there for very important times for us and our country. I also thank their insistence in asking me year over year when would I come back definitively and encouraging me to finish my PhD the soonest the best in order to get back home: Anna Argelaguer, Pep Arqu, Guillem Casacuberta, Nria Casals, Mart Feliu, Marc Font, Gerard Iglesias, David Masachs, David Saborido, Anna Simon, and Oriol Trasserra. And finally, last but by no means least, I want to express gratitude for the support received by all my family. My forever interested, encouraging and always enthusiastic wife. Your love, advice and constant support have made my PhD possible.

This work would not have been possible without the financial support of the start-up funds provided by the Mechanical Engineering Department at University of Utah to Assistant Professor Marc Calaf. I am also grateful to the GCSC for providing me funding for attending a wind energy conference celebrated in Dallas, Texas 2016.

Thanks for all your encouragement!

CHAPTER 1

INTRODUCTION

Over the past 10 years wind energy harvesting has experienced a rapid growth, with an overall installed global power increase of a factor of five between 2002 and 2009 (see the latest special IPCC report [20]). Throughout this time wind turbine designs have evolved, with increases in rotor diameter and overall efficiency designs. By 2009 most wind turbines had a $\sim 70 - 80$ meter rotor diameter. Now rotor diameter designs are approaching 190 meters. Engineering improvements have accompanied the development of the massive rotors. However, the way in which wind turbines obtain in-situ meteorological information remains the same - traditional wind vanes and cup anemometers are installed at the turbine's nacelle, right behind the blades. The orientation and other operating parameters of the turbine are governed by these two wind measurements through the use of a control loop. These wind measurements have important drawbacks, especially with increasing rotor diameters: 1) since the velocity is measured at a single point immediately behind the blades, turbine misalignment with the mean wind direction is common, inducing energy losses up to 10% [13]; and 2) the near-blade monitoring does not provide time to adjust the operating parameters of the wind turbine to account for changes in the approaching wind flow. This latency in adjusting to ambient wind direction and speed subjects the blades and turbine structure to unanticipated wind gusts or extreme incoming wind conditions. These velocity aberrations induce increased loading, structural fatigue, power train failures and associated increases in maintenance costs. A solution is to install forward directed wind LIDARs (Light Detection and Ranging) on the turbines' nacelles. The continuous improvement of LIDAR technology over the past few years, with enhanced spatio-temporal resolution, improved signal-to-noise ratio, and considerable reduction of the physical package, has made this technology very appealing for wind energy applications. For example, several studies have illustrated the LIDARs' capacity to

provide more accurate measures of the turbine's approaching wind vector in comparison to traditional wind vane and cup anemometers [7, 13]. With this new capacity of staring ahead of the turbine's rotor blades, it is possible to improve the turbine's yaw alignment [16, 1], and therefore enhance the turbine's harvested power [7, 15]. In addition, wind LIDARs have also improved the measure of power curves [12, 19] and the prediction of incoming flow turbulence [9], which results in a potential mitigation of the turbines' loads. Wind LIDAR systems, however, are optimized to measure over a fixed upwind range, but "At what upwind distance should they interrogate the atmosphere?" and "What is the optimal average time in which to learn about the incoming flow conditions?"

A second goal of this research is to determine how the changes of the upwind turbulent flow can be reliably sensed by wind LIDARs according to the location of the turbine. Either it is located standing alone or within a large wind farm. The use of wind LIDARs to detect incoming wind gusts will allow control of the blade pitch to feather the blades to protect the wind turbine from extreme structural loading and therefore reduce maintenance cost. This analysis will facilitate determining the upstream ranging under specific meteorological conditions. For example, in order to study the detection of wind gusts, Harris et al. [9] installed a wind LIDAR on the nacelle of a 2.3 MW turbine. The wind measurements were performed at a constant upstream scanning distance of 200 meters for a period of 18 hours. By comparing the LIDAR measurements with those provided by cup anemometers, they illustrated the potential of nacelle-mounted wind LIDARs to accurately measure incoming wind gusts. By being able to measure the incoming flow ahead of time, it is, for example, possible to design control mechanisms that force certain wind turbines of a wind farm to be purposely yaw-misaligned, reducing the wake-to-wake interaction with downstream turbines [10]. This is for example the purpose of the control-oriented dynamic model proposed by Gebraad and Van Wingerden [8], or the approach explored by the National Renewable Energy Laboratory (NREL) at the Fishermens Atlantic City Windfarm. In this last case, an increase of 10% in power output for the overall wind farm and a reduction in successive wake-turbine interactions were reported [6]. According to Mikkelsen et al. [13], the 'warning' time for the incoming winds gusts is of 5 to 10 seconds, depending on the mean incoming wind velocity. Therefore, the potential of using wind LIDARs to predict the incoming turbulent flow relies on the time-lapse with which turbulent events can be

predicted before these reach the turbine blades. At this point, while the LIDAR-assisted collective pitch control and the pitching system have been proved to be fast enough to regulate the wind turbine settings [14], several questions remain to be answered with respect to the evolution of the turbulent flow within wind farms. For example, how far upstream should the wind LIDARs measure to observe rotor-disk correlated turbulence? and how does this upstream correlation distance change with atmospheric stratification?

Another approach to enhance the wind farm power production is by designing better wind farm layouts. For this reason, this work also focuses on the wake recovery mechanisms. For example, in a very large wind farm a fully developed turbulent flow develops, in which the statistical properties of the flow do not change within the horizontal direction and thus relevant changes mostly occur in the vertical direction. Within this region, the so called *"wind turbine array boundary layer"* (WTABL), the recovery of the successive turbine-generated wakes is only a result of vertical entrainment of mean kinetic energy (MKE) as shown by Lu and Porté-Agel [11], Yang et al. [21], VerHulst and Meneveau [17], Abkar and Porté-Agel [2], which is a function of the wind farm arrangement [3]. This mechanism determines the overall efficiency of the farm as numerically shown in VerHulst and Meneveau [18] for a pressure-driven flow without thermal stratification, in Calaf et al. [5] for a neutrally stratified atmospheric flow, and experimentally in Cal et al. [4]. Moreover, we want to create new knowledge regarding the differences in wake recovery process in an isolated turbine in comparison to a turbine within a large wind farm, and for wind farms with different densities (wind farms with more or fewer wind turbines). From these results, we can formulate a model to forecast the wind farms' harvested power as a function of the thermal stratification and the wind farm density. This model has the potential to be employed as an order of magnitude estimation tool. Also, it could help quickly determine the optimal number of wind turbines that a wind farm should include, or even it could be used to determine the number of wind turbines of an existing wind farm that should be disconnected to optimize the harvested power as a function of the atmospheric stability. High-resolution large eddy simulations (LES) of the atmospheric boundary layer (ABL) flow are used to solve the specific questions stated herein.

1.1 References

[1] *Improving Yaw Alignment Using Spinner Based LIDAR*, AIAA Aerospace Sciences Meeting including the New Horizons Forum and Aerospace Exposition (2011), pp. 1–13.

[2] M. Abkar and F. Porté-Agel, *The effect of free-atmosphere stratification on boundary-layer flow and power output from very large wind farms*, Energies, 6 (2013), pp. 2338–2361.

[3] M. Abkar and F. Porte-Agel, *Mean and turbulent kinetic energy budgets inside and above very large wind farms under conventionally-neutral condition*, Renewable Energy, 70 (2014), pp. 142–152.

[4] R. B. Cal, J. Lebrón, L. Castillo, H. S. Kang, and C. Meneveau, *Experimental study of the horizontally averaged flow structure in a model wind-turbine array boundary layer*, Journal of Renewable and Sustainable Energy, 2 (2010), p. 013106.

[5] M. Calaf, C. Meneveau, and J. Meyers, *Large eddy simulation study of fully developed wind-turbine array boundary layers Large eddy simulation study of fully developed wind-turbine array*, Physics of Fluids, 22, 015110 (2010).

[6] M. J. Churchfield, P. Fleming, B. Bulder, S. M. White, et al., *Wind turbine wake-redirection control at the fishermen's atlantic city windfarm*, Offshore Technology Conference, 2015.

[7] P. a. Fleming, a.K. Scholbrock, a. Jehu, S. Davoust, E. Osler, a.D. Wright, and a. Clifton, *Field-test results using a nacelle-mounted lidar for improving wind turbine power capture by reducing yaw misalignment*, Journal of Physics: Conference Series, 524 (2014), p. 012002.

[8] P. M. O. Gebraad and J. W. van Wingerden, *A control-oriented dynamic model for wakes in wind plants*, Journal of Physics: Conference Series, 524 (2014), p. 012186.

[9] M. Harris, D. Bryce, A. Coffey, D. Smith, J. Birkemeyer, and U. Knopf, *Advance measurements of gusts by laser anemometry.*, Wind Engineering and Industrial Aerodynamics, 95 (2007), pp. 1637–1647.

[10] K. A. Kragh and M. H. Hansen, *Load alleviation of wind turbines by yaw misalignment*, Wind Energy, (2014), pp. 17:971–982.

[11] H. Lu and F. Porté-Agel, *On the impact of wind farms on a convective atmospheric boundary layer*, Boundary-Layer Meteorology, 157 (2015), pp. 81–96.

[12] J. Medley, W. Barker, M. Harris, M. Pitter, C. Slinger, T. Mikkelsen, and M. Sjöholm, *Evaluation of wind flow with a nacelle-mounted, continuous wave wind lidar*, in EWEA 2014 conference, 2014.

[13] T. Mikkelsen, N. Angelou, K. Hansen, M. Sjöholm, M. Harris, C. Slinger, P. Hadley, R. Scullion, G. Ellis, and G. Vives, *A spinner-integrated wind lidar for enhanced wind turbine control*, Wind Energy, 16 (2013), pp. 625–643.

[14] E. Muljadi and C. P. Butterfield, *Pitch-controlled variable-speed wind turbine generation*, IEEE Transactions on Industry Applications, 37 (2001), pp. 240–246.

[15] D. Schlipf, J. Anger, S. Kapp, O. Bischoff, M. Hofsäss, A. Rettenmeier, and M. Kühn, *Prospects of optimization of energy production by lidar assisted control of wind turbines.*, in Proceedings of European Wind Energy Conference and Exhibition, EWEA, 2011.

[16] A. Scholbrock, P. Fleming, A. Wright, C. Slinger, J. Medley, and M. Harris, *Field test results from lidar measured yaw control for improved yaw alignment with the nrel controls advanced research turbine: Preprint*, tech. rep., National Renewable Energy Laboratory (NREL), Golden, CO., 2014.

[17] C. VerHulst and C. Meneveau, *Large eddy simulation study of the kinetic energy entrainment by energetic turbulent flow structures in large wind farms*, Physics of Fluids, 26 (2014), p. 025113.

[18] ——, *Altering kinetic energy entrainment in large Eddy simulations of large wind farms using unconventional wind turbine actuator forcing*, Energies, 8 (2015), pp. 370–386.

[19] R. Wagner, M. Courtney, T. Pedersen, and R. Campus, *Power performance measured using a nacellemounted lidar*, Dewi Magazine (2013), pp. 49–54.

[20] R. Wiser, Z. Yang, M. Hand, O. Hohmeyer, D. Infield, P. H. Jensen, V. Nikolaev, M. O'Malley, G. Sinden, and A. Zervos, *Wind energy*, IPCC Special Report on Renewable Energy Sources and Climate Change Mitigation (2011).

[21] D. Yang, C. Meneveau, and L. Shen, *Large-eddy simulation of offshore wind farm*, Physics of Fluids, 26 (2014), p. 025101.

CHAPTER 2

INVESTIGATION OF THE INCOMING WIND VECTOR FOR IMPROVED WIND TURBINE YAW-ADJUSTMENT UNDER DIFFERENT ATMOSPHERIC AND WIND FARM CONDITIONS

Renewable Energy (2017) 101, 376-386. Investigation of the incoming wind vector for improved wind turbine yaw-adjustment under different atmospheric and wind farm conditions. G. Cortina, V. Sharma, M. Calaf.

Renewable Energy 101 (2017) 376–386

Contents lists available at ScienceDirect

Renewable Energy

journal homepage: www.elsevier.com/locate/renene

Investigation of the incoming wind vector for improved wind turbine yaw-adjustment under different atmospheric and wind farm conditions

G. Cortina [a, *], V. Sharma [b], M. Calaf [a]

[a] Department of Mechanical Engineering, University of Utah, Utah, USA
[b] School of Architecture, Civil and Environmental Engineering, EPFL, Lausanne, Switzerland

ARTICLE INFO

Article history:
Received 23 November 2015
Received in revised form
31 May 2016
Accepted 5 August 2016

Keywords:
Large eddy simulation
LIDAR
Wind energy
Wind farm
Wind turbines
Yaw-misalignment

ABSTRACT

Regardless of the evolution of wind energy harvesting, the way in which turbines obtain in-situ meteorological information remains the same - i.e. using traditional wind vanes and cup anemometers installed at the turbine's nacelle, right behind the blades. As a result, misalignment with the mean wind vector is common and energy losses up to 4.6% can be experienced as well as increases in loading and structural fatigue. A solution for the near-blade monitoring is to install wind LIDAR devices on the turbines' nacelle. This technique is currently under development as an alternative to traditional in-situ wind anemometry because it can measure the wind vector at substantial distances upwind. But at what upwind distance should they interrogate the atmosphere? and, what is the optimal average time in which to learn about the incoming flow conditions? This work simulates wind fields approaching isolated wind turbines and wind turbine arrays within large wind farms using Large Eddy Simulations. The goal is to investigate the existence of an optimal upstream scanning distance and average time for wind turbines to measure the incoming wind conditions under different ambient atmospheric conditions. Results reveal no significant differences when measuring the incoming wind vector at different upstream distances, regardless of the atmospheric stratification. Within this framework a 30 min readjustment period is observed to perform the best.

1. Introduction

Over the past ten years wind energy harvesting has experienced a rapid growth, with an overall installed global power average annual increase of the total installed wind power capacity of 25% per year in the last ten years (2002–2012) [1]. Throughout this time wind turbine designs have evolved, with increases in rotor diameter and overall efficiency designs. By 2004–08 most wind turbines had a ~70–80 meter rotor diameter, and currently, rotor diameter designs are approaching 100 m with an average hub height of 80 m [2]. Engineering improvements have accompanied the development of large rotors. However, the way in which wind turbines obtain in-situ meteorological information remains the same – traditional wind vanes and cup anemometers are installed at the turbines nacelle, right behind the blades. The orientation and other operating parameters of the turbine are governed by these two wind measurements through the use of a control loop [3].

These wind measurements have important drawbacks, especially with increasing rotor diameters. Since the velocity is measured at a single point immediately behind the blades, turbine misalignment with the mean wind direction is common [4]. In principle, this problem should be overcome using the so-called nacelle transfer functions (NTFs), which describe the relation between the nacelle wind vector measurements and the unperturbed wind vector upstream of the wind farm. The NTFs are used to properly correct nacelle measurements [5]; however, they have a strong variability from site to site and they don't account for changes in atmospheric-stratification. For example, Vanderwende and Lundquist [6] experimentally showed distinct wind turbine performances, with respect to a given wind turbine power coefficient curve, under different atmospheric regimes. They demonstrated under-performance during stably-stratified periods and over-performance during unstably-stratified periods and

* Corresponding author.
E-mail address: gerard.cortina@utah.edu (G. Cortina).
URL: http://wet.mech.utah.edu/

http://dx.doi.org/10.1016/j.renene.2016.08.011
0960-1481/

moderate wind speeds (8–12 ms^{-1}). An additional drawback from the near-blade monitoring is the limited time it provides the wind turbine controllers to adjust the turbine operating parameters' to account for changes in the approaching wind flow [7]. This latency in adjusting to ambient wind direction and speed subjects the blades and turbine structure to unanticipated wind gusts or extreme incoming wind conditions. These velocity aberrations induce increased loading, structural fatigue, power-train failures and associated increases in maintenance costs. A solution is to install forward directed wind Laser Imaging Detection and Ranging (LIDAR) on the turbines' nacelles. Future studies might find a way to measure ahead of time these velocity aberrations and wind gusts with the use of wind LIDARs, which together with advanced control systems will advice the wind turbine controls system to correct their settings. Also experimental LES studies should be performed in order to study the turbulent flow upstream of the wind turbines. Although LIDAR technology has been around since the early 1970s [8–10], it hasn't been until the recent advancements in optical fiber technology that such LIDARs have become affordable. Because wind LIDARs measure the frequency shift of the backscattered light initially sent by a laser beam, making it possible to measure the along-beam component of the wind velocity at various distances upwind of the rotor. By using a cone-scanning or volumetric scanning technique, the full three-dimensional wind components can be used to measure the approaching unperturbed winds [7, 11–17].

Further, recent studies have shown the potential of optimizing the overall power output of a wind farm by forcing a fixed yaw-misalignement on the upwind wind turbine arrays such that their corresponding wakes are laterally deviated and reducing their corresponding interaction with the downstream turbines [17–19]. Gebraad et al. [18] developed a control-oriented dynamic model that determines the best orientation of a given wind turbine to avoid turbine-wake interaction. Also the National Renewable Energy Laboratory (NREL) experimentally implemented at the Fishermens Atlantic City Windfarm a control strategy to reduce the wind-turbine wake interaction, obtaining up to a 10% increase in harvested power for the overall wind farm [19]. Yet, for these wind farm optimization techniques to be efficient, it is critical to accurately know the correct yaw-alignment of the turbine with respect to the incoming wind vector. The use of a wind LIDAR mounted on the turbine's nacelle has been shown to provide good yaw alignment and better power curves than traditional wind vanes, therefore enhancing the overall power output [20–22]. However, wind LIDAR systems are optimized to measure over a fixed upwind range and average over a certain period of time. The question remains as to what upwind distance they should interrogate the atmosphere and for what time period. In the present work, different upstream scanning distances and averaging times are evaluated within different atmospheric stratifications using Large Eddy Simulations (LES) driven with the experimental data of the well known Cooperative Atmospheric Surface Exchange Study (CASES-99) [23–25]. In Section 2, the LES code is presented in detail together with the sub-grid model, the boundary conditions and the wind turbine model used. Section 3 introduces the study cases considered, and Section 4 introduces the numerical results, first with respect to different upstream scanning distances and second with respect to distinct yawing averaging times. Finally, the conclusions are presented in Section 5.

2. Large-eddy simulation framework

The present work uses the Large Eddy Simulation code introduced in Sharma et al. [26]. The numerical code integrates the non-dimensional, incompressible, and filtered Navier-Stokes (NS) equations together with the continuity equation. The NS equation is implemented using its rotational form to assure conservation of energy and mass of the inertial terms [27]. The effect of temperature is introduced by means of a buoyancy term in the NS equation, which is the result of the Boussinesq approximation, and which is obtained from solving a coupled advection-diffusion equation for the potential temperature (θ). Therefore, the full set of equations solved is,

$$\frac{\partial \tilde{u}_i}{\partial x_i} = 0, \tag{1}$$

$$\frac{\partial \tilde{u}_i}{\partial t} + \tilde{u}_j \left(\frac{\partial \tilde{u}_i}{\partial x_j} - \frac{\partial \tilde{u}_j}{\partial x_i} \right) = -\frac{1}{\rho}\frac{\partial p^*}{\partial x_i} - \frac{\partial \tilde{\tau}_{ij}}{\partial x_j} + g \left(\frac{\tilde{\theta} - \langle \tilde{\theta} \rangle}{\theta_0} \right) \delta_{i3} + \\ + f(\tilde{u}_2 - v_G)\delta_{i1} - f(\tilde{u}_1 - u_G)\delta_{i2} + f_i, \tag{2}$$

$$\frac{\partial \tilde{\theta}}{\partial t} + \tilde{u}_j \frac{\partial \tilde{\theta}}{\partial x_j} = -\frac{\partial \pi_j}{\partial x_j}. \tag{3}$$

Here, the tilde (˜) represents the LES filtering operation at the grid-size Δ, and the angle brackets (⟨•⟩) represent a horizontal average, with index notation used to specify rectangular Cartesian coordinates $i = 1,2,3 = x,y,z$. The reference temperature is denoted by θ_0. The $\tilde{\tau}_{ij}$ term represents the deviatoric part of the momentum sub-grid stress (SGS) term, which is modeled using the Lagrangian Scale Dependent model of Bou-Zeid et al. [28], and π_j represents the sub-grid component of the thermal equation, which is correspondingly modeled with the adaptation of the Lagrangian Scale Dependent model for scalars introduced in Calaf et al. [29]. The modified kinematic pressure term (p^*) includes the filtered pressure term and the trace of the SGS tensor $\left(\tilde{p}/\rho + \tilde{\tau}_{kk}/3 + \frac{1}{2}\tilde{u}_j\tilde{u}_j\right)$. Within this work, the flow is forced with a time- and height-independent geostrophic wind (u_G,v_G), where f represents the Coriolis parameter, and δ_{ij} is the Kronecker delta ($\delta_{ij} = 1$, if $i = j$, and 0 otherwise). The f_i term represents the sink of momentum induced by the wind turbine. It is represented as a body force (per unit volume) and it is modeled using the traditional actuator-disk with rotation (ADR, see Wu et al. [30]) including the dynamical yaw-alignement of Sharma et al. [26]. Note that within the formulation of these equations the potential temperature is an active scalar that modifies the momentum equation by means of the buoyancy term, which accounts for the vertical motions induced by the thermal stratification. Further, as it is traditional in LES of atmospheric flows, the viscous effects are neglected and the flow is therefore characterized by a very large Reynolds number. The numerical discretization of the equations follows the one introduced by Moeng [31] and Alberston et al. [32], where a pseudo-spectral approach with a staggered-grid is used. Therefore, second-order finite differences are used in the vertical direction and a spectral discretization using the Fast Fourier Transform in the West (FFTW) [33] library is implemented in the horizontal directions. As a result of the Fourier discretization in the horizontal directions the numerical domain becomes periodic, eliminating the need for lateral boundary conditions and becoming infinite in practical effects.

The equations are dealiazed using the 3/2-rule [34], and time-integrated using a second order Adam-Bashfort scheme. The numerical algorithm is fully parallelized using the Message-Passing Interface (MPI) with a total of 64 processors and the pressure solver is further parallelized with the pipeline Thomas algorithm [35]. As a result of the periodic boundary conditions in the horizontal directions, there is no need for lateral boundary conditions. For the top boundary a zero-flux and zero-shear are imposed, with

the vertical velocity and the gradients of the horizontal velocities equal to zero. At the surface, the non-slip condition is imposed for the vertical velocity, and because of the staggered grid, an equivalent shear stress is imposed at the first grid point for the horizontal velocities. The shear stress at the surface is parametrized using the traditional log-law including the effects of surface stratification [28,36,37],

$$\tau_{i,3}(x,y,z_1) = -\left[\frac{k\sqrt{\left(\widehat{u}_1^2+\widehat{u}_2^2\right)}}{ln\,(z_1/z_0)+\psi_m(z_1/L)}\right]^2 n_i. \tag{4}$$

In this equation z_1 indicates the height of the first grid point where the horizontal velocity components are computed ($\Delta_z/2$) and where the shear stress is applied, i indicates any of the horizontal plane-parallel directions ($i = 1,2$), and n_i is a unitary directional vector, $n_i = \widehat{\tilde{u}}_i/\sqrt{\widehat{\tilde{u}}_1^2+\widehat{\tilde{u}}_2^2}$. While this expression was originally developed for ensemble averages and later interpreted as spatial averages over homogeneous surfaces, here a double filtering at 2Δ grid spacing, equivalent to a local averaging, is used instead (see Refs. [28,37] for further details in this filtering). In this study the surface roughness is maintained homogeneous over the entire domain with a value of $z_0 = 3{\cdot}10^{-5}z_i$ (where z_i is the initial inversion height, which will be used as a normalization length-scale, see later). To numerically integrate the NS equations, the vertical derivatives of the horizontal velocities are also parametrized at the first grid point (z_1) using Monin-Obukhov similarity theory [38],

$$\partial_3\tilde{u}_i(x,y,z_1) = \left(\frac{\sqrt{\tau}}{\kappa z}\right)n_i, \tag{5}$$

with $\tau = \sqrt{\tau_{1,3}^2+\tau_{2,3}^2}$. In addition, to integrate the advection-diffusion equation for the potential temperature a sensible heat flux is imposed at the first grid point, similar to the momentum, also using Monin-Obukhov similarity theory,

$$H_s(x,y,z_1) = \frac{\kappa^2\left[\theta_s-\tilde{\theta}(x,y,z_1)\right]\left(\sqrt{\widehat{u}_1^2+\widehat{u}_2^2}\right)}{\left[ln\left(\frac{z_1}{z_0}\right)+\psi_m(z/L)\right]\left[ln\,\frac{z_1}{z_{0,h}}\right)+\psi_h(z/L)\right]}. \tag{6}$$

The surface temperature (θ_s) is imposed as bottom boundary condition (see Fig. 1a) and $z_{0,h}$ represents the scalar surface roughness, which has been taken to be one tenth of the momentum surface roughness ($z_{0,h} = z_0/10$) [39]. The stability correction functions ($\psi(z/L)$) implemented are those from Brutsaert [40]. Different formulations exist depending on stability and the appropriate choice of functions is made based upon the Obukhov length (L) depicted in Fig. 1b and defined as

$$L = \frac{-u_\star^3\,\overline{\theta}_s}{\kappa\, g\left(\overline{w'\theta'}\right)_s}, \tag{7}$$

where $u_\star$ is the friction velocity, $\overline{\theta}_s$ is the mean potential temperature, κ is the von Kárman constant ($\kappa = 0.4$), g represents the gravity term and $\overline{w'\theta'}$ is the surface sensible heat flux. In this work it is well understood that the stability correction functions were initially developed from experimental studies on statistically homogeneous surfaces and that the wind turbines might have an effect on the precise parametrization of the stability correction functions. However, lack of new experimental data on this precise matter doesn't allow for a better numerical approach at the present time.

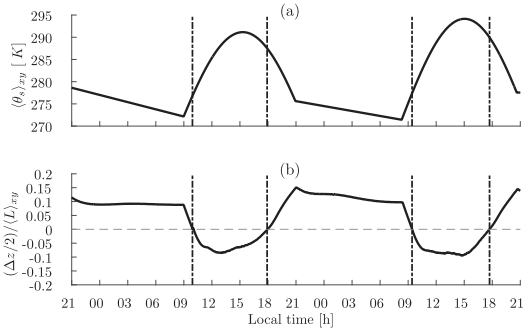

Fig. 1. (a) Spatially averaged and time-dependent imposed potential temperature at the surface of the domain $\langle\theta_s\rangle_{xy}$ [K]; (b) normalized stability parameter, $(\Delta z/2)/\langle L\rangle_{xy}$, where $(\Delta z/2)$ is the hight of the first grid-point and L is the Monin-Obukhov length as a function of time.

3. Study case description

To develop this study two different sets of simulations, both of which included the presence of wind turbines, were considered. One case consisted of a traditional very large wind farm (VLWF), and the second one consisted of a largely spaced wind farm (LSWF), or equivalently seen as a single wind turbine. For all cases, the turbines were immersed within an atmospheric boundary layer that would evolve with time, such that the wind farms could experience different flow types with different atmospheric stratification. Precisely, each simulation was run for a total of 48 h (real-time), in which the initial conditions and forcing of the flow was extracted from the CASES-99 field experiment. This means that the atmospheric flow evolved over two complete days. In order to ensure the simulation of a realistic diurnal cycle the numerical simulations were forced with a height-independent and time-constant geostrophic wind together with a time-varying surface temperature. The values for the geostrophic wind and surface temperature were extracted from the CASES-99 field experiment between October 22–24, 1999. This period was previously studied by Kumar et al. [24] to illustrate the wellness of the LES simulations. Recently, Fitch et al. [41] and Sharma et al. [42] used the same period of time to investigate the effects of finite-size and very-large wind farms on a realistic diurnal cycle using mesoscale simulations (WRF) and LES, respectively. It is for this reason that the same forcing is used in this work.

The detailed time-evolution of the surface temperature is represented in Fig. 1a, and the corresponding evolution of the atmospheric stratification is represented in Fig. 1b, where the non-dimensional stability parameter $z/\langle L\rangle_{xy}$ is presented (with $z = \Delta z/2$). The vertical dashed lines indicate the times with an atmospheric stratification change (0955, 1752, 0925 and 1842) and they will be used in other Figures throughout this work. In addition, the flow was forced with a geostrophic wind of value (u_G,v_G), and the domain size was set to $(2\pi \times \pi \times 3)z_i$, where z_i is the height of the boundary layer, initially located at 1000 m height. To keep a fairly high numerical resolution, a computational domain with $256 \times 128 \times 384$ grid points was used. The simulations where initialized with a height-independent geostrophic wind and a well mixed temperature profile matching the initial surface temperature of 278.6K, with an inversion layer spanning from z_i to the top of the domain, with $z_i = 1000m$. The LES was initialized with vertical profiles of velocity and temperature extracted from Kumar et al.

[25]. Overall, a total of 19 different cases (7 for VLWF and 12 for the LSWF) have been considered to evaluate the effect of the upstream scanning distances and orientation times.

3.1. Very large wind farm (VLWF)

The VLWF configuration consisted of 48 wind turbines homogeneously distributed in 8 rows and 6 columns using the traditional spacing of ~8D and ~5D (where D refers to the turbines' rotor diameter) in the streamwise and spanwise directions, respectively (see Fig. 2a for details). Similar to previous studies [43] the turbines' hub-height (z_h) was located at 100 m and the wind turbine diameter was equally set to 100 m. Besides parametrizing the wind turbines using the actuator disk (AD) with rotation approach of Wu et al. [30] including the dynamical yaw-alignement of Sharma et al. [26], the turbines were additionally capable of dynamically yaw-align with the incoming wind vector measured at different upstream scanning distances, similar to what a real wind turbine would do if equipped with a wind LIDAR. Therefore, each row of wind turbines was configured such to measure the incoming wind vector at a different upstream distance ranging between 50 m (D/2) and 200 m (2D) upstream (D/2, 3D/4, D, 5D/4, 3D/2 and 2D). In the most basic mode, the wind turbine model readjusts the yaw orientation every 10 min according to the averaged wind vector measured at the predetermined upstream scanning distance. The incoming wind vector is equally averaged for 10 min, and the angle of the incoming wind is measured as $\tan^{-1}(\langle vd\rangle/\langle ud\rangle)$, where the overline represents the time average and $\langle \bullet \rangle$ represents the spatial average of u_d and v_d, which denote the horizontal velocities at the upstream disk area scanned by a hypothetical wind LIDAR. This configuration allowed us to study the effect of using different upstream scanning distances to measure the incoming wind vector and correspondingly readjust the turbine's yaw-alignment.

In addition, in this work we are interested in deciphering the effect of the averaging and readjustment time to determine the correct incoming wind vector, given a fixed upstream scanning distance (e.g. D/2). For this reason, a suite of seven simulations was used, where each used a different averaging time to measure the upstream incoming wind vector (1 s, 5 min, 10 min, 20 min, 30 min, 45 min, 60 min). Because of the unaffordable numerical cost it would imply running 7 additional diurnal cycles, each one considering a different averaging time, shorter simulations (4 h of physical time) were performed for the day, unstable period (1330–1730), and for the night, stable period (0130–0530), so that the effect of stratification (unstable and stable) could be analyzed.

3.2. Largely spaced wind farm (LSWF)

The LSWF consists of a wind farm where the constituent wind turbines are highly spaced. This case could perfectly correspond to the case of a single wind turbine. Notice that given the size of the numerical domain, although it is periodic as mentioned in Section 2, the wake of the wind turbine doesn't interact with itself, meaning that in practice we are effectively modeling a single wind turbine. For this case, the characteristics of the wind turbine are exactly the same as the ones described in the VLWF case. Equivalently, the turbines forming this very large spaced wind farm would be in practice separated by ~63D and ~31D in the streamwise and spanwise directions, respectively (see Fig. 2b for details). In this case, and as a result of the computational cost of the simulations, only 4 upstream scanning configurations were considered (D/2, D, 3D/4, and 2D). Note that for each upstream scanning configuration 48 h of real time flow were simulated. Similar to what was done in the VLWF configuration, the same shorter events, representing unstable and stable stratified conditions, were used to study the effect of the different averaging times (1 s, 5 min, 10 min, 20 min, 30 min, 45 min, 60 min).

4. Results

The nominal loss in harvested power induced by a given yaw-misalignment angle is provided by the cosine cubed of the misalignment angle ($\cos^3\phi_e$). It is for this reason that the turbine's harvested power is highly sensitive to the turbine's capacity to timely align with the incoming wind vector. In Fig. 3b, a graphical representation of the yaw-misalignement of a wind turbine with the incoming wind vector is presented. Fig. 3a indicates the corresponding loss in power induced by different degrees of misalignment. It can be observed that yaw errors of 10° can reduce the harvested power by about 5%, and errors of 15° can reduce as much as 10% of the harvested power. While these values might seem small a priori, their corresponding economical translation is certainly important. In Table 1 it is shown an estimation of the economical loss in revenue due the wind turbine misalignment. The analysis is performed for two different offshore large wind farm scenarios: the well known Danish Horns Rev 2 wind farm and the projected Horns Rev 3, located at the North Sea. Results show that for a misalignment of 5° the total economical loss is 0.3M€/year and 3.1M€/year for the Horns Rev 2 wind farm and Horns Rev 3, respectively. Additionally, for a misalignment of 10° it corresponds to a loss of 1.1M€/year and 10.5M€/year. The data to compute the economics has been extracted from the Danish energy agency [44] assuming a capacity factor of 65% for the Horns Rev 3 and an average bid price of 25€/MWh for the Horns Rev 2, representative of the 2014–15 energy market [45,46]. The estimated annual energy production of a wind farm is obtained by multiplying the nominal power of the wind farm by a total year time and the corresponding wind farm capacity factor. By multiplying the energy

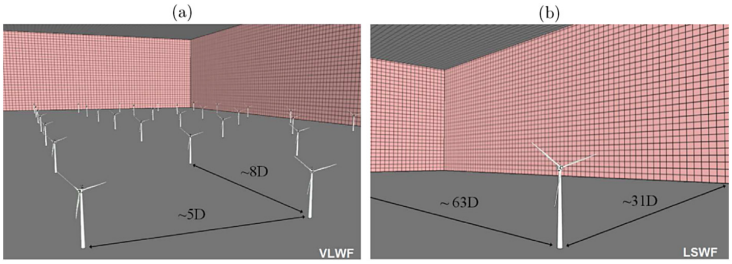

Fig. 2. a) Very large wind farm case (VLWF); (b) Largely spaced wind farm case (LSWF).

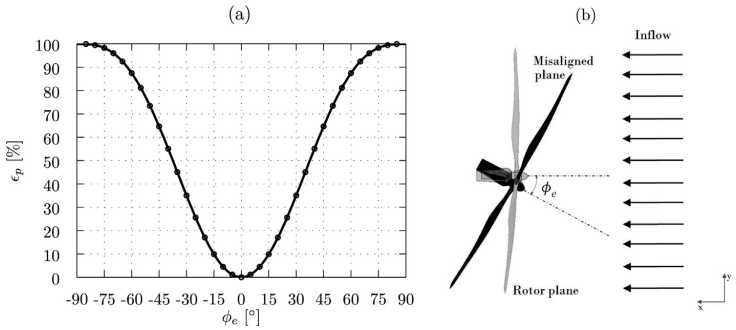

Fig. 3. (a) Theoretical representation of the error in power [$\epsilon_p = (1 - \cos^3(\phi_e)) \times 100$] due to the wind turbine misalignment; (b) schematic representation of the wind turbine misalignment.

Table 1
Parameters used to estimate the economical loss for two given average yearly misalignments and for two distinct scenarios, Horns Rev 2 in current operational conditions and for the projected Horns Rev 3 wind farm.

	Horns rev 2	Horns rev 3 (projected)
Number of wind turbines	91	50
Wind farm nominal power	209 MW	400 MW
Capacity factor (CF)	50%	65%
Estimated annual energy production	915GWh	2,278GWh
Bid price	25€/MWh	103€/MWh
Yearly income	13M€	235M€
Revenue loss for a misalignment of 5°	0.3M€/year	3.1M€/year
Revenue loss for a misalignment of 10°	1.1M€/year	10.5M€/year

bid price by the estimated annual production, one obtains the yearly income. To obtain the revenue loss, the yearly income should be multiplied by the error in harvested power due to the yaw-misalignment of the turbine depicted in Fig. 3b. Overall, the loss in income showed in Table 1 partially illustrates the urgent need for reducing the misalignment error.

4.1. Optimal upstream distance at which wind LIDARs should interrogate the atmosphere

One of the objectives of this work is to assess whether there exists an optimal upstream scanning distance for wind LIDARs to retrieve the most-accurate yaw-alignment angle considering the effect of changing atmospheric stratification. At the same time, we aim to better analyze the potential yaw-misalignment induced by measuring with a wind vane placed behind the rotor blades.

Subplots a_i and b_i in Fig. 4 present vertical profiles of wind velocity together with their corresponding incidence angle for a 10-min period representative of the unstable stratification (i.e. averaged between 0230 and 0240pm; $i = 1$ to 3) and for both cases, the LSWF ($4a_i$) and the VLWF ($4b_i$). Subplots $4c_i$ and $4d_i$ illustrate the same profiles for a 10-min period representative of the stable stratification (i.e. averaged between 0030 and 0040am) also for both cases the LSWF ($4c_i$) and the VLWF ($4d_i$). The vertical profiles have been planar-averaged (denoted by the sub-index y) along the upstream plane parallel to the turbine's rotor disk, and the vertical axis is normalized with the turbines' hub-height ($z_h = 100m$). Subplots $4a_1$-d_1 represent the magnitude of the incoming wind ($\overline{U} = \sqrt{\overline{u}^2 + \overline{v}^2 + \overline{w}^2}$) at different upstream distances ($D/2$, $3D/4, D$, $5D/4$, $3D/2$, $2D$) and at the traditional nacelle's wind vane location ($-3D/10$) normalized by the geostrophic wind ($\overline{U}_G = \sqrt{\overline{u}_G^2 + \overline{v}_G^2}$). For all the subplots, the turbine's rotor-disk region is constrained between two horizontal dot-dashed lines, and the precise location of the hub is indicated with a horizontal dash line. Because the differences in wind magnitude are small between all the upstream scanning distances the relative differences with respect to the measured wind magnitude at $D/2$ ($\langle\overline{U}_i\rangle_y - \langle\overline{U}_{D/2}\rangle_y$) are also presented in subplots $4a_2$-d_2. The $D/2$ distance has been selected as a reference upstream measure because it is close to the wind turbine and still outside of the induction zone [47]. Finally, subplots $4a_3$-d_3 represent the normalized relative difference with the yaw-angle measured at $D/2$, $(\langle\overline{\phi}_i\rangle_y - \langle\overline{\phi}_{D/2}\rangle_y)/\langle\overline{\phi}_{D/2}\rangle_y$.

In the measure of the incoming wind, we observe a maximum difference of 7.4% between the furthest upstream scanning distance ($2D$) and the wind vector at $D/2$ for the LSWF and a difference of 4.6% for the VLWF, both during the unstable stratification period (subplots $4a_2$ and $4b_2$). For the closer upstream scanning distances these differences decrease. As one would expect, the measurements from the wind vane proxy present larger differences with a maximum difference of 20.2% and 16% for the LSWF and the VLWF cases, respectively. During the stably stratified period (subplots $4c_2$ and $4d_2$) maximum differences of 6.7% and 4.7% between the furthest upstream scanning distance ($2D$) and the wind vector at $D/2$ are observed for the LSWF the VLWF case, respectively. Also, the measurements for the wind vane proxy present larger differences with a maximum of 17.3% for the LSWF and 13% for VLWF case. The average standard deviations of the relative velocities at hub height are 0.43% and 1.5% correspondingly for the VLWF under unstable and stable conditions, and 4% and 2% for the LSWF for the unstable and stable cases.

In the measure of the yaw-angle, the most important is to note the quasi-inexistent difference obtained when measuring at different upstream distances, regardless of the stratification. Once more, it is interesting to notice the large differences with the measurement position behind the blades. Once the flow crosses the rotor disk area, there exists a large deflection angle of up to 22.4% for the LSWF and close to 9% for the VLWF for the different stratifications. Similarly, the measured yaw-angle for the stable period (see subplots $4c_3$ and $4d_3$) remains practically the same for all the upstream scanning distances, and the nacelle angle is deflected by smaller values in comparison to the unstable regime. Note that the characteristic difference in magnitude between the results obtained for the VLWF and the LSWF is a result of the higher turbulence intensity in the VLWF that tends to homogenize the turbulent flow around the wind turbines [48–50]. Also, the proxy for the incoming wind vector measured by the wind vane corresponds to an approximate measure a wind vane would provide when

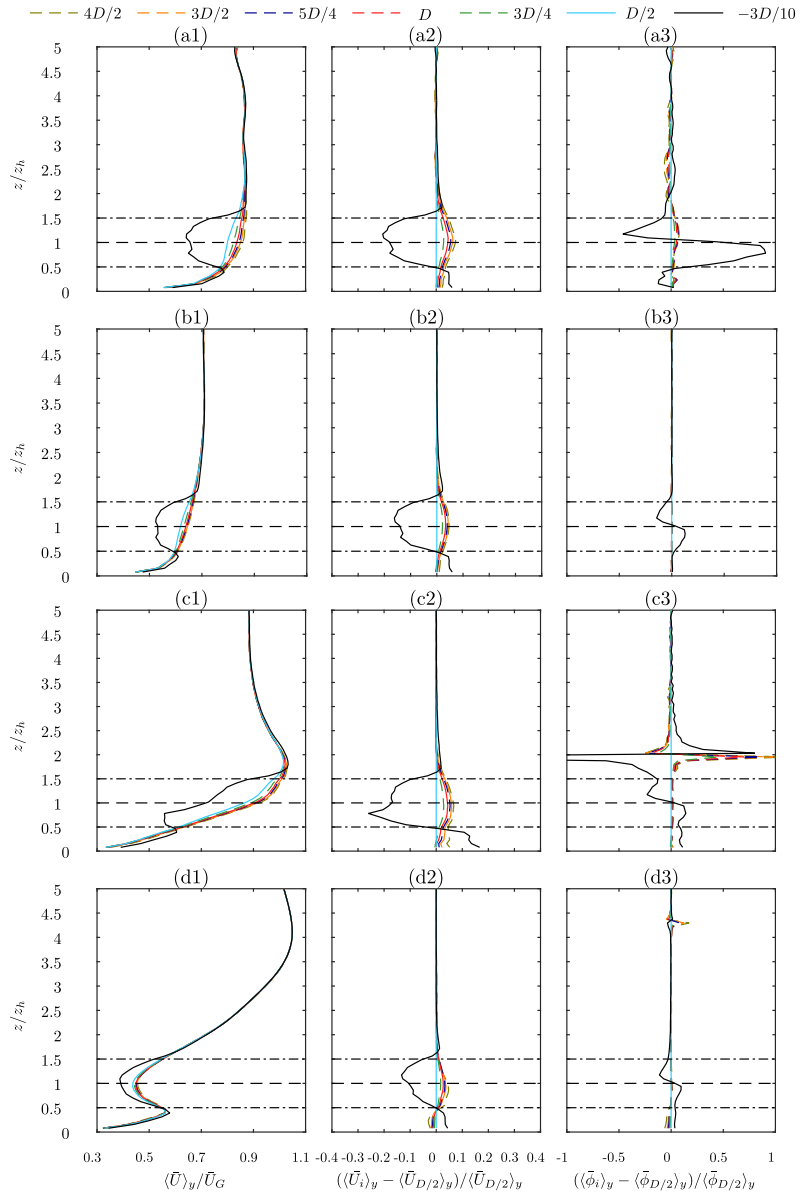

Fig. 4. Vertical averaged profiles of normalized velocity magnitude (a_1 and c_1), relative velocity magnitude (a_2 and c_2) and relative angle (a_3 and c_3) for the LSWF for the stable (a_i) and unstable (c_i) stratified periods. A similar structure is used in subplots b_i and d_i for the VLWF case, respectively.

installed at the turbine's nacelle, right behind the rotor-blades and without being corrected with the often used NTFs.

By comparing subplots ($4a_i$ and b_i) to subplots ($4c_i$ and d_i) the effect of atmospheric stratification on the incoming wind vector (module and angle) is clearly observed. At night, during the stable period, a characteristic nocturnal low-level jet (LLJ) forms at heights between $1 \leq z/z_h \leq 2$, which interacts with the top section of the wind turbine blades. In the case of a VLWF the LLJ is shifted by the presence of the very large wind farm [51]. While the LLJ induces relevant changes on the wind vector profiles, the relative differences between the different upstream scanning regions remain similar between the day-time and night-time.

Overall, the results presented within Fig. 4 show that there are no significant differences in the incoming wind vector when

measured at different upstream distances and for different atmospheric stability conditions. Even thought Fig. 4 shows the behavior of 10 min data during the unstable-stratified and stable-stratified periods, a similar behavior is observed for different 10 min averaged periods along the two diurnal cycles (not shown here for the sake of clarity). This result is really important because it will allow the nacelle installed wind LIDARs to learn from the incoming wind vector at further upstream distances, providing more time to the wind turbines to readjust their corresponding settings and hence optimally adapting to the incoming flow. Results are the opposite for the nacelle wind vane location. In this case, results show how the measured flow diverges from the one reaching the blades, with errors of up to 22.41% in the measure of the wind vector angle. These results are in-line with experimental measurements done using a real wind LIDAR mounted on the nacelle of a wind turbine [7]. Currently, wind turbine operators get around these large errors by imposing an 'ad-hoc' correction function using an unperturbed wind vector measurement from a meteorological-tower, upstream of the farm. Yet, these correction functions rarely account for the effect of atmospheric stability, which is shown to have a relevant effect in the deflection of the yaw-angle measured at the nacelle for the LSWF case (30% and 20% for the unstable and stable in average, respectively), and a more attenuated effect for the VLWF case (10% and 5% for the unstable and stable in average, respectively), right behind the blades. The reduced wind-angle deflection on the VLWF is a result of the enhanced mixing produced by the large array of wind turbines.

To further explore the effect of atmospheric stratification on the incoming wind vector, Fig. 5 illustrates the average yaw angle ($\langle\phi\rangle$ WT) as a function of the local time for a duration of two complete diurnal cycles, where ($\langle\bullet\rangle_{WT}$) represents the average among the distinct wind turbines. The yaw angle has been spatially averaged on the projection of the rotor disk at the different upstream distances, and therefore it is referred as an upstream rotor-disk average. Within this Figure, subplot 5a represents the average evolution of the yaw angle in the case of a LSWF and the blue shade indicates the corresponding standard deviation for the four different upstream scanning distances presented in Section 3.2. Supblot 5b depicts the case of the VLWF, where the blue line represents again the wind vector orientation averaged over all the wind turbines conforming the wind farm, and the blue shading indicates the corresponding standard deviation. The reason for averaging over all the wind turbines, without distinguishing between the turbines scanning at different upstream distances, is the similitude presented in Fig. 4. Further, the black line represents the average wind vector angle obtained by those wind turbines that learn about the incoming wind measuring behind the blades, as a proxy to a wind vane and cup anemometer, and the black shade represents the corresponding standard deviation. It is interesting to note that during the unstable regimes, as a result of the enhanced vertical and lateral mixing [52–55] there exists a larger variability (standard deviation) in the wind vector angle measured among the different turbines in comparison to the stably stratified regime. However, this differentiated behavior is not apparent in the wind turbines driven by the wind vane proxy, probably as a result of the continuous mixing produced by the blades regardless of the atmospheric stratification. Interestingly, the maximum error observed between the upstream and wind vane proxy measurements are close to 5° during the stable regime (from 0600 to 0900 in the first diurnal cycle). Almost no differences are observed during the unstable regime (from 1230 to 0100 of the first diurnal cycle). In subplot 5a, the same representation is used, where the maximum error is close to 4° and the minimum is close to 1°. Mikkelsen et al. [7] showed experimental misalignments of 10° root mean square (RMS) value for a 10 min average of a 3 h 20 min observation period during the night of April 30th, 2009. This is about half the error observed in subplot 5a. This underprediction of the LES could be due to the approximate wind turbine model used in the LES to represent the actual turbines. It is also interesting to note the difference in averaged angle values between the VLWF and LSWF cases. This is a result of the enhanced resistance introduced by the large wind farm in comparison to the largely spaced wind farm, which produces a deeper geostrophic imbalance.

As a result of the diurnal evolution of the yaw-angle and its associated standard deviation, a new unknown arises with respect to the use of wind LIDAR technology. From the presented results, it is clear that the scanning averaging time and corresponding turbine's readjustment frequency should also be analyzed. For

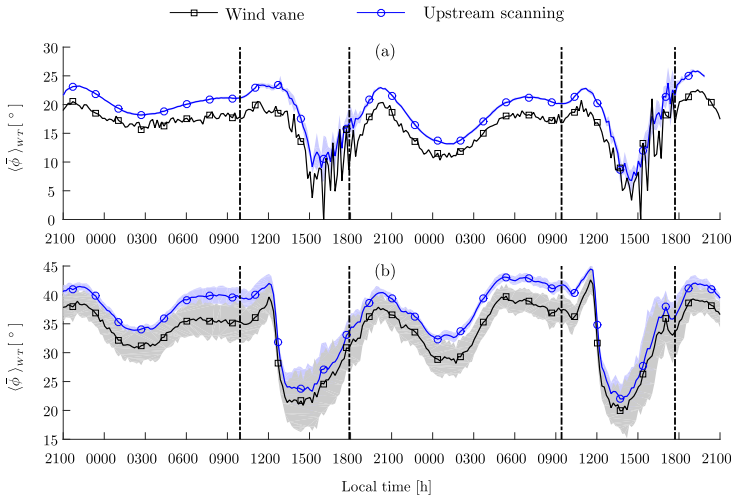

Fig. 5. Yaw alignment for the upstream scanning distance (in blue) and for the wind vane (in black), (a) for the LSWF and (b) for the VLWF. (For interpretation of the references to colour in this figure legend, the reader is referred to the web version of this article.)

example, one could wonder whether it could be more optimal to keep the wind turbine's yaw alignment fixed during day time, when the wind vector continuously changes direction and just allow the time-varying readjustment during night-time, when the flow changes less randomly. This additional degree of freedom is explored in the following section.

4.2. Optimal averaging time to interrogate the atmosphere

A total of 14 simulations of 4 h real-time length each have been performed to evaluate the effect of using different averaging times to readjust the turbine's yaw-alignment. The study includes both (stable and unstable) stability regimes for the two wind farm scenarios (VLWF and LSWF). In this case, the analysis is based on the same previous diurnal cycle, but only consider the time period between 0130 and 0530 to represent the stable regime, and the time period between 1330 and 1730 to represent the unstable stratification. During these periods of time the wind turbine model was configured as such to learn from the incoming wind vector at a fixed distance upstream of the rotor disk ($D/2$). The corresponding frequency of yaw-readjustment was varied, with time-periods ranging between 1 s and 60 min. Precisely, the studied readjustment time-periods are: 1 s, 5 min, 10 min, 20 min, 30 min, 45 min, and 60 min, where each set-up corresponds to a new numerical simulation in which all turbines are equally configured. These times also correspond to the averaging times used to determine the characteristics of the incoming wind vector (module and angle). In order to quantify the misalignment error with the incoming wind vector and hence the corresponding loss in power induced by the use of different averaging times, the simulation with 1-s readjustment-time has been used as a base case, or 'ground truth'.

In order to evaluate the performance of the different yawing times, Fig. 6 illustrates the normal probability density function (PDF) of the yawing error associated with the different study cases (VLWF versus LSWF, day-night for different averaging times). The error is computed as the difference between the angle of the incoming wind vector measured with a 1 Hz frequency and the angle obtained by the corresponding longer averages i.e. $\varepsilon_\phi = \overline{\phi}^{1s} - \overline{\phi}^{t}$, where t represents the different averaging times. Subplots 6a and 6b represent the study cases for the LSWF and subplots 6c and 6d for the VLWF, where 6a and 6c represent the stably stratified case and 6b and 6d illustrate the unstable case, respectively. Notice that the left and right dashed lines represent the 95% confidence intervals, which are equivalent to two standard deviations (2σ), for the 30 min PDF. It is worth noting that the unstable regimes are characterized by a wider PDF, which is related to the variability of the wind vector during the unstable regime. Subplot 6a shows that the probability density function of the associated error for the LSWF during the stably stratified period is overall quite small (less than 1° on the 60 min period case and for the mean value) when compared to the other scenarios, regardless of the averaging time. This means that even if one decides to use large periods of time between yaw-readjustments, the associated penalization in power loss would be very small. Also, it is interesting to notice that all the PDFs in subplot 6a are shifted towards the right. This phenomena is an effect of the preferential wind direction. For example, if the wind vector has a preferred clockwise rotation in time, the increase of the turbine's yawing time leads to larger errors. This is the result of the cumulative misalignment with longer times. This behavior is not seen in subplot 6c due to the high perturbation produced by the presence of a large wind farm. Also, in subplots 6b and 6d it is not observed as a result of the large mixing and not preferred direction of the flow during the unstable period.

In contrast, in the convective period for the LSWF case (subplot 6b), the means of the PDFs associated with the different readjustment periods are progressively shifted to larger biased errors with 95% confidence of ±12.86° contrasting with a ±0.86° for the stable period. Also, it is noticeable the larger standard deviation associated in this case, which is more than ten times larger than the one for the stable stratified period. In the VLWF cases (subplot 6c and 6d) results follow a similar trend with larger standard deviations on the unstable stratified period. However, in this case the error associated with larger readjustment periods is much more noticeable, with PDF mean values in exceedance of 5° during the stable stratified period, and larger than 10° during the unstable stratified period. Therefore, in VLWFs the continuous interaction between wakes truly penalizes the large yawing times with large errors observed, both during day-time and night-time (subplots 6c and 6d, respectively).

A better representation of the relationship between the yawing angle error presented in Fig. 6 and its direct effect on the harvested power is presented in Fig. 7. This figure illustrates the normalized cumulative error in power for the different atmospheric stability

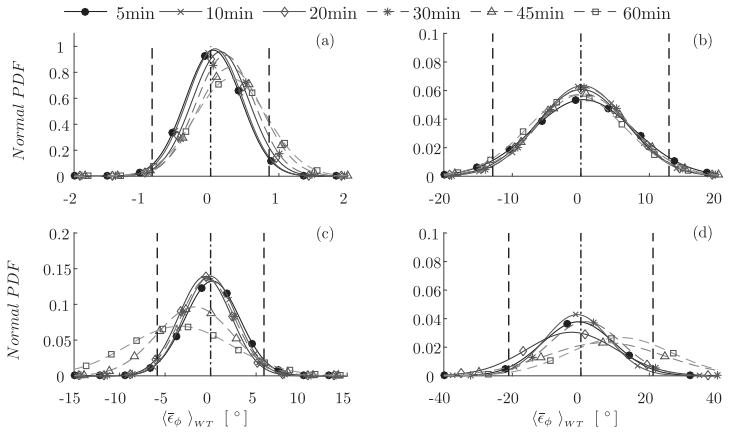

Fig. 6. Probability density function of the yaw-alignment error for the LSWF during the stable (a) and unstable (b) regimes, and for the VLWF, (c) and (d), respectively.

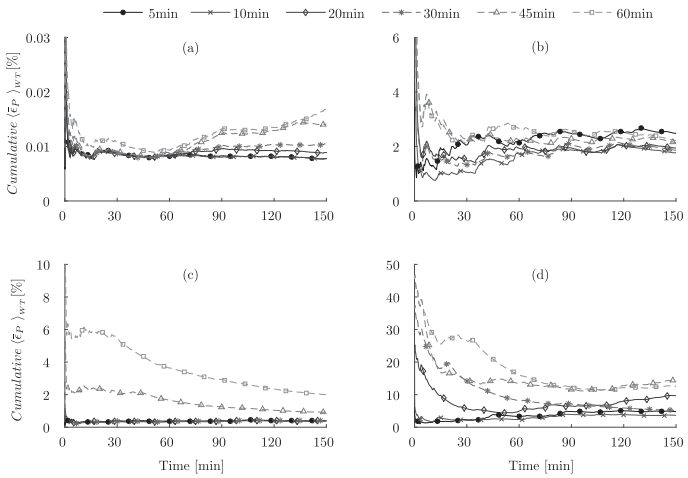

Fig. 7. Normalized cumulative error in power for the LSWF during the stable (a) and unstable (b) regimes, and for the VLWF, (c) and (d), respectively.

scenarios and for a period of time of 150 min. The associated error in harvested power (ε_P) is computed using the theoretical $\cos^3$ factor, provided the error in the yaw angle (ε_ϕ), meaning

$$\langle \overline{\varepsilon}_P \rangle_{WT}[\%] = \frac{100}{N} \sum_{t=1}^{N} \left(1 - \left|\cos^3(\langle \overline{\varepsilon}_\phi \rangle_{WT})\right|\right), \tag{8}$$

where N is the time cumulative number of events used to compute the error with a frequency of 1 Hz over 150 min (N = 9000) and the error in the yaw angle is computed as $\langle \overline{\varepsilon}_\phi \rangle_{WT} = \langle \overline{\phi}^{1s} - \overline{\phi}^{t} \rangle_{WT}$, where t represents the different averaging times. Notice that the initial cumulative error values ($\leq$ than the first 60 min) have a poor statistical meaning given the reduced amount of cumulative data points. The cumulative error becomes representative after the 90 min threshold (where N is equal to 5400). This explains the very large error encountered during the initial 5–10 min of the analysis, where N is still very small (300–600 data points respectively).

Interestingly, during the stable period for the LSWF (subplot *a*) the cumulative error in power is practically negligible (less than 0.02%), showing the excellent performance of the upstream scanning approach regardless of the yawing times. Nonetheless, it can be observed that the 5, 10 and 20 min readjustment times perform the best, as one could a priori expect. The small error associated to this case is due to the fact that the incoming wind is not perturbed by other wind turbines as well as due to the strong incoming winds associated with the LLJ. For the unstable stratified scenario of the LSWF (subplot 7b) there is a slight increase of the cumulative error in power as a result of the unstable ABL, but once again it presents small differences between the different readjustment times. Interestingly, the 10, 20 and 30 min readjustment periods present the lowest associated error in power. Indeed, it is the 5 min readjustment time that presents the largest cumulative error. Results show how the strong fluctuating winds characteristic of the daytime periods penalize the shorter readjustment time. It has been observed that once the yaw alignment has been corrected, it doesn't take long for the wind vector to change its orientation, inducing continuous large misalignment. In contrast, while larger times such as the 30 min readjustment period remains most of the time aligned, the absolute misalignment error remains smaller in magnitude.

Finally, subplots 7c and 7d represent the cumulative error in power for the VLWF. In both cases (stable and unstable regimes) results illustrate the effect of the continuous wake interaction, characteristic of large wind farms [52–55], with much larger errors for the longer readjustment times. A 2% and 12.5% cumulative error is observed for the 60 min readjustment-time for the stable and unstable cases respectively. Also in this case, the error appears to be larger for the convective time in comparison to the stable period.

Overall, the 30 min readjustment period seems to perform optimally within all the studied scenarios, presenting a small error for all the different cases independently of the stability and the particular wind farm scenario.

5. Conclusions

The goal of the present study was to investigate the possible existence of an optimal upstream scanning distance and readjustment-time to accurately learn about the incoming wind vector using wind LIDARs mounted on the wind turbine nacelle. To answer this question a total of nineteen LES cases have been developed which consider the canonical scenarios of a largely spaced wind farm (LSWF) and a very large wind farm (VLWF) under continuously changing atmospheric conditions.

The numerical results of two consecutive diurnal cycles reveal that during unstable regimes, as a result of the enhanced vertical and lateral mixing, there exists a larger variation in the incoming wind vector angle (~8°) compared to the stable period, which shows a 50% reduction in wind angle variability. For the LSWF under stable stratification the maximum error observed between the upstream and wind vane proxy measurements of wind direction are close to 5° (found between 0600 h and 0900 h) whereas almost no differences were observed during the late unstable period (between 1300 h and 1800h). For the VLWF case, the maximum error is close to 4° and the minimum is close to 1°. These results agree well with the experimental data of Mikkelsen et al. [7]. Nonetheless, some differences exist, which have been attributed to the approximate wind turbine model used in the LES to represent the wind turbines. However, results reveal no significant differences when measuring the incoming wind vector at different upstream distances, regardless of the atmospheric stratification.

This is a very important result because it will allow wind LIDARs to learn from the incoming wind vector at far upstream distances, hence providing longer readjustment times to reset the optimal turbine parameters.

Within this study the effect of the wind turbine yaw readjustment-time has also been considered. Results indicate that for the LSWF under stable conditions the overall cumulative error in power is very small (~0.015%), with time periods of 5, 10 and 20 min showing the best performance, and for the unstable conditions the 10, 20 and 30 min readjustment times showing the best performance (~2% error). In this case the 5 min period underperformed as a result of the fast and continuous change in the incoming wind vector (~3% error). In contrast, for the VLWF (cases, both stable and unstable) illustrate the effect of the continuous turbine-wake interactions, with much larger errors for longer readjustment times. For example, a 2% and 12.5% cumulative error in power are observed for the 60 min readjustment time for the stable and unstable atmospheric regimes correspondingly. Overall, the 30 min readjustment period seems to perform most optimally, presenting small errors for all the different study cases, independently of atmospheric stability and the particular wind farm configuration.

Acknowledgements

This research has been supported with the start-up funds provided by the Mechanical Engineering Department at University of Utah to Assistant Professor Marc Calaf. The authors would like to acknowledge the computational support provided by the Center for High Performance Computing (CHPC) at University of Utah. PhD student Varun Sharma thanks the support received through the Swiss National Science Foundation (project no. 200021134892/1 and 20020 125092), ETH Domain Centre for Competence in Environmental Sustainability, and the NSERC Discovery Grant (MBP) Scientific IT and Application Support (SCITAS) group at EPFL. Finally, we wish to acknowledge the editorial assistance of James Kris Koford PhD, Department of Writing and Rhetoric studies, University of Utah.

References

[1] N. Goudarzi, W.D. Zhu, A Review of the Development of Wind Turbine Generators across the World 4 (PARTS a AND B), 2013, pp. 192–202.
[2] R. Wiser, M. Bolinger, Wind Technologies Market Report, Tech. Rep. August, U.S. Department of Energy (2015), 2014.
[3] M. Gryning, H.H. Niemann, M.P.S. Gryning, Q. Wu, M. Blanke, S. Member, Wind turbine inverter robust loop-shaping control subject to grid interaction effects, IEEE Trans. Sustain. energy 7 (1) (2016) 41–50.
[4] S. Wan, L. Cheng, X. Sheng, Effects of yaw error on wind turbine running characteristics based on the equivalent wind speed model, Energies 8 (7) (2015) 6286–6301.
[5] D. Shin, H. Kim, K. Ko, Analysis of wind turbine degradation via the nacelle transfer function, J. Mech. Sci. Technol. 29 (9) (2015) 4003–4010.
[6] B.J. Vanderwende, J.K. Lundquist, The modification of wind turbine performance by statistically distinct atmospheric regimes, Environ. Res. Lett. 7 (3) (2012) 1–7.
[7] T. Mikkelsen, N. Angelou, K. Hansen, M. Sjöholm, M. Harris, C. Slinger, P. Hadley, R. Scullion, G. Ellis, G. Vives, A spinner-integrated wind lidar for enhanced wind turbine control, Wind Energy 16 (2013) 625–643.
[8] G. Benedetti-Michelangeli, G. Congeduti, Fiocco, Measurement of aerosol motion and wind velocity in the lower troposphere by doppler optical radar, J. Atmos. Sci. 29 (1972) 906–910.
[9] G. Benedetti-Michelangeli, G. Congeduti, Fiocco, Determination of vertical eddy diffusion parameters by doppler optical radar, Atmos. Environ. 8 (1974) 793–799.
[10] E. Eloranta, J. King, J. Weinman, The determination of wind speeds in the boundary layer by monostatic lidar, J. Appl. Meteorol. 14 (1975) 1485–1489.
[11] G. Iungo, W. Yu-Ting, F. Porté-Agel, Field measurements of wind turbine wakes with lidars, J. Atmos. Ocean. Technol. 30 (2) (2012) 274–287.
[12] M. Harris, D. Bryce, A. Coffey, D. Smith, J. Birkemeyer, U. Knopf, Advance measurements of gusts by laser anemometry, Wind Eng. Industrial Aerodynamics 95 (2007) 1637–1647.
[13] E. Simley, L. Pao, R. Frehlich, B. Jonkman, N. Kelley, Analysis of wind speed measurements using continuous wave lidar for wind turbine control, in: A. Astronautics (Ed.), Proceedings of 49th AIAA Aerospace Sciences Meeting Including the New Horizons Forum and Aerospace Exposition, 2011.
[14] K. Kragh, P. Fleming, Rotor speed dependent yaw control of wind turbines based on empirical data, in: Proceedings of 50th AIAA Aerospace Sciences Meetings and Exhibit, American Institute of Aeronautics and Astronautics, 2012.
[15] K. Kragh, M. Hansen, T. Mikkelsen, Improving yaw alignment using spinner based lidar, in: Proceedings of 49th AIAA, Aerospace Sciences Meeting Including the New Horizons Forum and Aerospace Exposition, American Institute of Aeronautics and Astronautics, AIAA, 2011.
[16] D. Schlipf, J. Anger, S. Kapp, O. Bischoff, M. Hofsäß, A. Rettenmeier, M. Kühn, Prospects of optimization of energy production by lidar assisted control of wind turbines, in: Proceedings of European Wind Energy Conference and Exhibition, EWEA, 2011.
[17] P. a. Fleming, P.M.O. Gebraad, S. Lee, J.W. van Wingerden, K. Johnson, M. Churchfield, J. Michalakes, P. Spalart, P. Moriarty, Evaluating techniques for redirecting turbine wakes using SOWFA, Renew. Energy 70 (2014) 211–218.
[18] P.M.O. Gebraad, J.W. van Wingerden, A control-oriented dynamic model for wakes in wind plants, J. Phys. Conf. Ser. 524 (2014) 012186.
[19] M.J. Churchfield, P. Fleming, B. Bulder, S.M. White, Wind turbine wake-redirection control at the Fishermen's atlantic city Windfarm, in: Offshore Technology Conference, No. May, Offshore Technology Conference, 2015.
[20] K. a. Kragh, M.H. Hansen, T. Mikkelsen, Improving yaw alignment using spinner based LIDAR, in: AIAA Aerospace Sciences Meeting Including the New Horizons Forum and Aerospace Exposition (January), 2011, pp. 1–13.
[21] P. a. Fleming, a.K. Scholbrock, a. Jehu, S. Davoust, E. Osler, a.D. Wright, a. Clifton, Field-test results using a nacelle-mounted lidar for improving wind turbine power capture by reducing yaw misalignment, J. Phys. Conf. Ser. 524 (1) (2014) 012002.
[22] A. Scholbrock, P. Fleming, A. Wright, C. Slinger, J. Medley, M. Harris, Field test results from lidar measured yaw control for improved yaw alignment with the NREL controls, Adv. Res. Turbine Prepr. (2014) 1–9.
[23] G. Svensson, A.A.M. Holtslag, Single column modeling of the diurnal cycle based on CASES99 data - GABLS second intercomparison project, in: 17th Symposium on Boundary Layers and Turbulence, 2006, pp. 22–25.
[24] V. Kumar, J. Kleissl, C. Meneveau, M.B. Parlange, Large-eddy simulation of a diurnal cycle of the atmospheric boundary layer: atmospheric stability and scaling issues, Water Resour. Res. 42 (2006) 1–18.
[25] V. Kumar, G. Svensson, a. a. M. Holtslag, C. Meneveau, M.B. Parlange, Impact of surface flux formulations and geostrophic forcing on large-eddy simulations of diurnal atmospheric boundary layer flow, J. Appl. Meteorol. Climatol. 49 (2010) 1496–1516.
[26] V. Sharma, M. Calaf, M. Lehning, M.B. Parlange, Time-adaptive wind turbine model for an les framework, Wind Energy 19 (5) (2016) 939–952.
[27] P.Y. Orzag SA, Numerical computation of turbulent shear flows, Adv. Geophys. 1 (224) (1974) 225–236.
[28] E. Bou-Zeid, C. Meneveau, M. Parlange, A scale-dependent Lagrangian dynamic model for large eddy simulation of complex turbulent flows, Phys. Fluids 17 (2) (2005) 1–18.
[29] M. Calaf, M.B. Parlange, C. Meneveau, Large eddy simulation study of scalar transport in fully developed wind-turbine array boundary layers, Phys. Fluids 23 (12) (2011).
[30] Y.-T. Wu, F. Porté-Agel, Large-eddy simulation of wind-turbine wakes: evaluation of turbine parametrisations, Boundary-Layer Meteorol. 138 (3) (2010) 345–366.
[31] C.-h. Moeng, A large-eddy-simulation model for the study of planetary boundary-layer turbulence, J. Atmos. Sci. 41 (13) (1984) 2052–2062.
[32] J.D. Albertson, M.B. Parlange, Natural integration of scalar fluxes from complex terrain, Adv. Water Resour. 23 (3) (1999) 239–252.
[33] M. Frigo, S.G. Johnson, The design and implementation of FFTW3, Proceed. IEEE 93 (2) (2005) 216–231.
[34] C. Canuto, M.Y. Hussaini, A. Quarteroni, T.A. Zang, Spectral Methods in Fluid Dynamics, Springer Berlin Heidelberg, Berlin, Heidelberg, 1988.
[35] A Higher-Order Compact Method in Space and Time Based on Parallel Implementation of the Thomas Algorithm, Journal of Computational Physics 161(1) (2000) 182–203.
[36] M.B. Parlange, W. Brutsaert, Regional shear stress of broken forest from radiosonde wind profiles in the unstable surface layer, Boundary-Layer Meteorol. 64 (4) (1993) 355–368.
[37] M. Hultmark, M. Calaf, M.B. Parlange, A new wall shear stress model for atmospheric boundary layer simulations, J. Atmos. Sci. 70 (11) (2013) 3460–3470.
[38] W. Brutsaert, M.B. Parlange, The unstable surface layer above forest: regional evaporation and heat flux, Water Resour. Res. 28 (12) (1992) 3129–3134.
[39] W. Brutsaert, M.B. Parlange, J.H.C. Gash, Neutral humidity profiles in the boundary layer and regional evaporation from sparse pine forest, Ann. Geophys. 7 (1989) 623–630, 623–630, 7.
[40] W. Brutsaert, Hydrology: an Introduction, Cambridge University Press, 2005.
[41] A.C. Fitch, J.K. Lundquist, J.B. Olson, Mesoscale influences of wind farms throughout a diurnal cycle, Mon. Weather Rev. 141 (2013) 2173–2198.
[42] V. Sharma, M.B. Parlange, M. Calaf, Perturbations to the spatio-temporal characteristics of a diurnal abl due to an idealised wind-farm, Bound. Layer. Meteorol. (2016), http://dx.doi.org/10.1007/s10546-016-0195-0.

[43] M. Calaf, C. Meneveau, J. Meyers, Large eddy simulation study of fully developed wind-turbine array boundary layers, Phys. Fluids 22 (1) (2010) 015110.
[44] [online] (2015). [link].
[45] [online] (2015). [link].
[46] [online] (2015). [link].
[47] E. Simley, L.Y. Pao, P. Gebraad, M. Churchfield, Investigation of the impact of the upstream induction zone on lidar measurement accuracy for wind turbine control applications using large-eddy simulation, J. Phys. Conf. Ser. 524 (1) (2014) 012003.
[48] F. Porté-Agel, Y.-T. Wu, C.-H. Chen, A numerical study of the effects of wind direction on turbine wakes and power losses in a large wind farm, Energies 6 (10) (2013) 5297–5313.
[49] H. Lu, F. Porté-Agel, On the impact of wind farms on a convective atmospheric boundary layer, Boundary-Layer Meteorol. 157 (1) (2015) 81–96.
[50] B. Witha, G. Steinfeld, M. Dörenkämper, D. Heinemann, Large-eddy simulation of multiple wakes in offshore wind farms, J. Phys. Conf. Ser. 555 (1) (2014) 012108.
[51] W. Gutierrez, G. Araya, S. Basu, a. Ruiz-Columbie, L. Castillo, Toward understanding low level jet climatology over west Texas and its impact on wind energy, J. Phys. Conf. Ser. 524 (2014) 012008.
[52] N.G. Nygaard, Wakes in very large wind farms and the effect of neighbouring wind farms, J. Phys. Conf. Ser. 524 (1) (2014) 012162.
[53] R.J. Barthelmie, S.T. Frandsen, O. Rathmann, K. Hansen, E.S. Politis, J. Prospathopoulos, J.G. Schepers, K. Rados, Flow and Wakes in Large Wind Farms : Final Report for UpWind WP8 Risø-r-report, 2011. Vol. Risø-R-Rep.
[54] H. Lu, F. Porté-agel, Large-eddy simulation of a very large wind farm in a stable atmospheric boundary layer, Phys. Fluids 23 (6) (2011) 065101.
[55] F. Porté-Agel, H. Lu, Y. Wu, Interaction between large wind farms and the atmospheric boundary layer, Procedia IUTAM 10 (0) (2014) 307–318.

CHAPTER 3

TURBULENCE UPSTREAM OF WIND TURBINES: A LARGE-EDDY SIMULATION APPROACH TO INVESTIGATE THE USE OF WIND LIDARS

Renewable Energy (2017) 105, 354-365. Turbulence upstream of wind turbines: A large-eddy simulation approach to investigate the use of wind LIDARs. G. Cortina, M. Calaf.

Renewable Energy 105 (2017) 354–365

Contents lists available at ScienceDirect

Renewable Energy

journal homepage: www.elsevier.com/locate/renene

Turbulence upstream of wind turbines: A large-eddy simulation approach to investigate the use of wind lidars

G. Cortina*, M. Calaf

Department of Mechanical Engineering, University of Utah, UT, USA

ARTICLE INFO

Article history:
Received 17 June 2016
Received in revised form
26 October 2016
Accepted 26 December 2016
Available online 28 December 2016

Keywords:
Large eddy simulation
Lidar
Wind energy
Wind farm
Wind turbines
Turbulent kinetic energy

ABSTRACT

Despite the evolution of wind turbines, the way in which in-situ meteorological information is obtained has not evolved much. Wind vane and cup anemometers, installed at the turbines nacelle, right behind the blades, are still used. This near-blade monitoring does not provide any time to readjust the profile of the wind turbine, and subjects the blades and structure to wind gusts and extreme incoming wind conditions. A solution is to install wind lidar devices on the turbine's nacelle. This technique is currently under development as an alternative to traditional in-situ wind anemometry because it can measure the wind vector at substantial distances upwind. However, most used wind lidar systems are optimized for measuring within a fixed upwind range, but at what upwind distance should they interrogate the atmosphere? This work uses Large Eddy Simulations to create a realistic atmospheric flow to evaluate optimal scanning distances to learn about the incoming turbulence as a function of wind farm configuration and atmospheric stratification. A correlation model, based on a modified truncated normal distribution, has also been developed, which could be implemented within the feed-forward collective pitch control of the turbine, allowing for improved wind turbine readjustments.

1. Introduction

The continuous improvement of Light Detection and Ranging (lidar) technology over the past few years, with enhanced spatio-temporal resolution, improved signal-to-noise ratio, and considerable reduction of the physical package, has made this technology very appealing for wind energy applications. For example, several studies have illustrated the lidars' capacity to provide more accurate measures of the turbine's approaching wind vector in comparison to traditional wind vane and cup anemometers [1–3]. With this new capacity of staring ahead of the turbine's rotor blades, it is possible to improve the turbine's yaw alignment [4,5], and therefore enhance the turbine's harvested power [2,6]. In addition, wind lidars have also improved the measure of power curves [7,8] and the prediction of incoming flow turbulence [9], which results in a potential mitigation of the turbines' loads.

To study the detection of wind gusts, Harris et al. [9] installed a wind lidar on the nacelle of a 2.3 MW turbine. The wind measurements were performed at a constant upstream scanning distance of two-hundred meters for a period of 18 h. By comparing the lidar measurements with those provided by cup anemometers, they illustrated the potential of nacelle-mounted wind lidars to accurately measure incoming wind gusts. Other studies have focused on the use of wind lidars to enhance the harvested power by continuously readjusting the turbine's yaw alignment [2], and in designing collective pitch controls [10,11] to reduce the loads that wind turbines suffer from incoming turbulent gusts. By being able to measure the incoming flow ahead of time, it is, for example, possible to design control mechanisms that force certain wind turbines of a wind farm to be purposely yaw-misaligned, reducing the wake-to-wake interaction with downstream turbines [12]. This is for example the purpose of the control-oriented dynamic model proposed by Gebraad and Van Wingerden [13], or the approach explored by the National Renewable Energy Laboratory (NREL) at the Fishermens Atlantic City Windfarm. In this last case, an increase of 10% in power output for the overall wind farm and a reduction in successive wake-turbine interactions were reported [14]. Another approach, currently being explored, to enhance the wind farm power production, knowing the incoming wind vector ahead of time, is the use of collective pitch control algorithms. These have the advantage of not increasing the turbine's structural loads (as compared to the yaw-misalignment approaches [10]). Yet, this approach has only been explored under deterministic gust conditions, assuming perfect inflow measurements, and applying

* Corresponding author.
E-mail address: gerard.cortina@utah.edu (G. Cortina).
URL: http://wet.mech.utah.edu/

http://dx.doi.org/10.1016/j.renene.2016.12.069
0960-1481/

Taylor's frozen turbulence hypothesis. Similarly, numerical works from Dunne et al. [15] have also illustrated the potential of using a wind lidar control approach to reduce loads while maintaining rated power and rotor speed, and at the same time without significantly increasing the pitch rate.

Currently it is possible to readjust the pitch of the turbine's blades at a rate of 4–8°/s [10,16], meaning that with a sufficient warning-time, it should be possible to readjust the blades', reducing the structural loads produced by wind gusts. According to Mikkelsen et al. [3], the 'warning' time for the incoming winds gusts is of 5–10 s, depending on the mean incoming wind velocity. Therefore, the potential of using wind lidars to predict the incoming turbulent flow relies on the time-lapse with which turbulent events can be predicted before these reach the turbine blades. At this point, while the lidar-assisted collective pitch control and the pitching system have been proved to be fast enough to regulate the wind turbine [10,16], several questions remain to be answered with respect to the evolution of the turbulent flow within wind farms. For example, how far upstream should the wind lidars measure to observe rotor-disk correlated turbulence, and how does this upstream correlation distance change with atmospheric stratification?

In this work we explore the correlation between the rotor-disk and the upstream measured turbulence fields in a wind farm under different atmospheric stability conditions. The goal is to determine whether it is possible to timely readjust the turbine blades to protect them from potentially damaging turbulent gusts. For this purpose a set of atmospheric large-eddy simulations (LES), including wind turbines capable of yaw self-adjustment, has been considered. The atmospheric flow was forced with a constant geostrophic wind and a time varying surface temperature extracted from the Cooperative Atmospheric Surface Exchange Study (CASES-99) field experiment [17], hence reproducing a realistic diurnal cycle. The effectiveness of measuring the flow upstream of the wind turbine to predict incoming turbulence gusts is quantified, and correlation curves are developed to help wind turbine operators select the most appropriate upstream scanning distance for nacelle mounted wind lidars as a function of atmospheric stratification.

In section 2 the considered study cases are explained, and in section 3 the results are presented and discussed. In section 4 a simple model to predict turbulent gusts is presented and section 5 outlines the conclusions. Additional details of the numerical configuration can be found in the Appendix section.

2. Study cases

To numerically simulate the atmospheric boundary layer flow throughout a diurnal cycle, the filtered Navier-Stokes equations (NS) with conservation of mass, and an advection-diffusion equation for potential temperature are integrated in time. The atmospheric boundary layer (ABL) flow is considered incompressible and as a result of the high Reynolds number, the viscous terms are neglected. The wind turbines are represented with the actuator-disk model with rotation of Wu et al. [18], including the dynamic yaw-alignment of Sharma et al. [19], where the turbines have the capacity to realign their yaw alignment every 10 min. The numerical domain has a physical size of $L_x = 2\pi z_i$ m, $L_y = \pi z_i$ m, and $L_z = 3z_i$ m, where z_i is the height of the inversion layer. The grid resolution is equal to $d_x = d_y = 24.5$ m and $d_z = 7.8$ m, with a total of $256 \times 128 \times 384$ grid points, providing a large enough domain for developing realistic ABL flow conditions [20,21]. Also, this numerical resolution is fine enough to accurately resolve the wind turbines and the corresponding wakes [22]. For each diurnal cycle the associated computational cost is approximately 33,000 core hours. In this study, each simulation used 64 cores, hence leading to a total of about 21 days. The specific details of the numerical code are found in the Appendix as well as in prior studies from the same authors [1,19,21].

To evaluate the possibility of using nacelle-mounted wind lidars to foresee strong incoming turbulence ahead of time, two different wind farm scenarios with different wind turbine spacings have been considered. Each wind farm configuration has been evaluated through two consecutive diurnal cycles. First, a very large wind farm (VLWF) is considered, where the turbines are perfectly aligned and separated by a distance of $\sim 8D$ in the streamwise direction (s_x) and $\sim 5D$ in the spanwise direction (s_y). Second, a very sparse wind farm representative of the case of an isolated single wind turbine is also considered, where the turbines are in practice separated by a distance of $s_x \sim 63D$ and $s_y \sim 31D$, and referred as largely-spaced wind farm (LSWF).

The simulations were initialized with vertical profiles of velocity and temperature extracted from Kumar et al. [23], corresponding to a height-independent geostrophic wind, and a well mixed temperature profile matching the initial surface temperature of 278.6K, with an inversion layer spanning from z_i to the top of the domain, with $z_i = 1000m$. To simulate a diurnal cycle, a time varying surface temperature is imposed (see Fig. 1a). Specifically

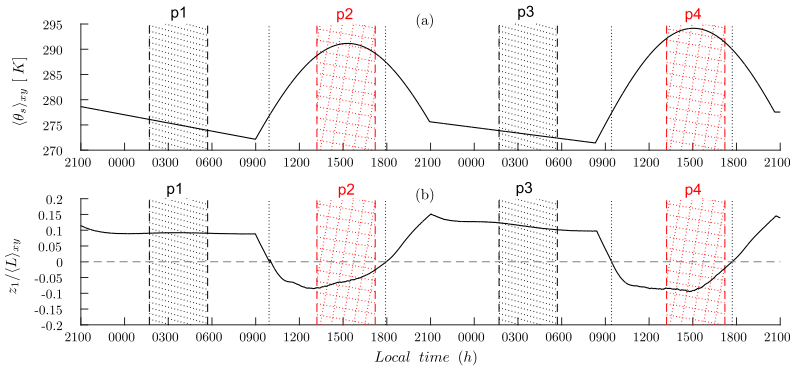

Fig. 1. (a) Spatially averaged and time-dependent imposed temperature at the surface of the domain $\langle\theta_s\rangle_{xy}$ [K]; (b) normalized stability parameter, $z_1/\langle L\rangle_{xy}$, where z_1 is the height of the first grid-point and L is the Monin-Obukhov length as a function of time. Four-hour periods marked with 45° dotted line (p1, p3), in black, and squared dotted line (p2, p4), in red, delineate time periods in which representative statistics are computed. Precisely, period p1 and p3 constitute the times between 0145 and 0545 h local time (LT) and p2 and p4 denote the time between 1315 and 1715 h of LT. (For interpretation of the references to colour in this figure legend, the reader is referred to the web version of this article.)

in this work two consecutive diurnal cycles are modelled, to ensure uniformity of the results presented and improve statistics. The imposed surface temperature is spatially homogeneous for the entire domain and as a result of the time variation, different stability conditions are achieved through the two diurnal cycles as depicted in Fig. 1b using the surface stability parameter (z_1/L). In this case z_1 represents the height of the first grid point and L is the Obukhov length, such that

$$\frac{z_1}{\langle L\rangle_{xy}} = \left\langle \frac{-kz_1 g\overline{(w'\theta')}_s}{\overline{\theta}u_*^3} \right\rangle_{xy}. \quad (1)$$

Here, the left and right triangular brackets ($\langle\cdot\rangle_{xy}$) indicate spatial averaging in the stream and spanwise directions. Also, k is the von Kármán constant, $\overline{(w'\theta')}_s$ is the surface sensible heat flux, $\overline{\theta}$ is the surface temperature, and u_* is the friction velocity. In Fig. 1b, the vertical doted lines denote a change in atmospheric stability. From 2100 to 0955 h the stability parameter is positive ($z_1/\langle L\rangle_{xy} > 0$), which means that the ABL flow is stable. Whereas between 0955 and 1842 the stability parameter is negative ($z_1/\langle L\rangle_{xy} < 0$), indicative of unstable stratified flow, hence representative of a convective atmospheric boundary layer (CBL). The same pattern develops in the second diurnal cycle, where the change of stability takes place at 0925 and 1842h, local time. Four-hour periods marked with 45° dotted lines and denoted as period 1 and period 3 (p1, p3), in black, and squared dotted lines for periods 2 and 4 (p2, p4), in red, delineate the times in which representative statistics of both stratification regimes are computed. Periods p1 and p3 constitute the time between 0145 and 0545 h and p2 and p4 denote the time between 1315 and 1715 h, local time. Within these stratification periods, the flow remains fairly unchanged from a statistical perspective.

2.1. The very large wind farm (VLWF)

The VLWF case is populated with 48 wind turbines uniformly spread in 8 rows of 6 wind turbines each, with a diameter and hub height of one hundred meters ($z_h = D = 100m$). As a result of the lateral periodic boundary conditions, the VLWF case is equivalent to an infinite wind farm. To evaluate the flow differences obtained by measuring the incoming wind field at different upstream distances, each row of turbines is configured with a different upstream scanning distance. Fig. 2a is a schematic representation of the wind farm configuration with color bands representing the different upstream scanning distances for each turbine. Specifically, the wind turbine rows scan at $D/4, D/2,\ 3D/4,\ D,\ 5D/4,\ 3D/2$ and $2D$ upstream of the rotor disk. These upstream scanning distances have been selected following a previous experimental study of Harris et al. [9], where a continuous-wave wind lidar was ranged between 10 and 200 m upstream of the wind turbine rotor disk. Fig. 2b is a detailed view of one of the wind turbines, where the cone shape denotes the upstream scanning distance (d_u) and ϕ_e represents the yawing alignment and correspondingly the orientation of the upstream scanning location.

2.2. The largely spaced wind farm (LSWF)

The LSWF consists of one single wind turbine located in the middle of the numerical domain. Due to the periodic boundary conditions, in practice this is equivalent to a largely spaced wind farm with a streamwise and spanwise spacing of approximately 63D and 31D, respectively. Hence, it is assumed to be representative of an isolated wind turbine. Note that given the size of the numerical domain, although it is periodic, the wake of the wind turbine doesn't interact with itself, meaning that in practice it perfectly corresponds to the case of a single wind turbine. In this case, however, given the computational cost of each simulation, only 4 upstream scanning configurations have been considered ($D/2,\ D,\ 3D/4$, and $4D/2$). Note that for each upstream scanning configuration 48 h of real time flow have been simulated.

3. Results

3.1. Mean velocity and turbulent kinetic energy throughout a diurnal cycle

Fig. 3 represents the corresponding diurnal evolution of the horizontally averaged wind velocity module ($U = \sqrt{u^2 + v^2}$, sub-plots a and b) and turbulent kinetic energy ($TKE = 0.5(\overline{u'u'} + \overline{v'v'} + \overline{w'w'})$, sub-plots c and d) for the VLWF case (a and c) and the LSWF case (b and d). Both, the mean wind velocity and the TKE are computed using a weighted moving average with a window size of 10 min. This becomes important later, when computing the space correlations of TKE between the rotor-disk measures and those made upstream. Precisely, the velocity fluctuations are computed by subtracting to the instantaneous velocity ($u(t)$) a 10 min time average

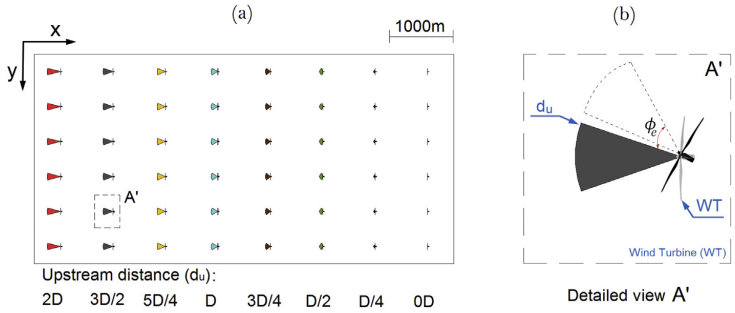

Fig. 2. (a) Top view representation of the LES domain with the eight rows of wind turbines for the VLWF case, where the different upstream scanning distances of each row are represented with a different scanning cone size and a different color. (b) Detailed view of A′, indicating the upstream scanning region as a function of changing yaw angle (ϕ_e). (For interpretation of the references to colour in this figure legend, the reader is referred to the web version of this article.)

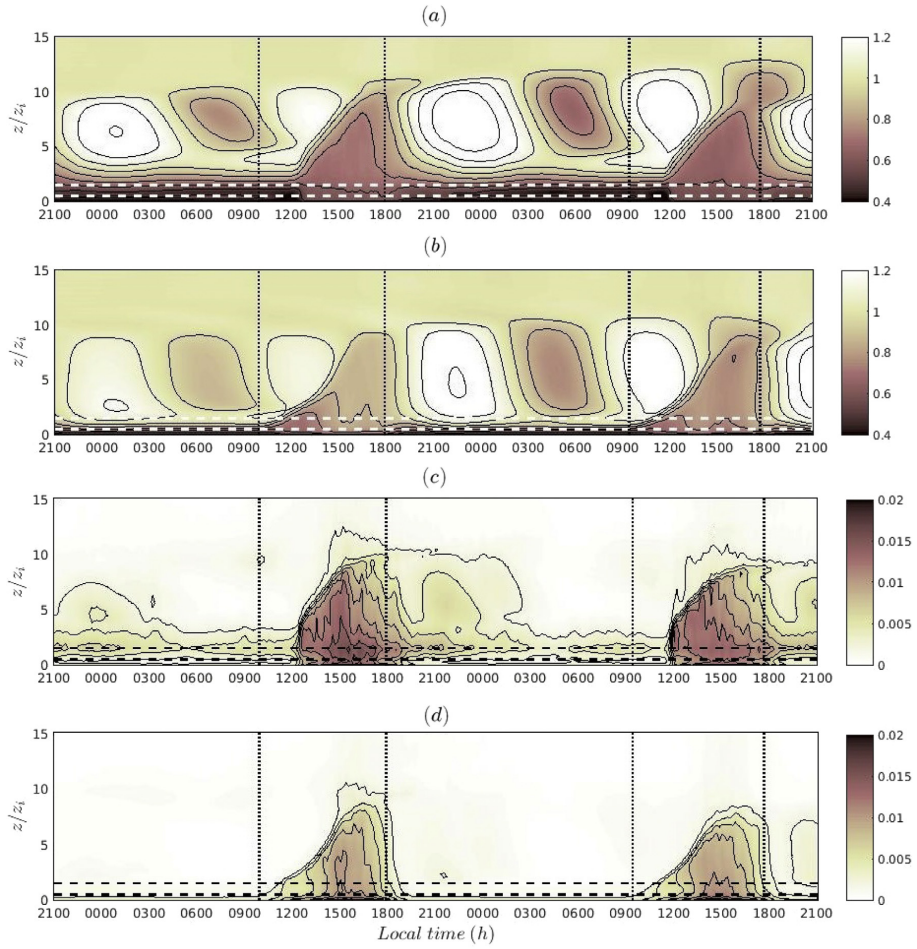

Fig. 3. Sub-plots a and b represent the vertical profiles of 10 min averaged and horizontally averaged velocity module ($\langle \overline{U} \rangle_{xy}$). Sub-plots c and d represent the turbulent kinetic energy ($\langle \overline{TKE} \rangle_{xy}$), representative of the VLWF (sub-plots a and c) and the LSWF (sub-plots b and d) during two consecutive diurnal cycles. The vertical dotted lines denote the change in stability and the horizontal dashed lines denote the top tip and bottom tip of the rotor of the wind turbine. Both cases are correspondingly normalized with the geostrophic wind (U_G) and the square of the geostrophic wind.

($u'(t) = u(t) - \overline{u}$) computed using an exponentially weighted moving average (EWMA, [24]). The averaging function is represented as follows,

$$\overline{u}(t;\tau) = \frac{1}{\tau} \int_{t-\tau}^{t} u(t)\omega(t-t')dt', \tag{2}$$

where the weighting function used is a decaying exponential, $w(t-t') = e^{-(t-t')/\tau}$. This weighting function is introduced to control the relative importance of events near time t with those of earlier times t', where $t' < t$. While traditionally the most common averaging techniques used to study atmospheric processes are the window average and the moving window average, these require knowing the complete time-series to compute the actual averaged quantity (these are a-posteriori averaging techniques). However to continuously obtain a measure of the incoming turbulence as needed to compute correlations at each instant in time, a continuous running averaging procedure is needed, hence the use of the EWMA. Note that as a result of the weighting function used, the fluctuating velocity is computed as a function of the past flow events, with stronger influence of the latest wind measures. In principle, the time averaging period (τ) used to compute the fluctuations of the velocity field and the corresponding TKE, should a-priory be atmospheric-stratification dependent because of the non-stationary behaviour of the turbulent flow through the diurnal cycle. Several works have investigated the use of different mathematical approaches such as the eddy covariance method [25], the Ogive function [26] and the Multiresolution flux decomposition [27], among others, to determine the most appropriate averaging time to compute statistics in turbulent flows. For example, Sozzi and Favaron [28] found that a time scale ranging between 30 and 60 min was a good averaging time under convective conditions. Also, under convective conditions, over the Salt Flats in Utah's

western desert, Metzger and Holmes [29] found that the appropriate mean removal time scale was in the range of 20.8 and 26.7 min. Instead, under a neutral stratification Vickers and Mahrt [27] found that the appropriate averaging time was of 9 min, and under stable stratified flows Babić et al. [30] suggested that a good averaging time scale should range between 7 and 11.5 min. In this work, the averaging time scale (τ) used to compute the velocity fluctuations, the corresponding TKE and the mean velocity is equal to 10 min. This time-scale has been chosen in accordance with the selected yaw reorientation-time. While this averaging time, might be a bit too short to capture the large-scale structures of the convective stratification as mentioned above, it wouldn't make sense to carry on statistics of turbulent flow from different directions. Further, the selected, fixed averaging time is inline with those suggested for neutral and stable conditions.

In Fig. 3b, the flow statistics of the evening period (between 21:30 and 04:00 h) illustrate the presence of an intense low-level jet (LLJ) at about 100 m height. Interestingly, in the VLWF case the LLJ is displaced vertically by almost 200 m, hence avoiding direct interaction with the turbines. This vertical shift is the result of an increased surface drag produced by the agglomeration of turbines and illustrated in the form of an increased TKE in 3c. As a result, since the harvested power is proportional to the cube of the averaged velocity, the harvested power for the VLWF case would be substantially reduced ($\sim$ 80% reduction) with respect to the LSWF case, during the night-time. During the convective regime (from 0925 to 1842h), this reduction in power is only of about $\sim$ 50%. Also, during this period it is important to notice the vertical growth of the surface boundary layer (10% increase), when compared to the LSWF case. This results once more, from the increase in TKE throughout the wind layer surrounding the turbines and extending vertically up to 400 m height. During night-time, the large array of turbines becomes the main generator of turbulence, dominating over the otherwise shallow turbulent layer formed near the surface and observed in the LSWF. Interestingly, during the convective regime the flow is mainly dominated by the background atmospheric turbulence (as will be shown later), and hence flow differences between the VLWF and the LSWF cases are much smaller.

As it can be observed in all sub-plots, both diurnal cycles present very similar trends, with minimal changes in magnitude for any of both variables. However, there exists a weak increase in the boundary layer depth (165 m and 149 m growth for the VLWF and LSWF, respectively) during the convective period of the second day in comparison to the first day. This results from the residual layer of the prior day.

Note that Fig. 3 is solely intended to provide a time evolution representation of the mean velocity and TKE, so the reader becomes familiarized with the tempos of the diurnal cycle and the progressive vertical changes in both variables as the day evolves. A much more detailed analysis of the diurnal evolution of the ABL, in presence of wind turbines, is provided by other LES works [21,31], and mesoscale simulations [32].

Using a different perspective, Fig. 4 presents a detailed time evolution of the TKE focusing now at the rotor-disk area. While the central lines (hollow circles and stars) represent the rotor-disk area averaged TKE, the top and bottom solid lines represent the TKE at $z = \pm D/2$, hence indicative of the vertical variation of TKE on the rotor-disk region. Note that during night-time and for the VLWF case, there exists a 2.7 difference in turbulence intensity between the top tip and the bottom tip of the rotor-disk. In contrast, during day time the vertical change in TKE is reduced to a factor of only 1.15, meaning that the turbulence is vertically well homogeneous. While overall the TKE is much weaker during night time, this vertical gradient throughout the rotor-disk is of big concern for wind turbine operators because of the resultant enhanced blade loads. With respect to the LSWF case, the TKE remains fairly uniform through the rotor-disk region and through all the diurnal cycle.

3.2. Correlation of rotor-disk and upstream turbulence

To quantify the resemblance between the rotor-disk reaching turbulence and the upstream measured one, a time-lag cross-correlation coefficient between the TKE measures at both locations (see Fig. 5) has been computed following Equation (3). Using this cross-correlation coefficient it will be possible to set a measure of relationship between the rotor-disk and the upstream TKE. Fig. 5 presents a schematic representation of the procedure followed to compute the TKE correlation. Sub-plot (a) depicts the wind turbine and the corresponding upstream scanning area, where the wind velocity fluctuations are measured and used to compute the TKE as a function of time. Initially, the TKE is computed individually at each grid point (i,j) of the rotor disk and the upstream scanning area using the 10 min weighted moving average. In a second step it is spatially averaged over each corresponding scanning area. As a result, a single TKE value is obtained per sampling time (sampling frequency of 1 Hz). The spatial distribution of grid points (i,j) corresponds with future wind lidar models, which will be adapted to scan full circular upstream planes. These are currently being developed and tested (Mikkelsen et al. [3]). In a third step, the correlation coefficient between the rotor-disk and upstream averaged TKE values is computed following a traditional approach,

$$R = \frac{C\left(e^d, e^u\right)}{\sqrt{C\left(e^d, e^u\right) C\left(e^d, e^u\right)}}, \tag{3}$$

where R represents the correlation coefficient. The corresponding covariance ($C(e^d, e^u)$) between the rotor-disk ($e^d(t)$) and the upstream TKE ($e^u(t)$) time-series is computed using 4 min chunks of

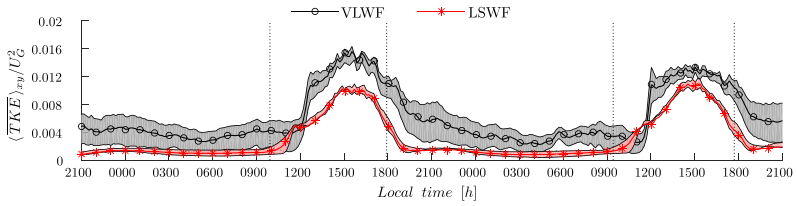

Fig. 4. Ten minutes averaged turbulent kinetic energy ($\langle \overline{TKE} \rangle$) for the VLWF and the LSWF cases during the two diurnal cycles, normalized by the square of the geostrophic wind. The line represented by circles and stars illustrate the volume average of the TKE between the top tip and bottom tip of the wind turbine's rotor. The lines surrounding the filled area depict the TKE averaged at the top and bottom tip of the wind turbine blades, $+D/2$ and $-D/2$, respectively.

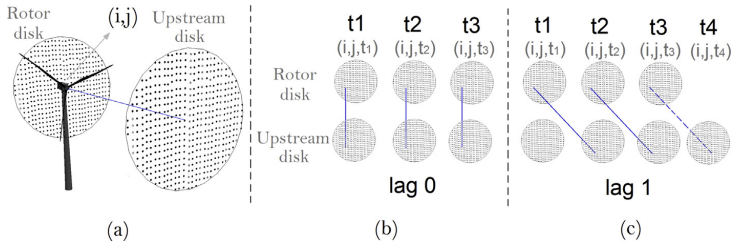

Fig. 5. Graphical representation of the computation of the lag-cross-correlation coefficient for the TKE between the rotor disk and the upstream disk for the different lags.

data, with a 50% overlap. Precisely, the covariance is computed as follows,

$$C\left(e^d, e^u\right) = \frac{1}{N-1}\sum_{i=1}^{N}\left(e_i^d - \mu^d\right)*\left(e_i^u - \mu^u\right), \tag{4}$$

where μ^u and μ^d are the corresponding time averages of the time varying TKE upstream and at the rotor-disk, and $(*)$ denotes the complex conjugate. In the above equation, N represents the total number of sampling points used at each plane. The 4 min period with 50% overlap used to compute the cross-correlations was selected upon the observation that beyond 2 min the TKE correlations are very weak. Initially, the correlation coefficient is computed for a lag-period equal to zero (see Fig. 5b and c), which is progressively increased up to the 2 min (4 min minus the 50% overlap). This procedure is progressively repeated in chunks of 4 min of data for each characteristic 4 h study periods (see Fig. 1) of each study case. At the end, all correlation coefficients of the same corresponding 4 h study periods are averaged to extract the most representative correlations for a given atmospheric stratification and wind farm arrangement. Results of the exhaustive analysis are presented in Fig. 6 for study periods p_1 and p_2 (see Fig. 1), where sub-figures (a) and (b) depict the stable- and unstable-VLWF cases, respectively, and sub-figures (c) and (d) depict the stable- and unstable-LSWF cases.

For the VLWF case it is interesting to note that the maximum correlation is strongly related with the time it takes for advection to displace the turbulent structures. This advection time scale (τ_a) is a function of the upstream velocity magnitude $\langle U_\infty \rangle_d = \langle \sqrt{u^2 + v^2} \rangle_d$ (where $\langle \cdot \rangle_d$ denotes the spatial average at the upstream disk) and the upstream scanning distance (d_u), such that $\tau_a = d_u / \langle U_\infty \rangle_d$. Therefore, because for the different upstream scanning distances the mean velocity remains fairly constant, the advection time at which the maximum correlation occurs is mainly only a function of the upstream scanning distance. Therefore the maximum correlation is equally spaced in time for the different upstream scanning distances in the VLWF case. This characteristic time scale is a good indicator of the reaction time that wind turbines will end up having to readjust the blades' pitch to reduce unwanted loads. Also, it should be noted that the turbulence correlation between the rotor-disk and the upstream scanning area decreases with increasing

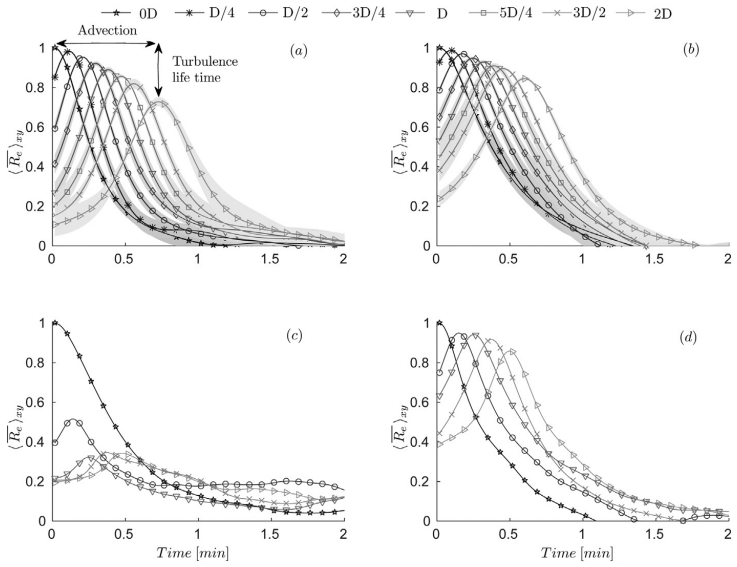

Fig. 6. Cross correlation coefficient for the different upstream scanning distances as a function of time, for the stable-VLWF (a), unstable-VLWF (b), stable-LSWF (c) and unstable-LSWF (d). For sub-figures (a) and (b) the correlation coefficient is averaged over the wind turbines scanning at the same upstream distance and the shaded area represents the standard deviation.

upstream scanning distance. This phenomena reflects the life-time of turbulence and is related to Taylor's frozen hypothesis [33]. For the stable-VLWF case (sub-Fig. 6a), the correlation of TKE has a constant drop of 4% for the first upstream scanning distances (between D/4 to 3D/2), while a more accentuated drop (9%) of TKE correlation exists at 2D. Contrary, for the unstable-VLWF case (sub-Fig. 6b), the TKE correlation presents a constant drop of 2%. The TKE correlation values for the unstable-LSWF represented in sub-Fig. 6d, seem to follow the same pattern as in the VLWF cases, with a total drop in correlation of 14% for the upstream distance of 2D. Overall, the VLWF (both stratification cases) and the unstable-LSWF depict very good correlations for the largest distance of 2D, with the maximum drop being 27% for the stable-VLWF case. Contrary, the lag-correlation coefficient curves for the stable-LSWF case depict a very different pattern. There exists already a very large drop of 50% in TKE correlation at the shortest upstream scanning distance (D/2), with also large differences at further distances (D, $5D/4$ and $2D$), ranging between 30 and 35%. To better understand the cause of this sudden drop in TKE correlation between the rotor-disk and the shortest upstream scanning distance, as well as to better compare the different TKE correlations, the corresponding TKE power spectra is computed at both locations, the rotor-disk and the upstream scanning area at $D/2$ (see Fig. 7). These power spectra are computed using the 4 min time series, at each point of the measuring disk, and then spatially averaged over the complete scanning disks, at the rotor and upstream. Sub-figure (a) illustrates the TKE spectra for the upstream plane and the rotor disk for the VLWF case, and sub-figure (b) illustrates the spectra for the LSWF cases. This representation illustrates better the difference in structure of the TKE, and justifies the severe difference in correlation previously observed in Fig. 6. It shows that for the stable-LSWF, the TKE power spectra between the rotor disk and the upstream disk is very distinct. Contrary, for the VLWF case independently of the ABL stratification, and for the unstable-LSWF, the two power spectra are practically identical. From the TKE spectra, it is observed that for the stable-LSWF case the TKE at the rotor disk is dominated by larger turbulent structures (low frequency), with two orders of magnitude more energy than for the TKE measured at D/2 upstream. This result could be induced by the effect of the wind turbine rotor blades. As it has been shown previously in Fig. 2b, during the stable-LSWF period, unlike the stable-VLWF case, the LLJ is intersecting the top-tip of the wind turbine rotor disk, causing a more intense induction zone in front of the rotor disk (see for example the study of Simeley et al. [34], which presents experimental results of the upstream induction zone for different flow stability patterns using a continuous-wave lidar). Without further proof, we attribute this to be the cause of the large difference in correlation happening at D/2 in the stable-LSWF. In parallel, it is interesting to note from these spectral representations that during day-time, and for both cases, the TKE spectra presents one order of magnitude larger values. This result is consistent with the results presented earlier in Fig. 3a and b. There, it was shown that for the VLWF, the wind turbines are the largest source of turbulence production. As a result, independently of the background atmospheric stratification, turbulence within the wind turbines' layer is dominated by rotor and wake generated turbulence, which becomes very homogeneous in very large wind farms. Therefore good TKE correlation values are obtained between the rotor-disk and any of the upstream scanning distances. Contrary, in the LSWF, each turbine behaves as a lone-standing element and hence the turbulence approaching the turbine is solely due to the background ABL turbulent flow. This presents large homogeneous turbulent values during daytime and small turbulence values, highly intermittent, during night-time. These last ones are very difficult to predict. The night-time turbulence deficit in correlation is a well known problem in atmospheric boundary layer turbulence [17,35].

To better understand the TKE correlation between the rotor-disk and an upstream scanning distance as a function of time throughout a diurnal cycle, the corresponding time-evolving peak of the correlation coefficient (maximum correlation value in Fig. 6) is represented in Fig. 8. Sub-Fig. 8a illustrates the maximum correlation coefficient for the VLWF case, where the maximum correlation coefficient is the average of the wind turbines configuring the same row, and therefore with the same upstream scanning distance. The shaded area depicts the standard deviation between those wind turbines. Sub-Fig. 8b illustrates the LSWF case. A common pattern can be observed throughout the diurnal cycle between both cases. In general, during stable stratified regimes the

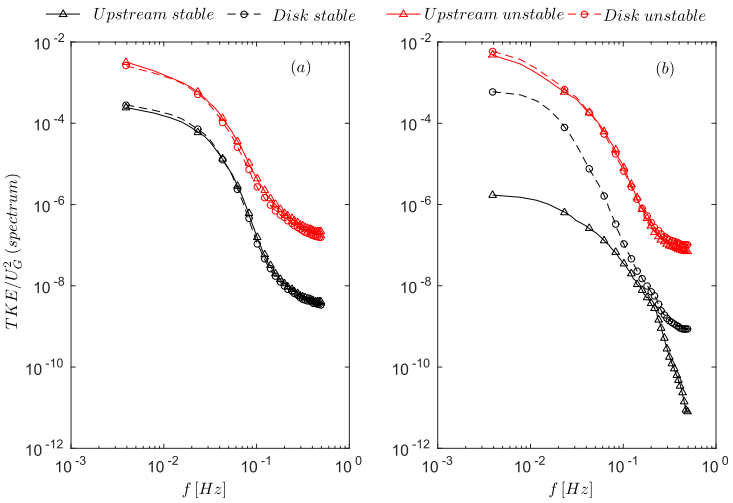

Fig. 7. Power spectra of the normalized TKE for the VLWF (a) and for the LSWF (b).

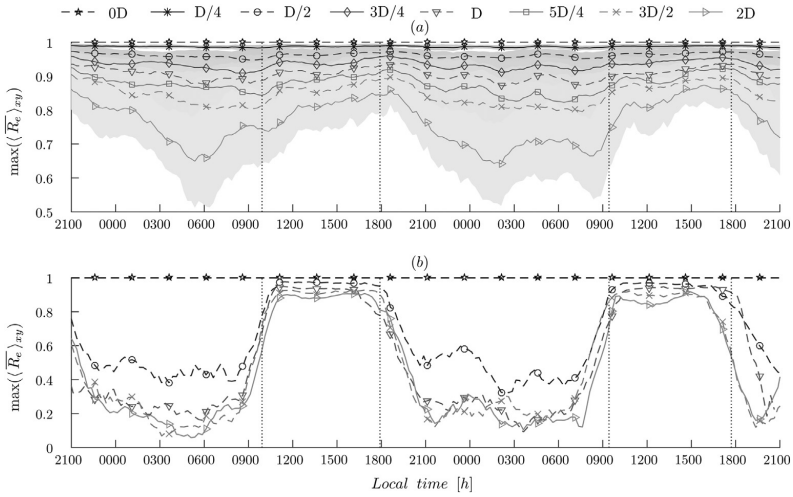

Fig. 8. Maximum correlation coefficient for the different upstream scanning distances as a function of time trough the two consecutive diurnal cycles for the VLWF (a) and the LSWF (b). For the sub-figure (a) the correlation coefficient is averaged over the wind turbines scanning at the same upstream distance and the shaded area represents the standard deviation. Notice that the scale of the vertical axis is different from (a) to (b).

TKE presents weaker correlations than during the unstable regime. As one would also expect, shorter upstream scanning distances present better TKE correlations. It is also interesting to note that for the VLWF case, the minimum correlation observed during daytime is 80%, on average for the 2D distance. Also, for the LSWF during the daytime, the correlations are above 85%, demonstrating that good predictions can be reached with the use of wind lidars. However, the night regime (or stably stratified) depicts very weak correlations, being the D/2 upstream distance more or less consistent with an average 50% correlation. With the larger upstream distances having average correlation values of only 20%.

The results shown in Figs. 6 and 8 outline the fact that during the unstable periods, independently of the wind farm case (VLWF or LSWF), the TKE presents the largest values, as well as the highest upstream correlations. This means that wind lidars would be able to foresee strong incoming TKE events, with efficiencies above 80% at upstream scanning distances of up to 200 m. For the stable periods, the turbulence in the VLWF is 4 orders of magnitude larger than for the single wind turbine case (see Fig. 4). Different to what happens during day-time, whereas the TKE measured in the VLWF case during stable periods can be predicted with good certainties (up to 70% for a distance of 2D upstream), for the stable-LSWF case it is very difficult to predict.

4. Truncated normal PDF stability dependent model

Within this section we investigate the possibility of developing an analytical expression that determines with certain accuracy the best upstream scanning distance to foresee rotor-disk turbulent events, accounting for the effect of atmospheric stratification. Ideally, this analytical expression should provide an upstream scanning distance provided some relevant wind farm characteristics and atmospheric stratification conditions. From the previous results, it is clear that the upstream scanning distance with stronger TKE correlation at the rotor-disk, is the closest distance possible, -i.e. $D/2$. However, such short distance provides almost no time for the wind turbine to respond accordingly. Hence, for this information to be useful, it needs to be provided with enough time-lag for the turbine to readjust. If t_r denotes the time that wind turbines need to measure the inflow conditions, process the data and re-adapt their pitch, then the condition $\tau_a = d_u / \langle U_\infty \rangle_d > t_r$, should be satisfied. This means that the upstream scanning distance should satisfy the condition where $d_u > t_r \langle U_\infty \rangle_d$. Therefore, the minimum upstream scanning distance (d_u) needed to guarantee enough time-lag should be determined as the averaged free stream velocity (U_∞) times the readjustment time (t_r). In addition, one should also include a *safety* factor γ, such to account for potential wind turbine delays or changes in the mean wind upstream of the turbine, hence $d_u \geq \gamma\, t_r \langle U_\infty \rangle_d$. For example, a $\gamma = 1.25$, would include a safety factor due to changes in the upstream wind of up to 25%.

The markers from Fig. 9 represent the same data from Fig. 6, corresponding to the LES obtained correlations. In addition, lines represent the adjustment of the LES correlation data using a one-sided truncated normal probability distribution function (one sided TN-PDF). While the range of definition of a normal PDF is between $-\infty$ and ∞, the one sided TN-PDF ranges between a lower limit a and ∞. Precisely, the lower TN-PDF can be represented by $\psi(\mu, \sigma, a; x)$, where μ and σ are the mean and variance of the parent or general normal PDF, and a specifies the lower truncation limit. Therefore, the TN-PDF can be evaluated as follows,

$$\psi(\mu, \sigma, a; t) = \begin{cases} 0 & \text{if } t \leq a \\ \dfrac{\psi(\mu, \sigma; t)}{\Psi(\mu, \sigma; \infty) - \Psi(\mu, \sigma; a)} & \text{if } t > a \end{cases} \tag{5}$$

where the TN-PDF is written as,

$$\psi(\mu, \sigma; t) = \frac{1}{\sigma\sqrt{2\pi}} exp\Big(- \frac{(t-\mu)^2}{2\sigma^2} \Big). \tag{6}$$

In the above equation, t represents the argument of the TN-PDF, which denotes time in minutes. To model the actual correlation functions showed in Fig. 6, two extra parameters have been

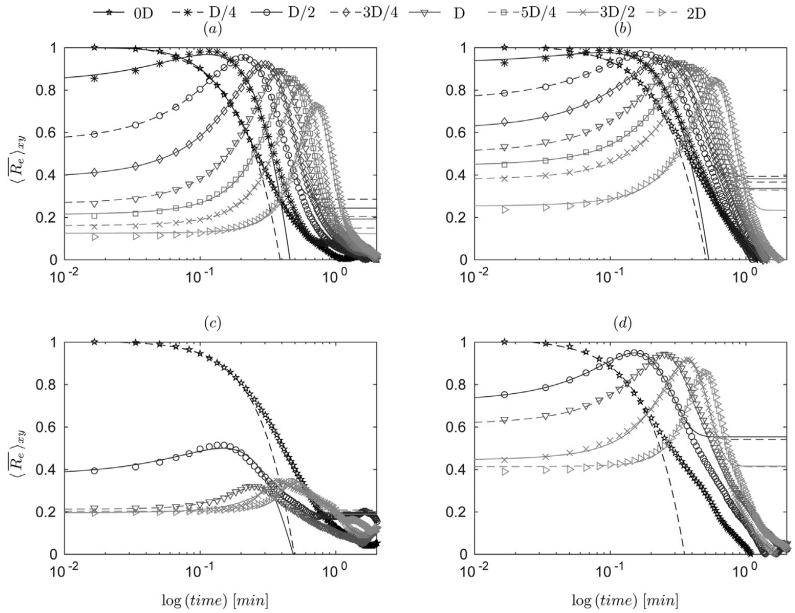

Fig. 9. Semi-logarithmic representation of the modelled truncated normal PDF functions fitting to the correlation coefficient curves for the different upstream distances and scenarios: VLWF (a) and (b) for stable and unstable, respectively; LSWF (c) and (d) for stable and unstable, respectively. Markers represent the same data from previous Fig. 6, which corresponding to the LES obtained correlations, and the lines represent the adjustment of the LES correlation data using a one-sided truncated normal probability distribution function (one sided TN-PDF).

introduced to scale the TN-PDF such that it fits the turbulent correlation functions,

$$\psi\left(\mu,\sigma,a,\lambda,\beta;t\right) = \frac{\lambda}{\sigma\sqrt{2\pi}} exp(-\frac{(t-\mu)^2}{2\sigma^2}\Big) + \beta, \tag{7}$$

with λ and β being the two new scaling parameters. Sub-Fig. 9a and b illustrate the stable and unstable stratification for the VLWF case, and sub-figures c and d present the stable and unstable stratification for the LSWF case. Note that the horizontal axis are represented in logarithmic scale to emphasize the adjustment of the maximum correlation peak. The solid lines represent the modified TN-PDF and the markers represent the data obtained from the lag cross-correlation coefficient computed for the distinct upstream scanning distances and represented in previous Fig. 6. Also note, that the corresponding fittings work very well with the upstream correlation measurements until the corresponding correlations drop to very small values. As a result, with the correct fitting parameters σ, μ, λ and β (represented in Fig. 10 for the current LES data analysis) the most appropriate upstream scanning distance, given a certain atmospheric stratification, could be determined ahead of time. Realize that these four parameters are wind farm dependent and can be easily determined on-site with nacelle mounted lidar measurements.

One of the properties of the probability distribution functions is that the area under the curve represents the total probability, and therefore it is equal to one. Instead, for the truncated normal PDF

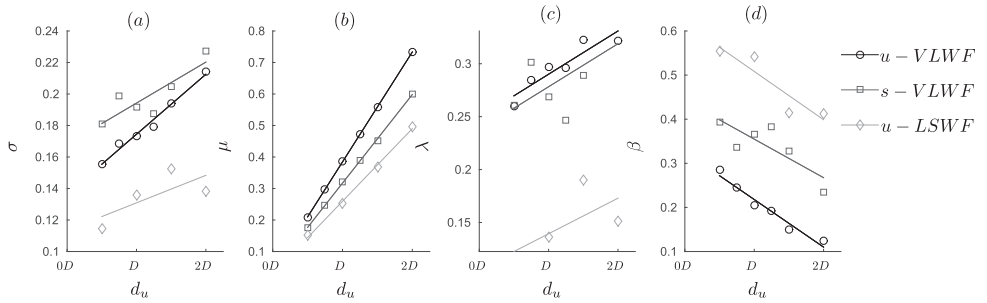

Fig. 10. Variables for the modified TN-PDF; (a) represents the standard deviation (σ), (b) represents the average (μ) and subplots (c) and (d) depict the scaling variables λ and β, correspondingly. Notice that there have been represented the unstable-VLWF ([o] *u − VLWF*), the stable-VLWF ([□] *s − VLWF*) and the unstable-LSWF ([◇] *u − LSWF*). Notice that the stable period for the LSWF has not been represented because it seems to not to be representative due to the poor correlations obtained.

the area under the curve is a partial representation of the total probability. Therefore expression 8 is used to properly normalize the modified TN-PDF,

$$\Psi(\mu,\sigma,\lambda,\beta;t) = \frac{\int_a^t (\psi(\mu,\sigma,\lambda,\beta;t))dt}{\Psi(\mu,\sigma,\lambda,\beta;\infty) - \Psi(\mu,\sigma,\lambda,\beta;a)}. \quad (8)$$

In this equation, the numerator is the area under the curve from the bounded limit a to the argument t, and the denominator represents the total area under the modified TN-PDF. As a result the probability of the modified TN-PDF is given by

$$P(\psi(\mu,\sigma,\lambda,\beta,a;t)) = \begin{cases} 0 & \text{if } t \le a \\ \dfrac{\psi(\mu,\sigma,\lambda,\beta;t)}{\Psi(\mu,\sigma\lambda,\beta;\infty) - \Psi(\mu,\sigma,\lambda,\beta;a)} & \text{if } t > a \\ 1 & \text{if } t \to \infty \end{cases} \quad (9)$$

from which results that ψ is equal to 0 at a and equal to 1 as the time t approaches ∞. For values of t in-between, the probability is simply a scaled and shifted version of a normal PDF. Within this probability function, the standard deviation (σ, sub-Fig. 10a) represents the spread or girth of the bell curve, indicative of the spread of the data, and it is indicative of the spread in foreseeing the incoming turbulence. The mean (μ, sub-Fig. 10b) indicates the upstream scanning distance where the maximum correlation coefficient is obtained, and it is related with the advection time (τ_a). The scaling parameter λ, (sub-Fig. 10d) readjusts the shape of the TN-PDF to obtain a more accurate fitting. Finally, parameter β (sub-Fig. 10b) indicates the vertical shift of the probability distribution, and it is a measure of the lifetime of the turbulence. Among the fitting parameters μ and β, seem to be the most important because they provide a measure of available reaction time t_r and the change in turbulence, respectively.

5. Summary and conclusions

In this work we have explored the effectiveness of detecting turbulent events at different upstream scanning distances using wind lidars mounted on the turbines' nacelle. The range of upstream scanning distances evaluated is between D/4 and 2D in accordance with previous experimental works. Two different study cases have been explored throughout a diurnal cycle, a very large wind farm (VLWF), and a largely spaced wind farm (LSWF). The first goal of this work was to quantify the effectiveness in measuring incoming turbulence at different upstream distances with sufficient time to readjust the wind turbine settings. The second goal was to create a turbulence correlation model, which could be implemented within the feed-forward collective pitch control of the turbine, allowing for improved wind turbine readjustments.

As one could expect, results illustrate the fact that scanning at different upstream distances changes the probability with which turbulence can be predicted. For the VLWF case under stable stratification, TKE correlations are minimum (65%) when scanning at the furthest upstream distance (2D), and maximum when measuring at the closest distance (D/4). A quasi linear decay in TKE correlation with changes in upstream scanning distance is observed. Overall, this case shows an average correlation of 80%. Under unstable stratification, the lowest TKE correlation is obtained when scanning at 2D upstream, with a value of $\sim$ 75%. At the closest scanning distance correlations are once again above 95%. At all upstream scanning distances, stronger correlations are observed during the convective regime, when TKE is much more intense and sustained in time, in comparison to the stable case; note that this plays in favour of using wind lidar technology to timely learn about incoming strong turbulent events. A stronger footprint of the diurnal variation in TKE correlation is observed for the LSWF case. In this case, during the unstable stratification a TKE correlation of about $\sim$ 85% is obtained when measuring at the furthest upstream distance. In contrast, only a 50% TKE correlation is measured for the closest upstream scanning distance of D/2, and even lower further upstream.

Wind turbines are modelled using the actuator-disk with rotation and yaw alignment of Sharma et al. [19], which means that the wind turbines timely align with the incoming wind vector, continuously changing the effective wind farm arrangement with atmospheric stratification. While we haven't run any simulation with an initially staggered wind farm configuration, as a result of the atmospheric stratification wind turbines continuously change their yaw angle, specially during the unstable regimes. Additionally, during the stable regimes turbulence is overall weak, and correlations decay really fast. Hence, we believe that the correlations presented in this study shouldn't change much with initial wind farm arrangement (staggered versus aligned). Given the recent results from a finite size wind farm [36,37], we expect the correlations presented in this work no to change much except for the first rows of wind turbines. At the entrance of the wind farm correlations should present a closer behaviour to the one observed for the LSWF.

In a second step, we have developed a model based on a truncated normal probability distribution function (TN-PDF) to provide a measure of the correlation between the incoming TKE and that measured at the turbine's rotor-disk ahead of time. By modelling the turbulent correlations, it is now possible to help decide what is the best upstream scanning distance to learn about the incoming turbulence, as a function of atmospheric stability and wind farm configuration. While not tested within this work, we further hypothesize that the TN-PDF parameters should be dependent on the local micro-meteorology and geographical characteristics. The model proposed includes four fitting parameters, two of them, μ and β, very important. The first one is indicative of when the maximum correlation coefficient is achieved, which is intimately related to the advection velocity. The second one, β, is an indicator of the vertical shift of the probability distribution, and hence an indicator of the effectiveness in predicting important turbulent events.

Finally, we note that the scanning distance should always be chosen the shortest possible in relation with the wind turbine reaction time. Best correlations are measured during unstable periods, which is very important because it is when the largest turbulent events happen. During stable periods, turbulence is weak and foreseeing incoming turbulence remains a challenge.

Acknowledgements

This research has been supported with the start-up funds provided by the Mechanical Engineering Department at University of Utah to Assistant Professor Marc Calaf. The support and resources from the Center for High Performance Computing at the University of Utah are gratefully acknowledged.

Appendix. Large eddy simulation formulation

In order to numerically simulate the flow throughout a diurnal cycle, the filtered Navier-Stokes equations (NS) with conservation of mass and an advection-diffusion equation for potential temperature are integrated in time. The atmospheric boundary layer (ABL) flow is considered incompressible and as a result of the high

Reynolds number (Re) the viscous terms are neglected. The NS equations are integrated in rotational form to ensure conservation of mass and energy for the inertial terms [38], hence they are written as,

$$\frac{\partial \tilde{u}_i}{\partial x_i} = 0, \tag{10a}$$

$$\frac{\partial \tilde{u}_i}{\partial t} + \tilde{u}_j\left(\frac{\partial \tilde{u}_i}{\partial x_j} - \frac{\partial \tilde{u}_j}{\partial x_i}\right) = -\frac{1}{\rho}\frac{\partial p^*}{\partial x_i} - \frac{\partial \tilde{\tau}_{ij}}{\partial x_j} + g\left(\frac{\tilde{\theta} - \langle\tilde{\theta}\rangle}{\theta_0}\right)\delta_{i3} + f(\tilde{u}_2 - v_G)\delta_{i1} - f(\tilde{u}_1 - u_G)\delta_{i2} + f_i, \tag{10b}$$

$$\frac{\partial \tilde{\theta}}{\partial t} + \tilde{u}_j\frac{\partial \tilde{\theta}}{\partial x_j} = -\frac{\partial \pi_j}{\partial x_j}. \tag{10c}$$

Index notation is used to specify rectangular Cartesian coordinates $i = 1, 2, 3 = x, y, z$, where Equation (10a) represents conservation of mass, Equation (10b) is the filtered NS equations. The same form of the filtered Navier-Stokes equations is used in (Moeng, [43]) with the addition of Equation (10c) for the filtered potential temperature ($\tilde{\theta}$), and hence the introduction of the buoyancy term in the right hand side of the NS equation. The buoyancy term is represented by the Boussinesq approximation [39], representing density fluctuations by relative temperature fluctuations, where θ_0 denoting the reference temperature. The $(\tilde{\cdot})$ denotes the LES filtering operation at the grid-size Δ, and the lateral brackets $(\langle\cdot\rangle)$ denote horizontal average in the $x-y$ planes. The flow is forced with a constant geostrophic wind equal to $u_G = 9m/s$ in the streamwise direction and $v_G = -3m/s$ in the spanwise direction. To represent a realistic diurnal cycle, both, the geostrophic wind and the surface temperature are obtained from a selected period of the Cooperative Atmosphere-Surface Exchange Study (CASES-99) that took place in Len (Kansas) from October first to 31st of 1999 (see Fig. 1). The dataset of interest for the present study begins at 2100 local time (LT) on the 22nd of October and extends up to a total of 48 h during which different atmospheric stability conditions are of interest to the present study. The same data set have been used in several LES studies and it has been verified experimentally with the CASES-99 field data [20,21,23,40]. In the above NS equations f denotes the Coriolis frequency ($f = 8.87 \times 10^{-5}s^{-1}$) for a latitude of 37.6N and the Kronecker delta is denoted by δ_{ij} ($\delta_{ij} = 1$, if $i = j$, and 0 otherwise). The gravitational acceleration is set to $g = 9.81ms^{-1}$ and $\tilde{u}$ denotes the filtered velocity. The filtered shear stress is represented by τ_{ij} and its deviatoric part is modelled using the sub-grid Lagrangian Scale-dependent model of Bou-Zeid et al. [41]. For the potential temperature the sub-grid sensible heat flux π_j from Equation (10c) is modelled using the Lagrangian Scale-dependent for scalars of Calaf et al. [42]. The modified kinematic pressure term (p^*) includes the filtered pressure term and the trace of the SGS tensor $\left(\tilde{p}/\rho + \tilde{\tau}_{kk}/3 + \frac{1}{2}\tilde{u}_j\tilde{u}_j\right)$. Finally, the body forces resultant from the wind turbines are represented by a body force term denoted as f_i. The wind turbine model implemented in the LES simulations is the traditional actuator-disk with rotation (ADR, see Wu et al. [18]) with an additional dynamic yaw-alignment model first introduced by Sharma et al. [19]. Also, it should be noticed that in LES of atmospheric flows the viscous effects are neglected due to the very large Reynolds number. The integration of the equations in the horizontal directions (streamwise and spanwise) is performed using a pseudo-spectral approach and for the vertical direction it is used a second-order finite difference scheme, similar to Moeng [43] and Albertson et al. [44]. The pseudo-spectral approach implies a periodic boundary conditions, which results in a periodic domain. The 3/2-rule is uded for deliazing [45] and the time integration is performed using a second order Adam-Bashfort scheme. Also, the LES numerical code is fully parallelizated with the Message-Passing Interface (MPI) using the pipeline Thomas algorithm [46] to parallelize the pressure solver.

The LES numerical grid is represented by $256 \times 128 \times 384$ grid-points with a numerical resolution of $24.54 \times 24.54 \times 7.81m$. The code uses a staggered grid to impose a non-slip condition for the vertical velocity ($\tilde{w} = 0$) at the surface of the domain. At the first grid point it is imposed an equivalent shear stress (τ) for the horizontal velocities $\tilde{u}$ and $\tilde{v}$, streamwise and spanwise respectively. Also, it is imposed a null vertical flux and a null vertical shear stress. For the parametrization of the surface horizontal shear stress, it is used an adaptation of Monin-Obukhov's similarity theory [47], similar to [41,48,49],

$$\tau_{i,3}(x, y, z_1) = -\left[\frac{k\sqrt{\left(\widehat{\tilde{u}}_1^2 + \widehat{\tilde{u}}_2^2\right)}}{ln\left(z_1/z_0\right) + \psi_m(z_1/L)}\right]^2 n_i; \tag{11}$$

where z_1 indicates the height of the first grid point located at $\Delta_z/2$, where Δ_z is the grid size in the vertical direction equal to 7.81 m. Also it is at that height where the horizontal velocity components are computed and where the shear stress is applied. The imposed ground surface roughness imposed in this study is equal to $z_0 = 3{\cdot}10^{-5}z_i$ matching this from the CASES-99 experimental campaign and also used in Kumar et al. and Svensson et al. [20,23,40]. The initial inversion height is denoted by z_i and will be used as a normalization length-scale. Further, n_i is the unit vector, $n_i = \widehat{\tilde{u}}_i/\sqrt{\widehat{\tilde{u}}_1^2 + \widehat{\tilde{u}}_2^2}$ where i indicates any of the horizontal directions taking values of $i = 1, 2$. In addition to the parametrization of the horizontal shear stress at the surface, the vertical derivatives of the horizontal velocities are also parametrized at the first grid point (z_1) using Monin-Obukhov similarity theory [50],

$$\partial_3\tilde{u}_i(x, y, z_1) = \left(\frac{\sqrt{\tau}}{\kappa z}\right)n_i, \tag{12}$$

where $\tau = \sqrt{\tau_{1,3}^2 + \tau_{2,3}^2}$. A time-varying surface temperature is imposed (see Fig. 1a) from which the surface sensible heat flux imposed at the first staggered grid-point is computed using Monin-Obukhov's similarity theory,

$$H_s(x, y, z_1) = \frac{\kappa^2\left[\theta_s - \tilde{\theta}(x, y, z_1)\right]\left(\sqrt{\widehat{\tilde{u}}_1^2 + \widehat{\tilde{u}}_2^2}\right)}{\left[ln\left(\frac{z_1}{z_0}\right) + \psi_m(z/L)\right]\left[ln\left(\frac{z_1}{z_{0,h}}\right) + \psi_h(z/L)\right]}, \tag{13}$$

where $z_{0,h} = z_0/10$ represents the scalar surface roughness. Following Brutsaert's et al. [51] experimental data, this has been taken to be one tenth of the momentum surface roughness. To correct for the stability, it has been used the correction functions ($\psi(z/L)$) implemented by Brutsaert [52]. The stability correction functions were initially developed from experimental studies on statistically homogeneous surfaces without the presence of wind turbines, and such, it should be noticed that wind turbines might have an effect on the precise parametrization of the stability corrections. However, lack of new experimental data on this precise matter doesn't allow for a better numerical approach at the present time.

References

[1] G. Cortina, V. Sharma, M. Calaf, Investigation of the incoming wind vector for improved wind turbine yaw-adjustment under different atmospheric and wind farm conditions, Renew. Energy 101 (2017) 376–386.

[2] P.A. Fleming, A.K. Scholbrock, A. Jehu, S. Davoust, E. Osler, A.D. Wright, A. Clifton, Field-test results using a nacelle-mounted lidar for improving wind turbine power capture by reducing yaw misalignment, J. Phys. Conf. Ser. 524 (1) (2014) 012002.
[3] T. Mikkelsen, N. Angelou, K. Hansen, M. Sjöholm, M. Harris, C. Slinger, P. Hadley, R. Scullion, G. Ellis, G. Vives, A spinner-integrated wind lidar for enhanced wind turbine control (October), Wind Energy 16 (2013) 625–643.
[4] A. Scholbrock, P. Fleming, A. Wright, C. Slinger, J. Medley, M. Harris, Field Test Results from Lidar Measured Yaw Control for Improved Yaw Alignment with the NREL Controls Advanced Research Turbine Preprint, 2015, pp. 1–9.
[5] K.A. Kragh, M.H. Hansen, T. Mikkelsen, Improving yaw alignment using spinner based lidar, in: AIAA Aerospace Sciences Meeting Including the New Horizons Forum and Aerospace Exposition (January), 2011, pp. 1–13.
[6] D. Schlipf, S. Kapp, J. Anger, O. Bischoff, M. Hofsäß, A. Rettenmeier, M. Kühn, Prospects of optimization of energy production by lidar assisted control of wind turbines, in: EWEA 2011 Conference Proceedings, 2011, pp. 1–10, http://dx.doi.org/10.18419/opus-3916.
[7] J. Medley, W. Barker, M. Harris, M. Pitter, C. Slinger, T. Mikkelsen, M. Sjöholm, Evaluation of Wind Flow With a Nacelle-Mounted, Continuous Wave Wind Lidar, Ewea, 2014 (February).
[8] R. Wagner, M. Courtney, T.F. Pedersen, D.T.U.W. Energy, R. Campus, Power performance measured using a nacelle-mounted LiDAR, Dewi Mag. 43 (2013) 49–54.
[9] M. Harris, D. Bryce, A. Coffey, D. Smith, J. Birkemeyer, U. Knopf, Advance measurements of gusts by laser anemometry, Wind Eng. Industrial Aerodynamics 95 (2007) 1637–1647.
[10] D. Schlipf, S. Schuler, P. Grau, F. Allgöwer, M. Kühn, Look-ahead cyclic pitch control using LIDAR, in: Proc. Of the Science of Making Torque from Wind (TORQUE), 2010, pp. 1–7.
[11] F. Dunne, D. Schlipf, L.Y. Pao, N. Kelley, A.D. Wright, E. Simley, B. Jonkman, Comparison of two independent lidar-based pitch control designs, in: 50th AIAA Aerospace Sciences Meeting Including the New Horzons Forum and Aerospace Exposition, 2012, pp. 1–22.
[12] K.A. Kragh, M.H. Hansen, Load alleviation of wind turbines by yaw misalignment, Wind Energy 17 (2014) 971–982.
[13] P.M.O. Gebraad, J.W. van Wingerden, A control-oriented dynamic model for wakes in wind plants, J. Phys. Conf. Ser. 524 (2014) 012186.
[14] M. Churchfield, S. Fleming, P. Bulder, B. White, Wind turbine wake-redirection control at the Fishermen's atlantic city windfarm, in: Offshore Technology Conference, 04-07 May, Houston, Texas, USA (May), 2015, pp. 01–22.
[15] F. Dunne, L.Y. Pao, A.D. Wright, E. Simley, B. Jonkman, Adding Feedforward Blade Pitch Control for Load Mitigation in Wind Turbines: Non-causal Series Expansion, Preview Control, and Optimized FIR Filter Methods, American Institute of Aeronautics and Astronautics, 2011, pp. 1–17.
[16] E. Muljadi, C. Butterfield, Pitch-controlled Variable-speed Wind Turbine Generation, IEEE Transactions on Industry Applications, 2000, pp. 1–8.
[17] G.S. Poulos, W. Blumen, D.C. Fritts, J.K. Lundquist, J. Sun, S.P. Burns, C. Nappo, R. Banta, R. Newsom, J. Cuxart, E. Terradellas, B. Balsley, M. Jensen, CASES-99: A comprehensive investigation of the stable nocturnal boundary layer, Bulletin of the American Meteorological Society 83 (4) (2002) 555–581.
[18] Y. Wu, F. Porté-agel, Large-eddy simulation of wind-turbine wakes: evaluation of turbine parametrisations, Boundary Layer Meteorol. 138 (2011) 345–366.
[19] V. Sharma, M. Calaf, M. Lehning, M.B. Parlange, Time-adaptive wind turbine model for an les framework, Wind Energy 19 (5) (2016) 939–952.
[20] V. Kumar, J. Kleissl, C. Meneveau, M.B. Parlange, Large-eddy simulation of a diurnal cycle of the atmospheric boundary layer: atmospheric stability and scaling issues, Water Resour. Res. 42 (2006) 1–18.
[21] V. Sharma, M.B. Parlange, M. Calaf, Perturbations to the spatial and temporal characteristics of the diurnally-varying atmospheric boundary layer due to an extensive wind farm, Boundary Layer Meteorol. (2016) 128.
[22] Y.-T. Wu, F. Port-Agel, Atmospheric turbulence effects on wind-turbine wakes: an les study, Energies 5 (12) (2012) 5340.
[23] V. Kumar, G. Svensson, A.A.M. Holtslag, C. Meneveau, M.B. Parlange, Impact of surface flux formulations and geostrophic forcing on large-eddy simulations of diurnal atmospheric boundary layer flow, J. Appl. Meteorology Climatol. 49 (2009) 1496–1516.
[24] S.V. Crowder, S.A. Wiel, Exponentially Weighted Moving Average (EWMA) Control Chart, John Wiley & Sons, Ltd, 2014.
[25] Ü. Rannik, T. Vesala, Autoregressive filtering versus linear detrending in estimation of fluxes by the eddy covariance method, Boundary Layer Meteorol. 91 (2) (1999) 259–280.
[26] J. Moncrieff, R. Clement, J. Finnigan, T. Meyers, Averaging, Detrending, and Filtering of Eddy Covariance Time Series, Springer, Netherlands, Dordrecht, 2005, pp. 7–31.
[27] D. Vickers, L. Mahrt, The cospectral gap and turbulent flux calculations, J. Atmos. Ocean. Technol. 20 (5) (2003) 660–672.
[28] R. Sozzi, M. Favaron, Sonic anemometry and thermometry: theoretical basis and data processing software, Environ. Softw. 11 (1997) 259–270.
[29] M. Metzger, H. Holmes, Time scales in the unstable atmospheric surface layer, Boundary Layer Meteorol. 126 (1) (2008) 29–50.
[30] K. Babić, Z.B. Klaić, Ž. Večenaj, Determining a turbulence averaging time scale by Fourier analysis for the nocturnal boundary layer, Geofizika 29 (2012) 35–51.
[31] M. Abkar, A. Sharifi, F. Porté-Agel, Large-eddy simulation of the diurnal variation of wake flows in a finite-size wind farm, J. Phys. Conf. Ser. 625 (2015) 012031.
[32] A.C. Fitch, J.K. Lundquist, J.B. Olson, Mesoscale influences of wind farms throughout a diurnal cycle, Mon. Weather Rev. 141 (2013) 2173–2198.
[33] C.W. Higgins, M. Froidevaux, V. Simeonov, N. Vercauteren, C. Barry, M.B. Parlange, The effect of scale on the applicability of taylor's frozen turbulence hypothesis in the atmospheric boundary layer, Boundary Layer Meteorol. 143 (2) (2012) 379–391.
[34] E. Simley, N. Angelou, T. Mikkelsen, M. Sjöholm, J. Mann, L.Y. Pao, Characterization of wind velocities in the upstream induction zone of a wind turbine using scanning continuous-wave lidars, J. Renew. Sustain. Energy 8 (1) (2016) 013301.
[35] R.K. Newsom, R.M. Banta, Shear-flow instability in the stable nocturnal boundary layer as observed by doppler lidar during CASES-99, J. Atmos. Sci. 60 (1) (2003) 16–33.
[36] C.D. Markfort, W. Zhang, F. Porté-Agel, A simple model for average kinetic energy flux within large wind turbine arrays, in: Presented at the 22nd Symposium on Boundary Layers and Turbulence, Salt Lake City, UT, 2016.
[37] D. Allaerts, J. Meyers, Internal boundary layer growth over large wind farms under conventionally neutral conditions, in: Presented at the 22nd Symposium on Boundary Layers and Turbulence, Salt Lake City, UT, 2016.
[38] S.A. Orszag, Y.-H. Pao, Numerical computation of turbulent shear flows, Adv. Geophys. 18 (1975) 225–236, http://dx.doi.org/10.1016/S0065-2687(08)60463-X.
[39] R. Stull, An Introduction to Boundary Layer Meteorology, Atmospheric Science Library, Springer, 1988.
[40] G. Svensson, A.A.M. Holtslag, V. Kumar, T. Mauritsen, G.J. Steeneveld, W.M. Angevine, E. Bazile, A. Beljaars, E.I.F. de Bruijn, A. Cheng, L. Conangla, J. Cuxart, M. Ek, M.J. Falk, F. Freedman, H. Kitagawa, V.E. Larson, A. Lock, J. Mailhot, V. Masson, S. Park, J. Pleim, S. Söderberg, W. Weng, M. Zampieri, Evaluation of the diurnal cycle in the atmospheric boundary layer over land as represented by a variety of single-column models: the second gabls experiment, Boundary Layer Meteorol. 140 (2) (2011) 177–206.
[41] E. Bou-Zeid, C. Meneveau, M. Parlange, A scale-dependent Lagrangian dynamic model for large eddy simulation of complex turbulent flows, Phys. Fluids 17 (2) (2005) 1–18.
[42] M. Calaf, M. B. Parlange, C. Meneveau, Large eddy simulation study of scalar transport in fully developed wind-turbine array boundary layers, Phys. Fluids 23(12).
[43] C.-h. Moeng, A large-eddy-simulation model for the study of planetary boundary-layer turbulence, J. Atmos. Sci. 41 (13) (1984) 2052–2062.
[44] J.D. Albertson, M.B. Parlange, Natural integration of scalar fluxes from complex terrain, Adv. Water Resour. 23 (3) (1999) 239–252.
[45] C. Canuto, M.Y. Hussaini, A. Quarteroni, T.A. Zang, Spectral Methods in Fluid Dynamics, Springer-Verlag, Berlin, 1988.
[46] A. Povitsky, P.J. Morris, A higher-order compact method in space and time based on parallel implementation of the Thomas algorithm, J. Comput. Phys. 161 (1) (2000) 182–203.
[47] A.S. Monin, A.M. Obukhov, Basic laws of turbulent mixing in the surface layer of the atmosphere, Tr. Akad. Nauk. SSSR Geofiz. Inst. Engl. Transl. by John Mill. 1959 24 (151) (1954) 163–187.
[48] M.B.B.W. Parlange, Regional shear stress of broken forest from radiosonde wind profiles in the unstable surface layer, Boundary Layer Meteorol. 64 (4) (1993) 355–368.
[49] M. Hultmark, M. Calaf, M.B. Parlange, A new wall shear stress model for atmospheric boundary layer simulations, J. Atmos. Sci. 70 (11) (2013) 3460–3470.
[50] W. Brutsaert, M.B. Parlange, The unstable surface layer above forest: regional evaporation and heat flux, Water Resour. Res. 28 (12) (1992) 3129–3134.
[51] W. Brutsaert, J. Gash, M. Parlange, et al., Neutral humidity profiles in the boundary layer and regional evaporation from sparse pine forest, Ann. Geophys. 7 (1989) 623–630.
[52] W. Brutsaert, Hydrology: an Introduction, Cambridge University Press, 2005.

CHAPTER 4

DISTRIBUTION OF MEAN KINETIC ENERGY AROUND AN ISOLATED WIND TURBINE AND A CHARACTERISTIC WIND TURBINE OF A VERY LARGE WIND FARM

Physical Review Fluids (2016) 1, 074402. Distribution of mean kinetic energy around an isolated wind turbine and a characteristic wind turbine of a very large wind farm. G. Cortina, M. Calaf, R. B. Cal.

PHYSICAL REVIEW FLUIDS **1**, 074402 (2016)

Distribution of mean kinetic energy around an isolated wind turbine and a characteristic wind turbine of a very large wind farm

Gerard Cortina* and Marc Calaf†
Department of Mechanical Engineering, University of Utah, Salt Lake City, Utah 84112, USA

Raúl Bayoán Cal‡
Department of Mechanical Engineering, Portland State University, Portland, Oregon 97207, USA
(Received 9 March 2016; published 9 November 2016)

An isolated wind turbine and a very large wind farm are introduced into large-eddy simulations of an atmospheric boundary layer. The atmospheric flow is forced with a constant geostrophic wind and a time-varying surface temperature extracted from a selected period of the CASES-99 field experiment. A control volume approach is used to directly compare the transfer of mean kinetic energy around a characteristic wind turbine throughout a diurnal cycle considering both scenarios. For the very large wind farm case, results illustrate that the recovery of mean kinetic energy around a wind turbine is dominated by the vertical flux, regardless of atmospheric stratification. Contrarily, for an isolated wind turbine, the recovery is dependent on the background atmospheric stratification and it is produced by a combination of advection, vertical flux, and pressure redistribution. The analysis also illustrates that during the unstable stratification periods vertical entrainment of mean kinetic energy dominates, whereas during the stable regime horizontal entrainment is predominant. Finally, it is observed that in both scenarios, the single wind turbine and the large wind farm cases, turbulent mixing is driven by the background convective stratification during the unstable period and by the effect of the wind turbine during the stable regime.

DOI: 10.1103/PhysRevFluids.1.074402

I. INTRODUCTION

Wind energy has stood as a prominent element of the mix of renewable energies, with a remarkable growth of 23% over the past decade [1]. For wind energy to be profitable large arrays of wind turbines, so-called wind farms, must be built. However, the capacity for the atmospheric turbulent flow to immediately recover past a succession of wind turbines is limited, inducing power losses and enhanced structural fatigue due to turbine to turbine proximity [2–4]. In a very large wind farm, a fully developed turbulent flow develops, in which the statistical properties of the flow do not change within the horizontal directions, thus relevant changes mostly occur in the vertical direction. Within this region, the so-called wind turbine array boundary layer, the recovery of the successive turbine-generated wakes is only a result of vertical entrainment of mean kinetic energy (MKE) as shown by Lu and Porté-Agel [5], Yang *et al.* [6], VerHulst and Meneveau [7], and Abkar and Porté-Agel [8], which is a function of the wind farm arrangement [9]. This mechanism determines the overall efficiency of the farm as numerically shown by VerHulst and Meneveau [10] for a pressure-driven flow without thermal stratification, by Calaf *et al.* [11] for a neutrally stratified atmospheric flow, and experimentally by Cal *et al.* [12]. These large wind farms alter the local atmospheric flow with changes in the surface momentum and surface heat fluxes [13], as well as readjusting the Coriolis force balance [14]. Overall, wind farms increase the turbulent mixing with

*gerard.cortina@utah.edu; http://wet.mech.utah.edu
†marc.calaf@utah.edu; http://wet.mech.utah.edu
‡rcal@pdx.edu

a reduction of momentum entrainment near the surface and a large increase near the top tip of the rotor blades. These flow alterations change the heat fluxes (sensible and latent) and introduce small perturbations on the surface and air flow temperature [14–17].

A control volume approach to extend the current understanding of the redistribution of MKE and recovery process around a single wind turbine and a characteristic wind turbine of a very large wind farm has been performed during a standard diurnal cycle. Results will illustrate the differences in the redistribution of MKE according to the background atmospheric stratification (stable, unstable, and neutral), as well as the relative importance of terms contributing the MKE budget (advection, work produced by the mean pressure field gradient, MKE flux, dissipation, gravitational acceleration of vertical motions, and Coriolis forcing).

In Sec. II the control volume framework used to develop the MKE budget is introduced. Section III presents the study cases considered and Sec. IV contains the concept of the wind turbine box. Section V presents the results for the aforementioned cases, illustrating the wind turbine box approach. Finally, conclusions are outlined in Sec. VI.

II. CONTROL VOLUME ANALYSIS OF THE MEAN KINETIC ENERGY

The mean kinetic energy equation is obtained by taking the product of the mean velocity $\overline{U}_i$ and the momentum equation

$$\overline{U}_j \frac{\partial \overline{U}_i}{\partial x_j} = -\frac{1}{\rho}\frac{\partial \overline{P}}{\partial x_i} - \frac{\partial \overline{u_i' u_j'}}{\partial x_j} + \nu \frac{\partial^2 \overline{U}_i}{\partial x_j^2} + \overline{B_i} - \overline{f}_i^{\mathrm{WT}} + f_c \epsilon_{ij3} \overline{U}_j, \tag{1}$$

where the prime denotes the fluctuations and the overbar a time-averaged quantity. The mean pressure is given by $\overline{P}$ and $\overline{f}_i^{\mathrm{WT}}$ represents the force imparted on the flow by the wind turbines. The thermal buoyant forcing is represented by $\overline{B_i} = \beta g(T - T_{\mathrm{ref}})\delta_{i3}$, where β is the coefficient of thermal expansion, g is gravity, T is the mean temperature, and T_{ref} is the reference temperature. Respectively, both air flow properties, density ρ and kinematic viscosity ν, are treated as constants. The Coriolis parameter is denoted by f_c and ϵ_{ij3} is the alternating unit tensor ($\epsilon_{ij3} = 0$ if $i = j$ and ± 1 otherwise). Omission of the time dependence of the velocity field is also noted ($\partial \overline{U}_i / \partial t = 0$). After carrying out the operation, the transport equation for the mean kinetic energy $K = \frac{1}{2}\overline{U}_i^2 = \frac{1}{2}(\overline{U}^2 + \overline{V}^2 + \overline{W}^2)$ ($\overline{U}$, $\overline{V}$, and $\overline{W}$ being the streamwise, lateral, and vertical mean velocities, respectively) is obtained as

$$\begin{aligned}\overline{U}_j \frac{\partial K}{\partial x_j} =& -\frac{\partial}{\partial x_j}\left(\frac{1}{\rho}\overline{P}\,\overline{U}_i \delta_{ij} + \frac{1}{2}\overline{u_i' u_j'}\,\overline{U}_i - 2\nu \overline{S}_{ij}\overline{U}_i\right) \\ & - \overline{u_i' u_j'}\frac{\partial \overline{U}_i}{\partial x_j} - 2\nu \overline{S}_{ij}\overline{S}_{ij} + \overline{U}_i \overline{B} - \overline{U}_i \overline{f}_i^{\mathrm{WT}} + f_c \epsilon_{ij3}\overline{U}_i \overline{U}_j,\end{aligned} \tag{2}$$

where $\overline{S}_{ij} = \frac{1}{2}(\frac{\partial \overline{U}_i}{\partial x_j} + \frac{\partial \overline{U}_j}{\partial x_i})$ is the mean strain rate tensor. From left to right, the terms in Eq. (2) are the advection of mean kinetic energy, mechanical work produced by gradients in the mean pressure field, two flux terms, i.e., mean kinetic energy by turbulence and viscous dissipation, production of turbulence kinetic energy, mean viscous dissipation, mean kinetic energy production or destruction by buoyancy forces, power extracted by the wind turbine, and the effect due to Coriolis force.

In marking a control volume (CV) around a turbine, a volume integral of the transport equation (2) is taken as shown in Fig. 1. In the CV of Fig. 1, the surfaces normal to the longitudinal direction, acting as inflow and outflow, are denoted by S_1 and S_2, lateral surfaces by S_3 and S_4, and horizontal

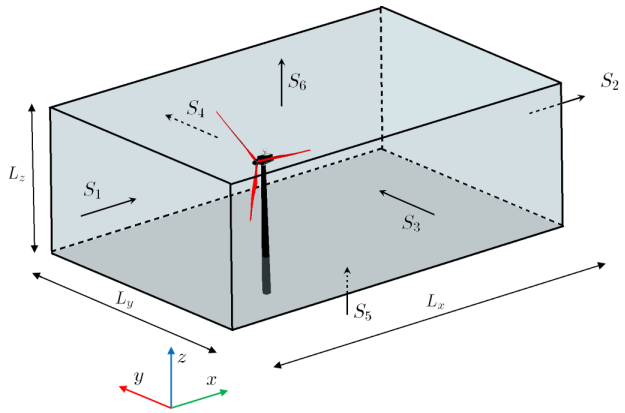

FIG. 1. Rectangular CV around the wind turbine used for an extended momentum analysis. The coordinate system denoted by x,y,z is the referent axis for the CV. The size of the CV is denoted by L_x,L_y,L_z, which represent the streamwise, spanwise, and vertical dimensions, respectively. The CV surfaces are denoted by S_i, where i indicates any of the CV surfaces (from 1 to 6).

bottom and top surfaces by S_5 and S_6. Hence, the volume integral of Eq. (2) reads

$$\overbrace{\iiint_{\forall} \overline{U}_j \frac{\partial K}{\partial x_j} d\forall}^{A_1} = -\overbrace{\iiint_{\forall} \frac{\partial}{\partial x_j}\left(\frac{1}{\rho}\overline{P}\,\overline{U}_i\delta_{ij} + \frac{1}{2}\overline{u_i'u_j'}\,\overline{U}_i - 2\nu\overline{S}_{ij}\overline{U}_i\right) d\forall}^{A_2}$$
$$- \underbrace{\iiint_{\forall} \overline{u_i'u_j'}\frac{\partial \overline{U}_i}{\partial x_j} d\forall}_{A_3} - \underbrace{\iiint_{\forall} 2\nu\overline{S}_{ij}\overline{S}_{ij} d\forall}_{A_4} + \underbrace{\iiint_{\forall} \overline{U}_i \overline{B} d\forall}_{A_5}$$
$$- \underbrace{\iiint_{\forall} \overline{U}_i\,\overline{f}_i^{\mathrm{WT}} d\forall}_{A_6} + \underbrace{\iiint_{\forall} f_c \epsilon_{ij3}\overline{U}_i\overline{U}_j d\forall}_{A_7}, \tag{3}$$

where the triple integral notation stresses that $d\forall$ is a closed volume.

To simplify the discussion, terms are labeled as A_n, where n runs from 1 to 7 as shown in the overbrackets and underbrackets in Eq. (3). Sequentially, these constitute the inertial terms A_1, the transport or flux terms denoted by A_2, production of turbulence kinetic energy A_3, and the mean viscous dissipation A_4. Finally, three-body force terms encompassing the buoyancy, the power extracted by the turbine, and the Coriolis effect, respectively, as A_5, A_6 and A_7, are also represented in Eq. (3). Introducing the divergence theorem, the volume integral of the advection of mean kinetic energy on the left-hand side is rewritten as a surface integral

$$A_1 = \iint_S (\overline{U}_i K)\hat{n}_i dS, \tag{4}$$

where $\hat{n}_i$ is the unit vector normal to the surface S of the CV. A similar treatment is applied to the volume integral of the transport terms of mean kinetic energy on the right-hand side

$$A_2 = \iint_S \left(\frac{1}{\rho}\overline{P}\,\overline{U}_i\delta_{ij} + \frac{1}{2}\overline{u_i'u_j'}\overline{U}_i - 2\nu\overline{S}_{ij}\overline{U}_i\right)\hat{n}_j dS. \tag{5}$$

Because the components of velocity tangent to the surface do not contribute to the flux across the control surface, since in such a case $\vec{u}\cdot\vec{n} = 0$, the surface integral of mean kinetic energy advection

TABLE I. Study cases for the LES numerical simulations.

Study case	ABL stratification	No. of turbines	$s_x \times s_y$
VLWF	unstable	48	$8D \times 5D$
VLWF	neutral	48	$8D \times 5D$
VLWF	stable	48	$8D \times 5D$
LSWF	unstable	1	$63D \times 31D$
LSWF	neutral	1	$63D \times 31D$
LSWF	stable	1	$63D \times 31D$

simplifies to

$$A_1 = -\iint_{S_1} \overline{U} K dS_1 + \iint_{S_2} \overline{U} K dS_2 - \iint_{S_3} \overline{V} K dS_3 + \iint_{S_4} \overline{V} K dS_4 - \iint_{S_5} \overline{W} K dS_5 + \iint_{S_6} \overline{W} K dS_6 \tag{6}$$

and surfaces are visualized in Fig. 1. Moreover, evaluating the various components within terms A_3 through A_7, the volume integral is considered. In expanding the term A_3, for example, the volume is composed of the differentials in the three directions x, y, and z and the corresponding stress term results

$$A_3 = \iiint_V \left(\overline{u'u'}\frac{\partial \overline{U}}{\partial x} + \overline{u'v'}\frac{\partial \overline{U}}{\partial y} + \overline{u'w'}\frac{\partial \overline{U}}{\partial z} + \overline{v'u'}\frac{\partial \overline{V}}{\partial x} + \overline{v'v'}\frac{\partial \overline{V}}{\partial y} + \overline{v'w'}\frac{\partial \overline{V}}{\partial z} + \overline{w'u'}\frac{\partial \overline{W}}{\partial x} + \overline{w'v'}\frac{\partial \overline{W}}{\partial y} + \overline{w'w'}\frac{\partial \overline{W}}{\partial z} \right) dx\, dy\, dz. \tag{7}$$

Therefore, it is understood that similarly it is obtained for the viscous dissipation, buoyancy, power extracted by the wind turbines, and the Coriolis terms in Eq. (3). Note that terms developed here correspond to the most general form of the MKE budget in a CV. These are correspondingly adapted to match the large-eddy simulations (see Sec. V A), which consist of a resolved and a subgrid stress contribution and neglect the viscous effects as a result of the high Reynolds number characteristic of atmospheric flows.

III. STUDY CASES

To develop this study, a suite of six large-eddy simulation (LES) cases are performed: three with a very large wind farm (VLWF) and three with a single wind turbine or largely spaced wind farm (LSWF). Table I summarizes the study cases. For both the LSWF and VLWF, a simulation consisting of a complete diurnal cycle (total of 24 h in physical time) is developed obtaining consecutive periods with stable (nighttime) and unstable (daytime) atmospheric stratification. The diurnal cycle is forced using a height-independent and time-constant geostrophic wind together with a time-varying surface temperature. The geostrophic wind $(u_G, v_G) = (9, -3)$ ms^{-1} and the surface temperature [see Fig. 2(a)] are extracted from the CASES-99 (Cooperative Atmosphere-Surface Exchange Study 1999) [18] field experiment between October 22 and 24 of 1999 and validated using results from Kumar *et al.* [19,20], Svensson *et al.* [21], and Basu *et al.* [22] as well as experimental data from the CASES-99 data set. Details on the LES framework can be found in previous works by Sharma *et al.* [23] and Cortina *et al.* [24]. The time period used to force the diurnal cycle has been previously used in studies of wind farms within a realistic atmospheric boundary layer diurnal cycle by Fitch *et al.* [25] and Sharma *et al.* [23] and is adopted here as well. Additionally, two independent cases forced with the same geostrophic forcing but with a fixed surface temperature and a well-mixed temperature profile are considered to simulate the case of a neutrally stratified atmospheric boundary layer (ABL) flow.

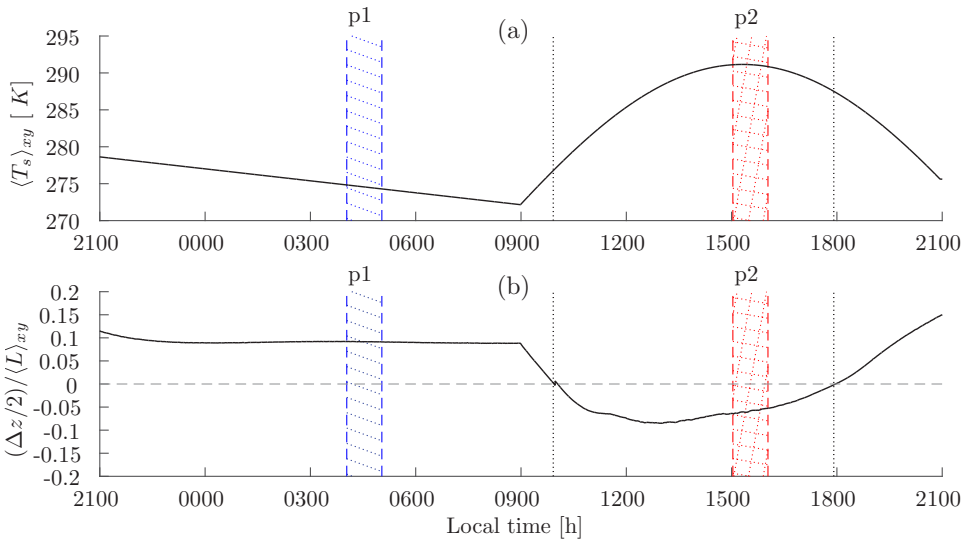

FIG. 2. (a) Horizontally averaged and time-dependent imposed temperature at the surface of the domain $\langle T_s \rangle_{xy}[K]$. (b) Normalized stability parameter $(\Delta z/2)/\langle L \rangle_{xy}$, where $\Delta z/2$ is the height of the first grid point and L is the Monin-Obukhov length as a function of time. One-hour periods marked with a 45° dotted line ($p1$), in blue, and squared dotted line ($p2$), in red, delineate time periods in which mean kinetic energy budgets and representative statistics are computed. Precisely, period $p1$ constitutes the time between 0400 and 0500 h local time (LT) and $p2$ denotes the time between 1500 and 1600 h of LT.

The time evolution of the surface temperature used to force the flow through a diurnal cycle is represented in Fig. 2(a) and the corresponding surface stability parameter z_1/L is shown in Fig. 2(b), where $z_1 = \Delta_z/2$ and Δ_z represents the vertical grid spacing. While the atmospheric flow through a diurnal cycle is intrinsically nonstationary, mean statistics over 1-h periods remain fairly unchanged. Here results for the 1-h periods between 0400 and 0500 h ($p1$) and between 1500 and 1600 h ($p2$) are presented, representative of a stable and an unstable atmospheric stratification, respectively. The same analysis is applied on other 1-h time periods through the different stable and unstable regimes, obtaining similar convergence in the statistics. A similar 1-h period is also analyzed for the neutrally stratified flow. For both cases, the LSWF and VLWF, the numerical domain is set to $(2\pi \times \pi \times 3)z_i$, where z_i is the initial height of the boundary layer, with $z_i = 1000$ m. In order to keep a high numerical resolution, the computational domain is discretized with a numerical grid of $256 \times 128 \times 384$ points, providing uniform grid resolutions of $\Delta_x = \Delta_y = 24.5$ m and $\Delta_z = 7.8$ m. The simulations are initialized with the velocity and temperature vertical profiles extracted from the CASES-99 field experiment, corresponding to a height-independent geostrophic wind and a well-mixed temperature profile matching the initial surface temperature of 278.6 K, with an inversion layer spanning from z_i to the top of the domain $3z_i$.

The VLWF configuration consists of eight rows with six wind turbines per row, using the traditional spacings of $\sim 8D$ and $\sim 5D$ (where D refers to the rotor diameter of the turbine, here taken equal to 100 m) in the streamwise and spanwise directions, respectively, as observed in Fig. 3(a). Because of the periodic boundary conditions, this configuration results in a practical sense equivalent to an infinite wind farm. On the other hand, the LSWF configuration, represented in Fig. 3(b), consists of a single wind turbine installed in the middle of the domain, and hence it is understood as a single isolated wind turbine, or as a result of the periodic boundary conditions, as a largely spaced wind farm, with wind turbine spacings of $\sim 63D$ and $\sim 31D$ in the streamwise and spanwise directions, respectively. In both configurations, the algorithm of Sharma *et al.* [26] is used

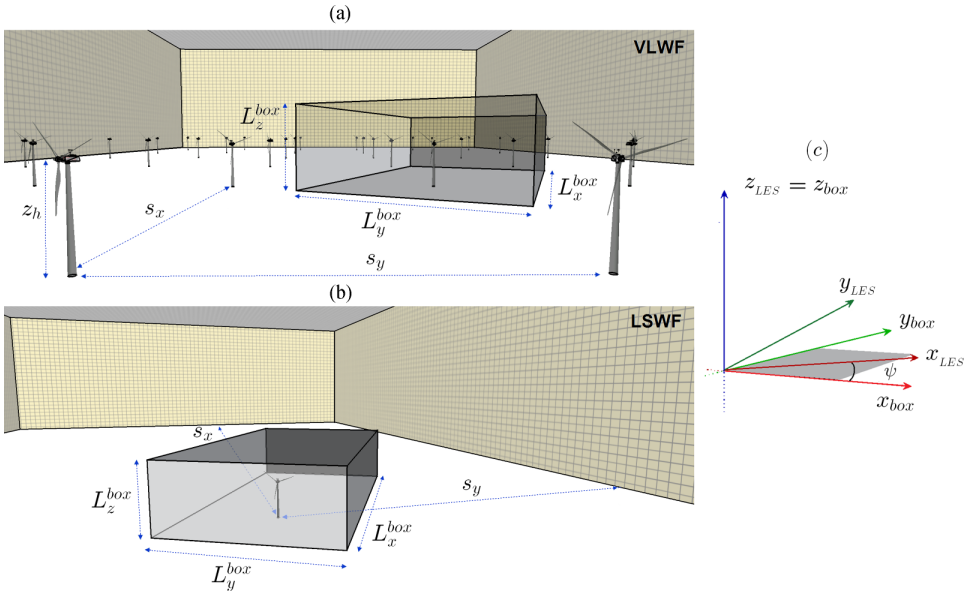

FIG. 3. (a) The VLWF case, (b) the LSWF case, and (c) graphical representation of the rotation between the LES domain coordinate frame and the wind turbine box.

to model the wind turbines, using an upstream scanning distance of $D/2$ to learn from the incoming wind vector and timely readjust the yaw angle of the turbines every 10 min (see [24]).

Differences in transport and recovery of MKE around an isolated wind turbine and a characteristic wind turbine within a wind farm are evaluated herein. To demonstrate the selected study periods, Figure 4 presents the time evolution of 10-min-averaged and horizontally averaged (between the top tip and bottom tip of the rotor) MKE for both cases, the VLWF (dashed line) and the LSWF (solid line), throughout the diurnal cycle. First, it should be noted that while the LES numerical simulation is exactly the same for both wind farms scenarios, a large difference in MKE is observed between them. During the stable stratified period (i.e., from 0000 to 0900 h), there exists ∼4 times more

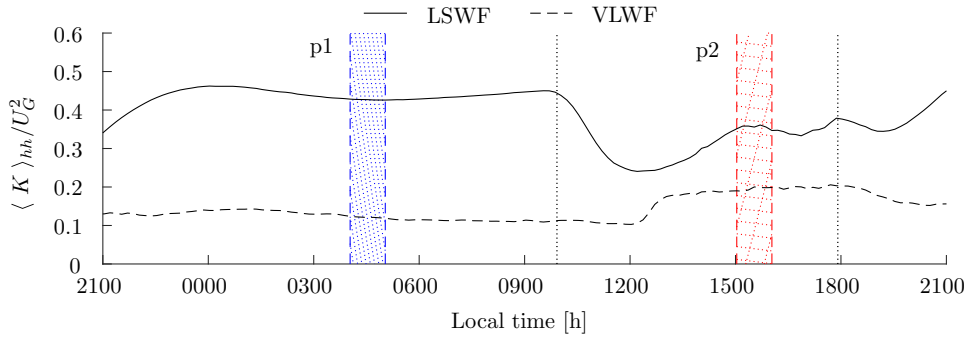

FIG. 4. Mean kinetic energy represented every 10 min and averaged over the volume capturing the wind turbine rotor disk (from $z_h - D/2$ to $z_h + D/2$, where $z_h = 100$ m is the hub height and D is the wind turbine diameter) normalized by the square of the geostrophic wind U_G. The MKE is represented for the LSWF and VLWF cases during the diurnal cycle. Correspondingly, the 45° dotted line region ($p1$), in blue, and the squared dotted region ($p2$), in red, identify the 1-h stable and unstable stratification periods.

energy in the LSWF than in the VLWF case. This is the result of the increased MKE absorption of the large wind farm. Further, the stable-LSWF period is characterized by a nocturnal low level jet (LLJ) intersecting the wind turbines rotor and hence accounted for in this MKE representation, while for the VLWF case the low level jet is shifted above the wind turbines hub layer (see [14,23,25,27]). This effect results in large energy differences between both stable conditions. On the other hand, the unstable periods are dominated by enhanced atmospheric mixing and hence the difference in available energy between the LSWF and the VLWF case is reduced. The unstable-LSWF regime (i.e., from 1300 to 1800 h) on average has 1.5 times more energy than the unstable-VLWF case. These differences in available energy will be further illustrated later within the analysis of MKE redistribution. Also, one should note the trend of MKE as a function of time. While for the LSWF more energy is available during the stable period ($K_{\text{unstable}} = 1.2K_{\text{stable}}$), for the VLWF the opposite results, with the unstable or convective regime being the one that presents the largest MKE available ($K_{\text{unstable}} = 0.5K_{\text{stable}}$). Further, it is worth noting that the MKE for the VLWF case presents a change of 30% within hours 1200 to 1400 and then reaches a quasistationary state. For the LSWF, there is an apparent constant change in the MKE ($\sim$5%/h) from 1200 to 1500 h.

IV. WIND TURBINE BOX

To directly compare the flow around a single wind turbine and the flow around a wind turbine installed within a very large wind farm, a dynamically time-realigned CV surrounding each wind turbine, from here on referred to as a wind turbine box, is developed. The wind turbine box consists of a reduced domain of adjustable size, with the box-local streamwise direction timely aligned perpendicular to the actual rotor disk [see Figs. 5(a)–5(d)]. Within this work, the box of the turbine is selected with a dimension of $(L_x^{\text{box}}, L_y^{\text{box}}, L_z^{\text{box}}) = (9D, 5D, 7D/4)$ and centered around the rotor. Precisely, the box extends between a distance of $2D$ upstream and $7D$ downstream of the disk in the streamwise direction and $2.5D$ left and right of the hub of the rotor in the cross-streamwise direction, respectively. In the vertical direction, the box is selected to extend a vertical distance between $z_h - 3D/4$ and $z_h + D$. The box size has been selected of equal size for both study cases (the VLWF and LSWF) to be able to compare statistics. Therefore, given the limited spacing in the VLWF case, the box is selected to capture the maximum wake region without including the effect of the following wind turbine. It is then possible to evaluate terms as developed in Sec. II from the standpoint of the wind turbine box as the CV is closely associated with the analysis.

The wind turbine box is designed such that its corresponding streamwise axis x_{box} is timely perpendicular to the rotor disk and hence aligned with the mean wind vector. The flow variables are initially computed within the base LES coordinate frame $(x_{\text{LES}}, y_{\text{LES}}, z_{\text{LES}})$ and then transformed into the new box coordinate frame $(x_{\text{box}}, y_{\text{box}}, z_{\text{box}})$. The mapping transformation consists of a rotation around the vertical axis $z_{\text{LES}} = z_{\text{box}}$, which remains frame invariant and it is represented by a rotation matrix, denoted by $\mathbf{R}$ with a rotation angle denoted by ψ, which represents the horizontal angle between the LES domain and box coordinate system [see Fig. 3(c)]. Note that, through the resultant coordinate transformation, the LES mean flow direction becomes the box local streamwise direction ($\vec{u}_{\text{box}} = \mathbf{R}\,\vec{u}_{\text{LES}}$). Similarly, the Reynolds stress tensor components are transformed using the corresponding matrix transformation $\tau_{\text{box}} = \mathbf{R}\,\tau_{\text{LES}}\mathbf{R}^{\text{T}}$, where $\mathbf{R}^{\text{T}}$ indicates the transpose of the rotation matrix. Figures 3(a) and 3(b) illustrate the structure of the wind turbine box within the LES domain for the VLWF and LSWF cases, respectively, and the schematics of the frame rotation $(x_{\text{LES}}, y_{\text{LES}}, z_{\text{LES}}) \rightarrow (x_{\text{box}}, y_{\text{box}}, z_{\text{box}})$ is represented in Fig. 3(c).

V. RESULTS

A. Flow around a characteristic wind turbine

Figures 5(a)–5(d) represent 1-h-averaged velocity field for both cases, the VLWF and LSWF, and for both stratification periods (stable and unstable) at hub height. In Fig. 5(a) the unstable regime causes the turbine wakes to be shorter and less organized due to the increased mixing characteristic

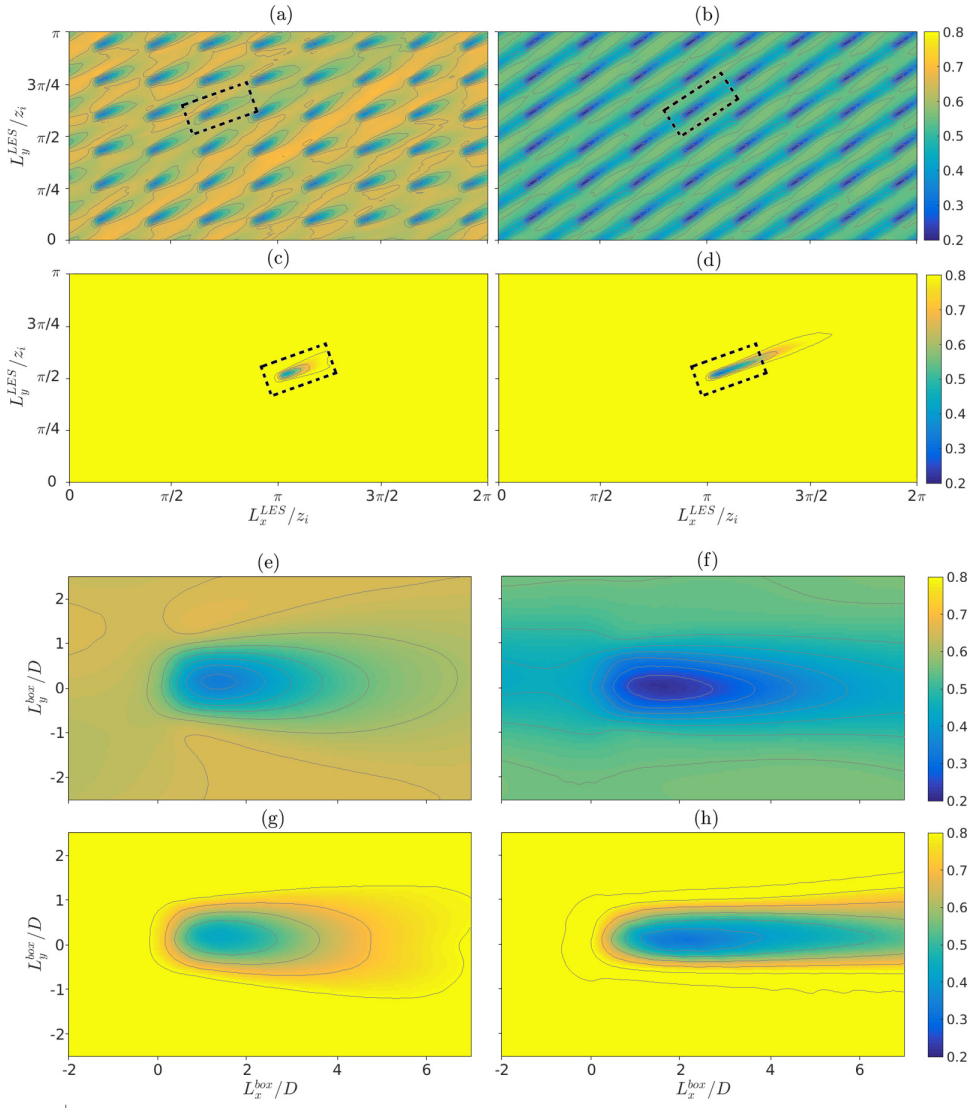

FIG. 5. The LES domain horizontal slices of 1-h-averaged, normalized velocity magnitude fields at hub height for two characteristic periods of the VLWF and LSWF simulations: (a) unstable VLWF, (b) stable VLWF, (c) unstable LSWF, and (d) stable LSWF. Also shown are the horizontal slices of 1-h averaged, normalized velocity magnitude at hub height within the wind turbine box reference frame: (e) unstable VLWF, (f) stable VLWF, (g) unstable LSWF, and (h) stable LSWF. The dashed line surrounding the wind turbine in (a)–(d) represents the wind turbine box.

of unstable regimes; this is especially the case in the VLWF. In contrast, wakes visibly persist over longer distances and overall are more organized during the stable regime [see Fig. 5(b)], as a result of the attenuated mixing due to turbulence. While the flow for the neutral stratification is not represented here, the flow shows a signature similar to that in the unstable regime, where the

turbine wakes expansion results in a radial shape, symmetrically in both directions (x-y plane), also reported by Abkar and Porté-Agel [9]. Rather than considering a wind farm, Figs. 5(c) and 5(d) highlight a single turbine under unstable and stable regimes, respectively. Wake features are similar to those in the wind farm, although these are exaggerated due to the lack of turbine-turbine wake interaction. In these cases, the difference in the expansion of the wake is in its length. Figures 5(c) and 5(d) illustrate that the length of the wake during the stable regime is twice as large as for the unstable period. Also, it should be noted that the yaw alignment has an effect on the wake length and persistence. During the 1-h stable period ($p1$) the standard deviation of the wind angle is $\sim 1^{\circ}$, while for the unstable period the standard deviation is $\sim 5^{\circ}$ (see [24]). This results in a more dynamic wind turbine force acting on the flow in time and space during the unstable regime.

Using the CV approach previously described, a comparison between the flow around a single wind turbine (LSWF) and a characteristic wind turbine within a VLWF is sought. This last one is obtained by averaging the flow of the 48-turbine boxes (one per wind turbine of the LES domain). Figure 5 presents a 1-h-averaged streamwise velocity field at hub height (using the wind turbine box) for the unstable [Figs. 5(a), 5(c), 5(e), and 5(g)] and stable [Figs. 5(b), 5(d), 5(f), and 5(h)] regimes. From this representation, the flow around both wind turbine scenarios [the VLWF represented in Figs. 5(e) and 5(f) and the LSWF represented in Figs. 5(g) and 5(h)] is very distinct between atmospheric stability conditions. From Figs. 5(e)–5(h) it can be observed that both types of turbines present different wake geometries. Flow features show changes in both streamwise and cross-streamwise directions. Figure 5(e) is the characteristic unstable wake, having a practically symmetric expansion in the horizontal direction. Figure 5(f) shows a slimmer and sharper shape with an irregular expansion, characteristic of the stable wake, as well as a velocity deficit upstream of the wind turbine, a signature of the turbine-wake interaction. Even though Fig. 5(e) should be showing a velocity deficit upstream of the wind turbine rotor, this is much more attenuated and practically nonexistent, due to the convective regime present during the unstable stratification. For the LSWF, there is no upstream velocity deficit due to the fact that in these cases there are no upstream turbines. Also, it should be noted that for the stable-VLWF case in Fig. 5(f), as a result of the overall wind reduction, the wake deficit is attenuated in comparison to the stable-LSWF case in Fig. 5(h). In general, a more rapid wake recovery is observed for the unstable-VLWF case, with the wake recovering to 90% of the inflow wind speed at $5D$ and $6D$ downstream from the rotor disk for the unstable-VLWF and unstable-LSWF cases, respectively.

B. Mean kinetic energy fluxes around a characteristic wind turbine

The MKE terms previously described in Sec. II are now redefined within the LES framework and the terms used in the following expression will be used from now on:

$$0 = A + P + \phi + \epsilon + G_a + P_{\mathrm{WT}} + C_g. \tag{8}$$

In this expression, A represents the advection term, denoted by A_1 in Eq. (3). The work due to pressure gradients on the mean flow is denoted by P and ϕ denotes the turbulent flux of MKE; these two terms correspond to the first and second terms denoted by A_2 in Eq. (3). The dissipation term, denoted by ϵ in expression (8), corresponds to the term A_3 and the gravitational acceleration of vertical motions is represented by G_a, which corresponds to the term A_5. Note that the difference between the terms A_5 and G_a [see Eq. (9)] is due to the use of the Boussinesq approximation within the LES framework. The wind turbine power extraction is identified by P_{WT} and corresponds to term A_6; finally, C_g denotes the effect of the Coriolis forcing, which corresponds to the term A_7 in Eq. (3). Notice that the third term from A_2 and the term A_6 are representative of the viscous effects, which are being neglected, as is traditional in LES of atmospheric flows because the atmospheric flow is characterized by a very large Reynolds number. Therefore, following Eqs. (2) and (3) from Sec. II, the corresponding terms of the MKE budget using the LES framework are

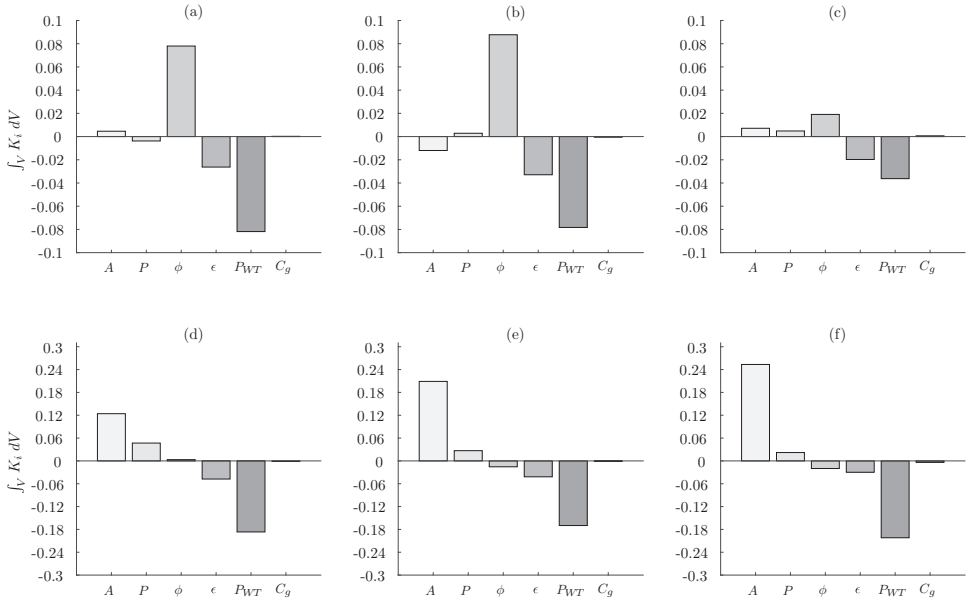

FIG. 6. Bar representation of the volume integral for the different MKE terms (K_i) within the wind turbine box. The subindex i represents the different terms contributing to the MKE budget (8), where A, P, ϕ, ϵ, P_{WT}, and C_g represent the advection, work due to pressure gradients on the mean flow, turbulent flux of MKE, dissipation, wind turbine power extraction, and the Coriolis effect, respectively. The VLWF case is shown for (a) unstable, (b) neutral, and (c) stable stratifications. The LSWF case is shown for (d) unstable, (e) neutral, and (f) stable stratifications.

represented by

$$A = -\overline{U}_j \frac{\partial K}{\partial x_j}, \quad P = -\frac{\overline{U}_i}{\rho}\frac{\partial \overline{P}}{\partial x_i}, \quad \phi = -\frac{\partial(\overline{\tau}_{ij}\overline{U}_i)}{\partial x_j}, \quad \epsilon = \overline{\tau}_{ij}\frac{\partial \overline{U}_i}{\partial x_j},$$
$$G_a = -g\left(\frac{\overline{U}_i\overline{\theta}}{\theta_{\text{ref}}}\right)\delta_{i3}, \quad P_{\text{WT}} = \overline{U}_i\overline{f}_i^{\text{WT}}, \quad C_g = f_c\epsilon_{ij3}\overline{U_iU_j}, \tag{9}$$

where $\overline{\tau}_{ij} = \overline{u_i'u_j'} + \overline{\tau}_{ij}^{\text{SGS}}$ is the sum of the Reynolds number and the subgrid scale shear stress.

Figure 6 illustrates the integral for the previously described MKE terms within the CV. This figure best illustrates the differentiated behavior in the wake recovery between the VLWF and the LSWF. For the VLWF [Figs. 6(a)–6(c)], the power harvested by the turbines corresponds to the remaining balance between the MKE dissipation and the turbulent flux of MKE; the contribution of the flux of MKE into the power harvested represents 72%, 79%, and 34% for the unstable, neutral, and stable regimes, respectively. Then it is concluded that in this case, the transport term is mainly responsible for the recovery of MKE within the turbine region, where the advection and pressure redistribution terms only provide a marginal contribution to the budget balance. In contrast, for the LSWF [Figs. 6(d)–6(f)] the harvested power is recovered mainly through the advection term (being 83%, 98%, and 109% with respect to the sum of the harvested power and dissipation for the unstable, neutral, and stable regimes, respectively) and the pressure redistribution (being 20%, 13%, and 9% with respect to the sum of the harvested power and dissipation for the unstable, neutral, and stable regimes, respectively). Note that for the LSWF scenarios the budget has a residual of 3%, 11%, and 18% for the unstable, neutral, and stable regimes, respectively. Also, it is relevant to note a factor of

2 between the advection term for the unstable [Fig. 6(d)] and stable [Fig. 6(f)] stratification cases for the LSWF cases.

This section should be concluded by stating that for the VLWF scenarios, independently of the flow stratification, the MKE is transported mainly by turbulent flux, decreased by viscous dissipation and power extracted by the wind turbine. Instead, the LSWF case is highly dependent on the stratification and differences are observed among the different regimes. While the MKE is always decreased by viscous dissipation and power extraction for the three studied stability conditions, emphasis should be placed on how the MKE is recovered or transported. While for the unstable stratification the MKE is mainly recovered within the CV by advection, pressure, and a very small contribution of turbulent flux of MKE, in the stable case the balance is practically due to advection with a very small contribution of the pressure term, with the turbulent flux having a negative contribution, also depicted in the neutral-LSWF case. In addition, the neutral case is a scenario that fits in between the unstable and stable cases.

To observe further details of the flow around an isolated wind turbine and the flow around a turbine within a large wind farm, the terms contributing to the budget of the MKE are now represented using a spatially distributed wind turbine box analysis, as presented in Sec. II. For example, Fig. 7 illustrates the contribution of the surface terms of MKE (A, ϕ, and P) through the control surface delimiting the wind turbine box, as well as horizontal slices at different heights ($z_h - D/2$, z_h, and $z_h + D/2$), of the volumetric terms contributing to the MKE budget (P_{WT}, ϵ, and C_g). The case represented in Fig. 7 corresponds to the LSWF case during the unstable regime. Influx terms to the CV are considered positive, while the outflux terms are considered negative. Each ones of the top six subplots represents a different side of the wind turbine box (front S_1, back S_2, right S_3, left S_4, bottom S_5, and top S_6 lids). The subplot located at the center represents the right plane S_3 of the box and the upper and lower ones represent the top S_6 and bottom S_5 lids, respectively. Note that these lids have the vertical axis inverted, so they perfectly connect with the right-side plane. Next the centered left and centered right subplots represent the front S_1 and back S_2 faces of the wind turbine box. Finally, the isolated, top left subplot represents the left plane of the box S_4. Within the front side, the geometry of the rotor disk is delineated with a dashed black line for the sake of reference. Note that the front plane S_1 is taken $2D$ upstream of the rotor disk.

Of special interest is the top lid subplot S_6, where an outflow of MKE can be observed from $2D$ upstream of the rotor disk to the rotor disk plane. Right behind the rotor disk, an entrainment region is observed for about $2D$ and then an outflow of MKE is measured, linked to the wake growth. An inverted behavior between the left and right sides of the wind turbine box is also present as a result of the rotation of the wake. There exists an influx at the top half of the right side of the surface S_3 with an outflux on the lower side. The opposite trend is shown on the left side, surface S_4. Finally, there is only an outflux of MKE through the back of the wind turbine box S_2. It is interesting to note that the outflux pattern is directly related to the wake of the turbine, which is vertically slanted.

To complete the picture, the spatial contribution of the MKE volumetric terms are also considered and represented through the lower 9 subplots in Fig. 7. These terms illustrate the contribution to the MKE of the Coriolis forcing (left column), the dissipation of MKE (middle column), and the power extracted by the turbines from the atmospheric flow (right column). Within each column, the different rows illustrate slices of the volume terms at different heights. From top to bottom these correspond to $z_h + D/2$, z_h, and $z_h - D/2$. In all plots, the contribution of the turbine wake and turbine rotor are quite apparent. In C_g, the turbine influences the term as two dipole features appear immediately at the rotor disk and these depend on the vertical location z, being most marked at midspan $z = z_h$. The signature in the wake is contrary to that at the rotor but with lessened magnitudes. When considering the dissipation term ϵ, once again as a function of height, it shows the signature of the rotor disk, strongly marking the lateral wind turbine effects at hub height and intensively noticeable at the center location of the wind turbine for the top and bottom plots. Finally, a significant sink is present at the exact location of the disk corresponding to the term P_{WT}. The diffuse effect of the rotor disk is due to the continuous realignment of the rotor throughout the 1-h-averaging period.

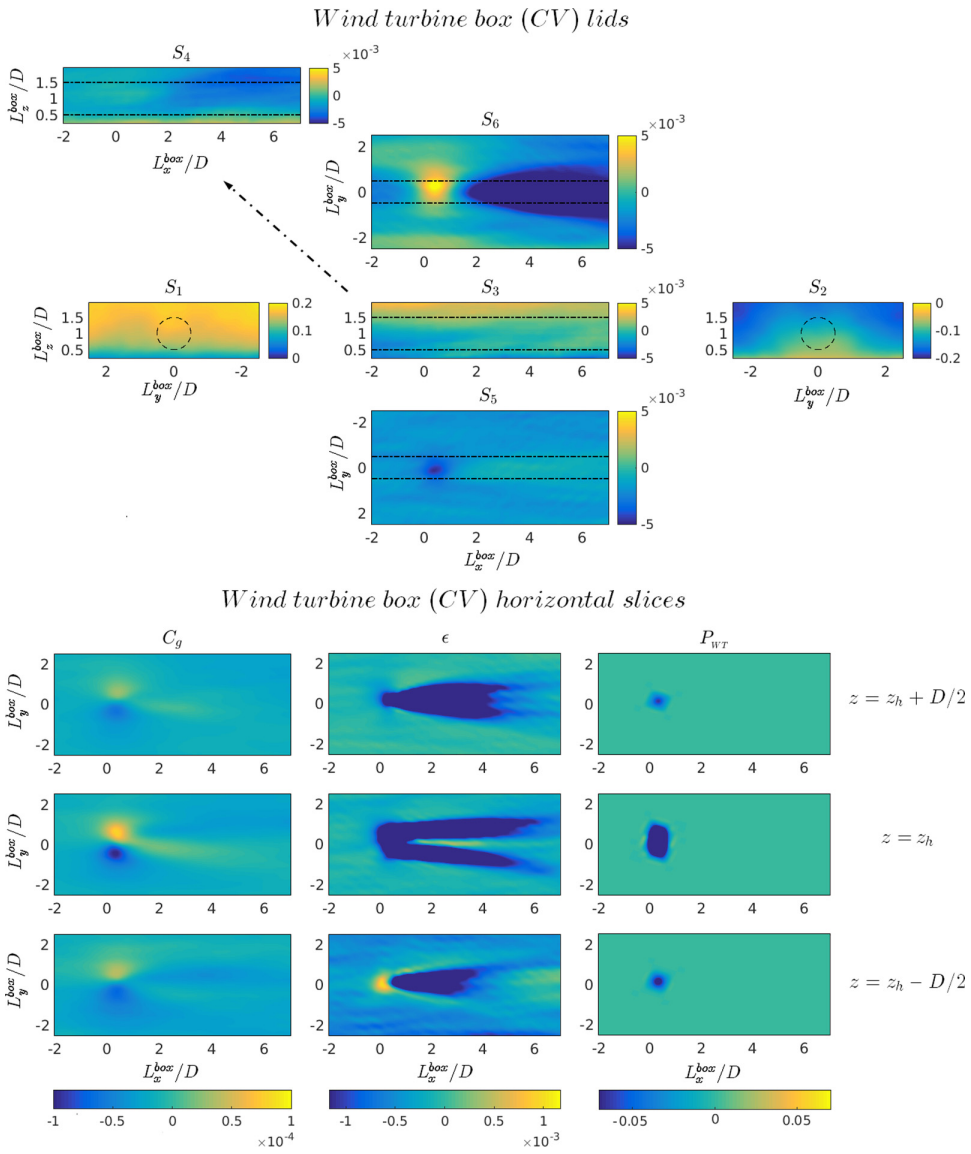

FIG. 7. Shown on top is a representation of the contribution of the surface MKE terms (sum of the advection A, turbulent flux ϕ, and pressure term P) through the control surfaces at the different lids of the wind turbine box: front S_1, back S_2, right S_3, left S_4, bottom S_5, and top S_6. Shown on the bottom are horizontal slices at different heights ($z_h - D/2$, z_h, and $z_h + D/2$) for the volume terms (C_g, ϵ, and P_{WT}) contributing to the MKE budget normalized by the geostrophic velocity and the wind turbine diameter (D/U_G^3). The top and bottom plots are representative of the 1-h averaged data for the LSWF case during the unstable regime.

In considering all cases, Fig. 8 represents streamwise profiles of the CV vertically integrated flux terms, through the lateral surfaces S_3 and S_4. Also, streamwise profiles of horizontally integrated flux terms through the bottom and top surfaces S_5 and S_6, respectively, are shown. While the wake recovery process is fully captured with this wind turbine box size for the VLWF case, for the LSWF

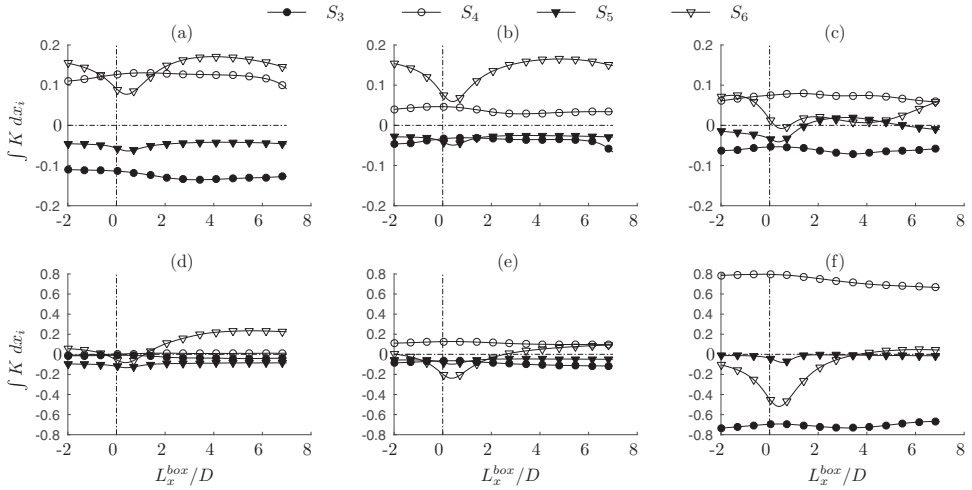

FIG. 8. Streamwise profiles of the wind turbine box, vertically integrated flux terms through the bottom S_5 and top S_6 lids and streamwise profiles of the wind turbine box horizontally integrated flux terms through the right S_3 and left S_4 surfaces. The flux terms are normalized by the cube of the geostrophic wind, the diameter of the wind turbine, and the length of the wind turbine box over which the integral is computed $D/U_G^3 L_i^{\text{box}}$, where $i = 1,3$. (a)–(c) The VLWF case and (d)–(f) the LSWF case for the unstable, neutral, and stable stratification, respectively. The vertical dashed line denotes the location of the wind turbine rotor.

case it is not, given the large extent of the wake. However, the same turbine box is used for one-to-one comparisons. Asymmetry is present in the lateral fluxes of MKE for all studied cases, meaning that the MKE entering through one side S_4 leaves almost entirely through the other side S_3 throughout the entire length of the CV. With opposite behavior, the flux of MKE through the top lid is highly dependent on the case, thus reflecting the influence of atmospheric stratification and number of turbines. For the VLWF case during the unstable regime [see Fig. 8(a)], an asymmetry exists in the MKE fluxes through the top and bottom lids. Clearly, a net influx (58% with respect to the total influx at $4D$ downstream of the wind turbine rotor) of MKE penetrates through the top lid and the flux through S_4 results in the same order of magnitude. A similar trend for the influx through the top lid S_6 is present during the VLWF neutral stratification, resulting in an influx of 84% with respect to the total influx at $4D$ downstream of the wind turbine rotor [see Fig. 8(b)]. Here a reduction of the horizontal flux is shown, being this close to 6 times smaller than the flux through S_6. Interestingly, the stable-VLWF shows a practically null vertical entrainment from the wind turbine rotor to $6D$ downstream, where the vertical MKE flux through the top lid S_6 starts to show up. This case is mainly driven by horizontal MKE flux through lid S_4. For the distinct LSWF scenarios, vertical entrainment of MKE is barely visible, except for the unstable case, where the flux through the top lid becomes important from $2D$ downstream of the rotor disk. It is interesting to note that for the stable LSWF, the horizontal flux of mean kinetic energy is remarkable, occurring along the entire length of the wind turbine box. Also, it should be noted that this case and the neutral-LSWF case are the only ones that present a negative flux through S_6 after the wind turbine rotor. This means that there exists an outflux of MKE resulting from the vertical expansion of the wake.

By integrating the MKE fluxes through the corresponding CV faces, it is possible to better quantify the relevance of the vertical entrainment of MKE in the recovery process of the depletion of MKE induced by the presence of the turbines. This is illustrated in Fig. 9 by means of a bar representation. Each bar indicates the corresponding contribution of MKE through each face of the wind turbine box (S_1, S_2, S_3, S_4, S_5, and S_6) and V represents the sum of the volume terms. As could be expected, the major inflow and outflow of MKE occurs through the front S_1 and back S_2 faces

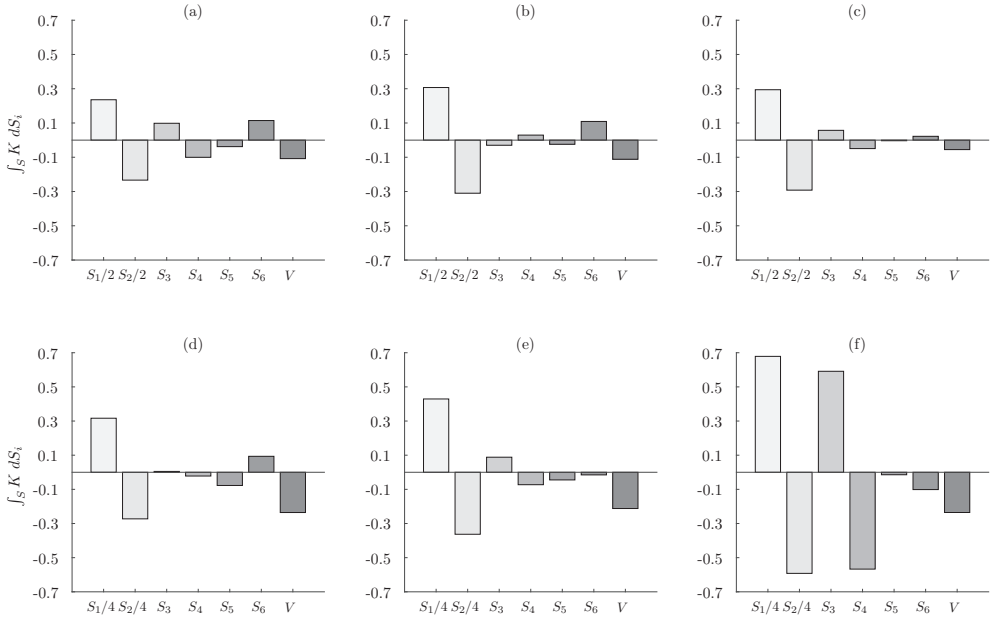

FIG. 9. Bar representation of the surface integral for the MKE flux through the distinct surfaces and volume terms. Each bar indicates the corresponding contribution of MKE through each face of the wind turbine box (S_1, S_2, S_3, S_4, S_5, and S_6) and V represents the sum of the volume terms within the control volume. The flux terms are normalized by the geostrophic wind and the diameter of the wind turbine resulting ($1/U_G^3 D^2$). The VLWF case is shown for (a) unstable, (b) neutral, and (c) stable stratification and the LSWF case is shown for (d) unstable, (e) neutral, and (f) stable stratification. Notice that for the VLWF subplots, terms S_1 and S_2 are divided by 2 and for the LSWF subplots, the same terms are divided by 4 in order to be able to visualize the magnitude of the rest of the terms.

of the wind turbine box. Note that the represented terms through faces S_1 and S_2 are divided by a factor of 2 for the VLWF and a factor of 4 for the LSWF case, for the sake of a better comparison of these terms. Furthermore, in the VLWF case these contributions are almost perfectly asymmetrical (influx S_1 versus outflux S_2) totaling to 0.48 and -0.46 for the unstable stratification [Fig. 9(a)], 0.62 and -0.62 for the neutral one [Fig. 9(b)], and 0.58 and -0.58 for the stable one [Fig. 9(c)]. Interestingly, this behavior is not as clear for the LSWF, where the values are 1.28 and -1.08 for the unstable stratification [Fig. 9(d)], 1.72 and -1.44 for the neutral one [Fig. 9(e)], and 2.72 and -2.36 for the stable one [Fig. 9(f)]. In both the VLWF and the LSWF, a similar asymmetrical behavior is observed for the lateral fluxes of MKE, as previously noted in Fig. 8, and with values of 0.1 and -0.1 for the unstable VLWF [Fig. 9(a)], -0.03 and 0.03 for the neutral VLWF [Fig. 9(b)], and 0.06 and -0.05 for the stable VLWF [Fig. 9(c)]. The unstable-LSWF case results in 0.01 and -0.02 [Fig. 9(d)], the neutral-LSWF case in 0.09 and 0.07 [Fig. 9(e)], and the stable-LSWF case in 0.59 and 0.56 [Fig. 9(f)]. Finally, attention should be focused on the asymmetric contribution of MKE through the bottom and top lids of the VLWF case (S_5 and S_6, respectively). This is the mechanism providing the recovery of most of the MKE depleted within the CV by the wind turbine, with values of -0.04 and 0.12 for the unstable case [Fig. 9(a)], -0.03 and 0.11 for the neutral one [Fig. 9(b)], and -0.004 and 0.022 for the stable one [Fig. 9(c)]. For the LSWF the contribution of MKE flux through the bottom and top lids does not greatly affect the recovery of MKE, and it can also behave as an outflux of MKE, like in the neutral and stable cases [Figs. 9(e) and 9(f)], due to the vertical slanted shape of the wake, especially during the stable regime.

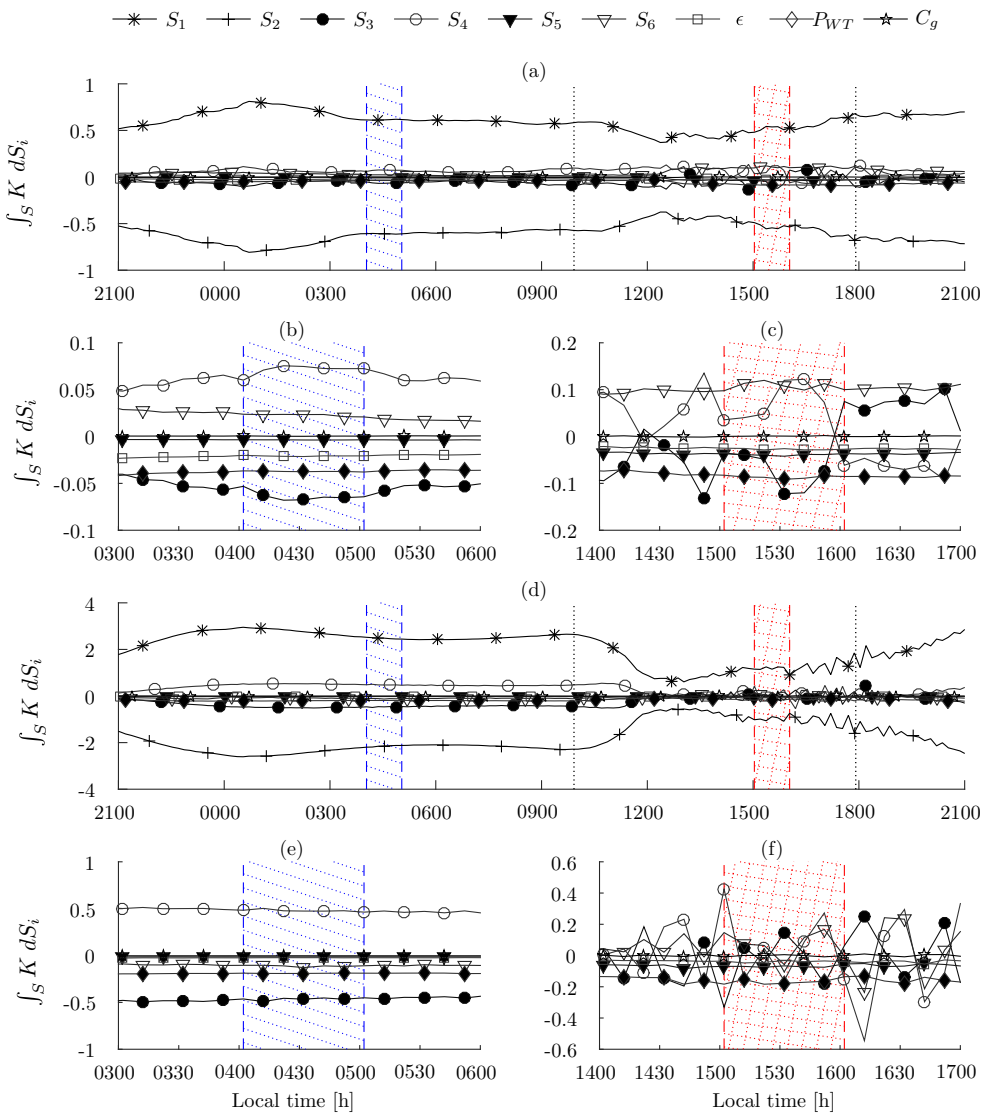

FIG. 10. Time-line representation of the 10-min-averaged surface integral for the MKE flux through the distinct surfaces (S_1, S_2, S_3, S_4, S_5, and S_6) and volume terms (ϵ, P_{WT}, and C_g) for the wind turbine box. The flux terms are normalized by the geostrophic wind and the diameter of the wind turbine resulting ($1/U_G^3 D^2$). (a)–(c) The VLWF case and (d)–(f) the LSWF case during the diurnal cycle. Notice that (b) and (c) are detailed views of the stable and unstable regimes for the VLWF case, respectively. (e) and (f) are detailed views of the stable and unstable regimes for the LSWF case, respectively.

To show the time evolution of the corresponding MKE contribution through the different surfaces of the wind turbine box, Fig. 10 represents the individualized volume terms, now averaged every 10 min instead of 1-h periods through the entire diurnal cycle. It corresponds to the previous bar plot (see Fig. 9) as a function of time and with the individualized contribution of each volume term. First, it is important to note that the behavior of the different terms does not exhibit variation as a function

of time for the represented periods (unstable and stable), illustrating that the 1-h averaging used throughout this study represents well the two different stratification regimes. Further, results illustrate that, continuously in time, the corresponding contributions through surfaces S_1 and S_2 remain the largest. It is worth noting the differentiated behavior between the VLWF and the LSWF cases: While the first almost presents negligible variation through the diurnal cycle, a more pronounced switch can be measured for the LSWF during the noon transition (between 10 a.m. and 1 p.m.) in the fluxes through S_1 and S_2. Also, for the VLWF the enhanced flux through S_5 is noticeable in comparison to S_6; $S_6 \approx 5S_5$ during the entire stable period [see Fig. 10(b)], reflecting the earlier observation that most of the wake recovery is produced as a result of the vertical transport of MKE. In contrast, for the LSWF it is the lateral flux through S_4 that contributes the most in the MKE recovery given that the fluxes through S_1 and S_2 almost perfectly compensate each other. It is also relevant to note the differentiated behavior for both cases, the VLWF and the LSWF, between the unstable and stable stratification periods, with large lateral oscillations on the fluxes through surfaces S_3 and S_4 [see Figs. 10(c) and 10(f)].

VI. SUMMARY AND CONCLUSIONS

In this work an analysis of the distribution of the mean kinetic energy around a single wind turbine (LSWF) and a characteristic wind turbine of a very large wind farm under different atmospheric stability conditions (unstable, neutral, and stable) was carried out. To accomplish a fair comparison, a dynamically yawed control volume (wind turbine box) was utilized.

The results illustrate important characteristic differences in the recovery of MKE between a VLWF and a LSWF under different atmospheric conditions. As previously shown in other studies, the harvested power by the wind turbines changes throughout the diurnal cycle, with a stronger power output during daytime and a reduction during nighttime for the VLWF (reduction of 42%). This is a result of the enhanced mixing induced by the thermal stratification during daytime and the vertical shift of the LLJ during nighttime. In contrast, for the LSWF the maximum harvested power is obtained during nighttime since the LLJ directly impinges on the rotor disk with an increase of 15%. In relation to this and for the case of a VLWF, the recovery of MKE is strongly dominated by the turbulent flux of MKE (ϕ), which presents a decreasing intensity with changing ABL stratification (a 32% and a 63% decrease for the neutral and stable stratified cases with respect to the unstable case, respectively). In contrast, for the LSWF, the recovery of MKE is shown to be dependent on the turbulent flux of MKE, the pressure redistribution term, and the advection, with advection the most important contribution. During the daytime the MKE depleted by the wind turbine is recovered by a contribution of 83% and during the nighttime the advection terms has a contribution of practically 100%. For the neutrally stratified case, again almost the totality of the MKE recovery happens through the advection.

The analysis allows us to identify the geometrical redistribution of MKE around a characteristic wind turbine. While the MKE fluxes through the front and backward faces (S_1 and S_2) are, respectively, the largest source and sink of MKE, they correspondingly compensate each other. Hence, the actual MKE recovery happens through the lateral (S_3 and S_4) and vertical (S_5 and S_6) faces of the wind turbine box. The results clearly illustrate that during the convective regime the fluxes through the vertical faces of the wind turbine box dominate, while during the stable stratification the fluxes through the lateral surfaces are most important.

Finally, the results also illustrate the fact that during the unstable regime the turbulent mixing around the wind turbines is dominated by the background atmospheric stratification, given that both the LSWF and the VLWF present a similar vertical shear at the top tip of the rotor disk (only an 8% difference). In contrast, during the nighttime, the mixing is dominated by the actual wind turbines, which is demonstrated by a much larger difference between the LSWF and VLWF vertical shear stress at the top tip of the rotor disk (a 90% difference).

ACKNOWLEDGMENTS

M.C. acknowledges the Mechanical Engineering Department at University of Utah for start-up funds. R.B.C. thanks the National Science Foundation for their support (Grant No. NSF-CBET-1034581). The authors would like to recognize the computational support provided by the Center for High Performance Computing at University of Utah.

[1] GWEC, Global Wind Report, 2014 (unpublished).

[2] N. D. Kelley and H. J. Sutherland, *Proceedings of the 35th Aerospace Sciences Meeting and Exhibit* (AIAA, Reston, NV, 1997), AIAA paper 97-0950, pp. 1–10.

[3] C. Sim, S. Basu, and L. Manuel, On space-time resolution of inflow representations for wind turbine loads analysis, Energies **5**, 2071 (2012).

[4] M. J. Churchfield, S. Lee, J. Michalakes, and P. J. Moriarty, A numerical study of the effects of atmospheric and wake turbulence on wind turbine dynamics, J. Turbul. **13**, 1 (2012).

[5] H. Lu and F. Porté-Agel, On the impact of wind farms on a convective atmospheric boundary layer, Bound.-Layer Meteor. **157**, 81 (2015).

[6] D. Yang, C. Meneveau, and L. Shen, Large-eddy simulation of offshore wind farm, Phys. Fluids **26**, 025101 (2014).

[7] C. VerHulst and C. Meneveau, Large eddy simulation study of the kinetic energy entrainment by energetic turbulent flow structures in large wind farms, Phys. Fluids **26**, 025113 (2014).

[8] M. Abkar and F. Porté-Agel, The effect of free-atmosphere stratification on boundary-layer flow and power output from very large wind farms, Energies **6**, 2338 (2013).

[9] M. Abkar and F. Porté-Agel, Mean and turbulent kinetic energy budgets inside and above very large wind farms under conventionally-neutral condition, Renew. Energ. **70**, 142 (2014).

[10] C. VerHulst and C. Meneveau, Altering kinetic energy entrainment in large eddy simulations of large wind farms using unconventional wind turbine actuator forcing, Energies **8**, 370 (2015).

[11] M. Calaf, C. Meneveau, and J. Meyers, Large eddy simulation study of fully developed wind-turbine array boundary layers, Phys. Fluids **22**, 015110 (2010).

[12] R. B. Cal, J. Lebrón, L. Castillo, H. S. Kang, and C. Meneveau, Experimental study of the horizontally averaged flow structure in a model wind-turbine array boundary layer, J. Renew. Sustain. Energ. **2**, 013106 (2010).

[13] M. Calaf, M. B. Parlange, and C. Meneveau, Large eddy simulation study of scalar transport in fully developed wind-turbine array boundary layers, Phys. Fluids **23**, 126603 (2011).

[14] H. Lu and F. Porté-agel, Large-eddy simulation of a very large wind farm in a stable atmospheric boundary layer, Phys. Fluids **23**, 065101 (2011).

[15] F. Porté-Agel, H. Lu, and Y. Wu, *23rd International Congress of Theoretical and Applied Mechanics* (Elsevier, Amsterdam, 2014), Vol. 10, pp. 307–318.

[16] B. Witha, G. Steinfeld, M. Dörenkämper, and D. Heinemann, Large-eddy simulation of multiple wakes in offshore wind farms, J. Phys.: Conf. Ser. **555**, 012108 (2014).

[17] M. Dörenkämper, B. Witha, G. Steinfeld, D. Heinemann, and M. Kühn, The impact of stable atmospheric boundary layers on wind-turbine wakes within offshore wind farms, J. Wind Eng. Ind. Aerodyn. **144**, 146 (2015).

[18] G. S. Poulos, W. Blumen, D. C. Fritts, J. K. Lundquist, J. Sun, S. P. Burns, C. Nappo, R. Banta, R. Newsom, J. Cuxart, E. Terradellas, B. Balsley, and M. Jensen, CASES-99: A comprehensive investigation of the stable nocturnal boundary layer, Bull. Am. Meteor. Soc. **83**, 555 (2002).

[19] V. Kumar, G. Svensson, A. A. M. Holtslag, C. Meneveau, and M. B. Parlange, Impact of surface flux formulations and geostrophic forcing on large-eddy simulations of diurnal atmospheric boundary layer flow, J. Appl. Meteor. Climat. **49**, 1496 (2009).

[20] V. Kumar, J. Kleissl, C. Meneveau, and M. B. Parlange, Large-eddy simulation of a diurnal cycle of the atmospheric boundary layer: Atmospheric stability and scaling issues, Water Resour. Res. **42**, 1 (2006).

[21] G. Svensson *et al.*, Evaluation of the diurnal cycle in the atmospheric boundary layer over land as represented by a variety of single-column models: The second GABLS experiment, Bound.-Layer Meteor. **140**, 177 (2011).

[22] S. Basu, J. F. Vinuesa, and A. Swift, Dynamic LES modeling of a diurnal cycle, J. Appl. Meteor. Climat. **47**, 1156 (2007).

[23] V. Sharma, M. B. Parlange, and M. Calaf, Perturbations to the spatial and temporal characteristics of the diurnally-varying atmospheric boundary layer due to an extensive wind farm, Bound.-Layer Meteor. **161**, 1 (2016).

[24] G. Cortina, V. Sharma, and M. Calaf, Investigation of the incoming wind vector for improved wind turbine yaw-adjustment under different atmospheric and wind farm conditions, Renew. Energ. **101C**, 376 (2017).

[25] A. C. Fitch, J. K. Lundquist, and J. B. Olson, Mesoscale influences of wind farms throughout a diurnal cycle, Mon. Weather Rev. **141**, 2173 (2013).

[26] V. Sharma, M. Calaf, M. Lehning, and M. B. Parlange, Time-adaptive wind turbine model for an LES framework, Wind Energy **19**, 939 (2016).

[27] M. Abkar, A. Sharifi, and F. Porté-Agel, Wake flow in a wind farm during a diurnal cycle, J. Turbul. **17**, 420 (2016).

CHAPTER 5

WIND FARM DENSITY AND HARVESTED POWER IN VERY LARGE WIND FARMS: A LOW-ORDER MODEL

Physical Review Fluids (2017) 2, 074601. Wind farm density and harvested power in very large wind farms: A low-order model. G. Cortina, V. Sharma, M. Calaf.

PHYSICAL REVIEW FLUIDS **2**, 074601 (2017)

Wind farm density and harvested power in very large wind farms: A low-order model

G. Cortina,[1,*] V. Sharma,[2] and M. Calaf[1]
[1]*Department of Mechanical Engineering, University of Utah, Salt Lake City, Utah 84112, USA*
[2]*School of Architecture, Civil and Environmental Engineering, EPFL, Lausanne, Switzerland*
(Received 2 November 2016; published 5 July 2017)

In this work we create new understanding of wind turbine wakes recovery process as a function of wind farm density using large-eddy simulations of an atmospheric boundary layer diurnal cycle. Simulations are forced with a constant geostrophic wind and a time varying surface temperature extracted from a selected period of the Cooperative Atmospheric Surface Exchange Study field experiment. Wind turbines are represented using the actuator disk model with rotation and yaw alignment. A control volume analysis around each turbine has been used to evaluate wind turbine wake recovery and corresponding harvested power. Results confirm the existence of two dominant recovery mechanisms, advection and flux of mean kinetic energy, which are modulated by the background thermal stratification. For the low-density arrangements advection dominates, while for the highly loaded wind farms the mean kinetic energy recovers through fluxes of mean kinetic energy. For those cases in between, a smooth balance of both mechanisms exists. From the results, a low-order model for the wind farms' harvested power as a function of thermal stratification and wind farm density has been developed, which has the potential to be used as an order-of-magnitude assessment tool.

DOI: 10.1103/PhysRevFluids.2.074601

I. INTRODUCTION

Adjusting to the need of every community, the use of wind energy has been spreading around the world, either as lone standing turbines, or conforming large wind farms. Some of the advantages of installing large wind farms are the reduction in cost of energy transport, ease of connecting to the electrical grid [1], and reduced costs in land leases and permits [2], to mention a few. However, when several turbines are grouped together the corresponding turbulent wakes interact with each other [3], reducing the harvested power per wind turbine unit [4], and increasing turbines loads and fatigue [5]. Also, the capacity of the atmospheric flow to immediately recover after circulation through a succession of wind turbines is limited, and differs with atmospheric stratification [6]. Generally, the arrangement of turbines, aligned or staggered [7,8], is determined by the amount of terrain available, the local topography, and local atmospheric conditions. In either case, turbines are packed in an attempt to optimize the cost-benefit ratio.

To date, there have been many studies investigating the benefits and limitations of staggered versus aligned turbine arrangements, with results showing a dominant effect of the streamwise versus the spanwise spacing [9–11]. For example, Yang *et al.* [9] used large-eddy simulations (LESs) to evaluate the effects of turbines' spacing in very large aligned wind farms. Results demonstrated that by increasing the streamwise spacing the harvested power would increase and turbulence intensity decrease. Similarly, Meyers and Meneveau [12] used the wind farm induced surface roughness model of Calaf *et al.* [13] to investigate optimal wind turbine spacings for enhanced harvested power. Results determined that the optimal average streamwise spacing should be of the order of 15 wind turbine diameters, which is considerably higher than current spacings. In this line,

*gerard.cortina@utah.edu; http://wet.mech.utah.edu/

recent numerical simulations of finite size wind farms [11] have further demonstrated that the power output in the fully developed wind farm region depends primarily on the geometric mean turbine spacing (defined as $s = \sqrt{s_x s_y}$, where s_x and s_y indicate the streamwise and spanwise spacings, respectively), with a stronger dependence on the streamwise spacing in the aligned configurations. Additional results of Son *et al.* [14] have also demonstrated that the spacing between the first and second row of wind turbines forming a wind farm strongly affects the overall system efficiency.

An additional complexity factor is the fact that realistic atmospheric flows show significant spatiotemporal variability, hence leading to changes in an effective wind farm's arrangement. For example, recent work of Sharma *et al.* [4] illustrates that under neutral and stable stratified flows, wind turbines are well aligned as a result of a uniform mean flow direction. However, during convective regimes turbines often reorientate according to the variable local wind vector. Therefore, determining an utmost convenient wind farm arrangement remains a very complex task. To facilitate deeper understanding in this matter, a diverse set of numerical and experimental studies were developed in the past. Some examples are the works of Hansen *et al.* [15], Fitch *et al.* [16], Zhang *et al.* [17], Abkar and Porté-Agel [18,19], Peña and Rathmann [20], Peña *et al.* [21,22], Bhaganagar and Debnath [23,24], Abkar *et al.* [25], El-Askary *et al.* [26], and Stevens and Meneveau [27]. For instance, results from Peña *et al.* [21] showed that under a stable stratified Atmospheric Boundary Layer (ABL) the power deficit is a maximum, while under convective conditions the power deficit is a minimum. In this regard, Abkar and Porté-Agel [19] and Cortina *et al.* [6] reported how the extent and shape of the turbines' wakes change as a function of the background atmospheric stratification, showing that atmospheric stability has a significant effect on the spatial distribution of the mean velocity deficit and turbulence statistics in the wake region, as well as in the wake meandering characteristics. For example, under convective conditions the enhanced turbulence associated with positive buoyancy leads to a relatively larger flow entrainment and a faster wake recovery; contrarily, during stable stratified periods, wakes extend longer. It has also been illustrated that wake meandering is stronger under convective regimes, compared to neutral and stable stratified cases. These findings have also been verified with experimental data from the Horns Rev wind farm [15,22,28]. At present, several optimization and control approaches are being developed to increase the number of turbines per unit area, while reducing the corresponding turbine wakes' interactions. One of these techniques consists of using upstream scanning wind lidars to timely learn about the incoming wind conditions [29–36] and purposely misalign the wind turbine with the incoming wind, steering the wake to favorably reduce interactions with downstream turbines [37–39].

Within this work we aim to create knowledge on the wake recovery processes as a function of wind farm density, regardless of turbine arrangement. We claim that by better understanding the intervening wake recovery mechanisms it will be possible to develop more efficient wind farms, with increased harvested power per turbine unit. Earlier works on very large wind farms [11–13,40,41] have shown by means of spatiotemporal averaged quantities over the full wind farm that the recovery of the wind turbine's wake is mainly due to the vertical flux of mean kinetic energy (MKE). In this regard, the work of Stevens *et al.* [11] showed that the turbines' power output is well correlated with the vertical flux of MKE. They further demonstrated that the vertical flux of MKE is more localized along turbine columns in aligned farm arrangements than in staggered ones, leading to faster wake recoveries. Differently, in this study, we aim to examine the wake recovery process as a function of wind farm density using a local approach. For this purpose, a detailed MKE budget analysis is performed following the procedure presented by Cortina *et al.* [6]. From this analysis, a low-order model is developed that determines the harvested power of the wind turbines as a function of the wind farm density and atmospheric stability.

In Sec. II, a brief description of the wind farm numerical simulations is provided. Section III describes the distinct study cases and Sec. IV presents the mean kinetic energy budget analysis. In Sec. V, the low-order model is developed, where results are tested against the numerical data. Finally, in Sec. VI a sensitive analysis for error propagation is presented to illustrate the robustness of the low-order model. Conclusions are presented in Sec. VII.

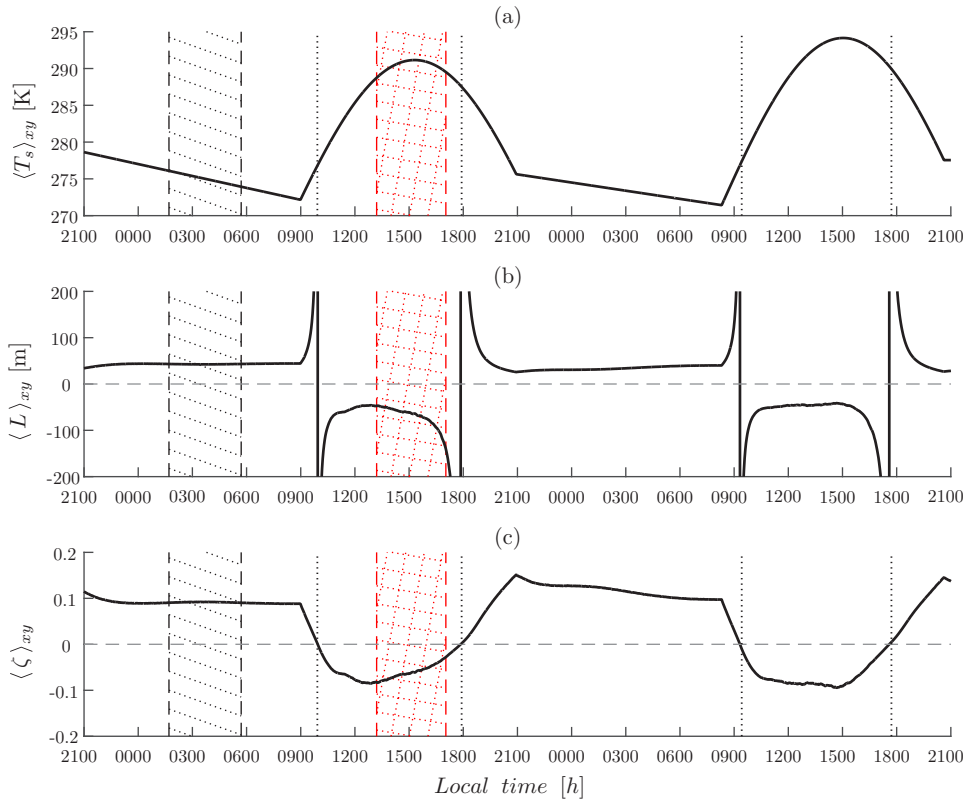

FIG. 1. (a) Spatially averaged and time-dependent imposed temperature at the surface of the domain, $\langle T_s \rangle_{xy}$, in kelvin during the evolution of two consecutive diurnal cycles; (b) the Monin-Obukhov length, $\langle L \rangle_{xy}$, in meters; and (c) the normalized stability parameter, $\langle \zeta \rangle_{xy} = z_1/\langle L \rangle_{xy}$, where z_1 is the height of the LES first grid point. The lateral brackets denote the planar average operation in the streamwise and spanwise directions. Two different periods marked with 45° dotted lines, in black, and squared dotted lines, in red, delineate time periods in which representative statistics are computed. Precisely, the first time period constitutes times between 01:45 and 05:45 local time and the second period denotes the time between 13:15 and 17:15 local time. The vertical dotted lines denote the change in stability, i.e., when $\langle \zeta \rangle_{xy} = 0$ or when $\langle L \rangle_{xy} \to \infty$. In (b) and (c) the horizontal dashed line depicts the zero value as a reference point.

II. LARGE-EDDY SIMULATION FRAMEWORK

The numerical code integrates the nondimensional and filtered Navier-Stokes equations, together with conservation of mass and an advection-diffusion equation for temperature using an LES approach. In this numerical framework, the thermal effects are coupled to the momentum equations using the Boussinesq approximation [42]. As is traditional in LES, only the energy-containing turbulent eddies are numerically resolved, and the effect of the smaller eddies is parametrized through a subgrid-scale model. The flow is forced using a time-constant and height-independent geostrophic wind equal to $(u_G, v_G) = (9, -3)\,\mathrm{ms}^{-1}$, together with a time varying surface temperature, represented in Fig. 1(a) for the evolution of two consecutive diurnal cycles. The surface temperature variation allows representation of a realistic diurnal cycle and corresponds to the experimental data set of the Cooperative Atmospheric Surface Exchange Study (CASES-99) field experiment [43]. This specific numerical simulation has been already used in other wind energy studies [4,6,16,35,36],

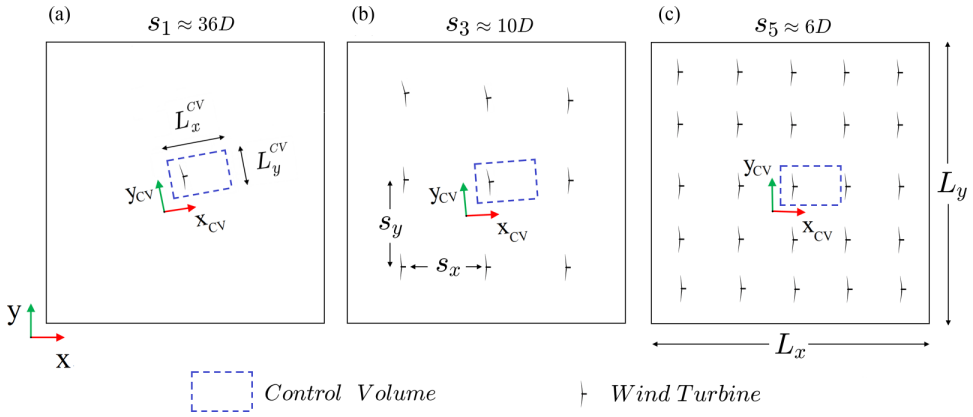

FIG. 2. (a) Case s_1, representative of 1 wind turbine located at the center of the LES domain; (b) case s_3 with a total of 9 wind turbines; and (c) case s_5 with a total of 25 wind turbines.

and for this reason it is also used here. During the evolution of this specific diurnal cycle, the ABL flow dynamically changes the thermal stratification as it transitions from nighttime to daytime, with neutral conditions being quite ephemeral. Consequently, an additional LES is considered to compute statistics under a neutral ABL stratification. For the neutral stratification, the flow is forced with the exact same geostrophic wind as the diurnal cycle, but with a constant surface temperature and a well-mixed vertical temperature profile. For all cases, the numerical domain has a lateral size equal to $L_x = L_y = \pi$ km, and a height of $z = 2$ km (see Fig. 2), and it is discretized by a total of $128\times128\times256$ grid points. As a result, the numerical resolution is 24.5 m in the streamwise and spanwise directions, and 7.8 m in the vertical direction. A pseudospectral approach is used to integrate the LES governing equations in the horizontal directions and, therefore, the numerical domain is periodic in the streamwise and spanwise directions. The initial height of the boundary layer top (z_i) is 1000 m, from which an inversion layer spans to the top of the numerical domain. In this study, the wind turbines are modeled using the actuator disk model with rotation and dynamic yaw alignment of Sharma *et al.* [44], with a yaw-readjustment time of 10 min [35,36]. The wind turbine diameter (D) is set to 100 m as well as the turbine's hub height. For further details on the numerical framework see Ref. [4].

III. STUDY CASES: WIND FARM ARRANGEMENT

To develop this study, a suite of two 4-h periods from the first diurnal cycle are selected (see Fig. 1). These two 4-h study periods are representative of two different characteristic ABL stratification regimes (unstable and stable), and because neutral stratifications are ephemeral during the evolution of the two diurnal cycles, a 4-h period is also selected from an independent LES study with a conventional neutrally stratified flow. The unstable and stable stratified periods are marked in Fig. 1 with black and red shadings for the stable and unstable regimes, respectively. Specifically, the selected stable period extends between 01:45 and 05:45, and the unstable period between 13:15 and 17:15, local time. For each stratification case, seven different wind farm arrangements have been considered to be representative of different wind farm densities, adding to a total of 21 study cases. Table I summarizes the distinct wind farm configurations, where study cases are referred as s_i, with i running from 1 to 7. In all cases, wind turbines' spacing is equidistant in both directions, streamwise and spanwise. This is illustrated in Figs. 2(a)–2(c) for cases s_1, s_3, and s_5, respectively. Each panel represents a different study case, with the corresponding LES domain and the corresponding number of turbines for that specific case. Note that because a pseudospectral approach is used to integrate the LES equations in the horizontal directions, the numerical domain is periodic in the streamwise

TABLE I. Summary of the different LES study cases for the different wind farm configurations from low (case s_1) to high (case s_7) wind farm density. The geometric mean turbine spacing is denoted by s, where $s = \sqrt{s_x s_y}$ with s_x denoting the streamwise and s_y denoting the spanwise spacing between turbines. The wind farm density is denoted by ρ_{wf}, in units of number of turbines per unit area in square kilometers.

Study case	No. of turbines	$s = \sqrt{s_x s_y}$	ρ_{wf} (no. of turbines/km^2)
s_1	1 (1×1)	$31D$	0.1
s_2	4 (2×2)	$16D$	0.5
s_3	9 (3×3)	$10D$	1.0
s_4	16 (4×4)	$8D$	1.5
s_5	25 (5×5)	$6D$	2.5
s_6	36 (6×6)	$5D$	3.5
s_7	49 (7×7)	$4.5D$	5.0

and spanwise directions and hence all wind farm configurations are in practice of infinite extent. However, also note that not in all cases does the turbulent flow reach a fully developed regime within the wind farm area. Specifically, in case s_1 turbines are spaced $31D$ apart and hence turbine-wake interactions are nonexistent and the turbulent flow does not reach a fully developed state leading to the so-called wind turbine array boundary layer limit (WTABL [13]). Contrarily, cases s_3 to s_7 present successive wind turbine–wake interactions and the turbulent flow becomes fully developed. Furthermore, depending on the ABL background stratification, case s_2 can be categorized as a stand-alone wind turbine (for unstable and neutral regimes), or as a very large wind farm (for stable regimes), where turbines are immersed in upstream turbine wakes.

Examples of the numerical domain configuration are presented in Fig. 2 for cases s_1, s_3, and s_5. In Fig. 2 the dashed blue box surrounding a wind turbine represents the control volume (CV) used to compute the local MKE budget. Note that each wind turbine of a given wind farm configuration is surrounded by a CV and statistics are averaged over all CVs of the same study case to extract a characteristic flow behavior. The CV has a streamwise distance (L_x^{CV}) that extends between a distance of $2D$ upstream of the wind turbine, down to a downstream distance where the turbine's velocity deficit recovers by 60%. The spanwise distance of the control volume is set to $L_y^{\mathrm{CV}} = 5D$, and the vertical dimension is set to $L_z^{\mathrm{CV}} = 2D$. For further details on the numerical algorithm used to compute the statistics within the local reference frame of the CV, see Ref. [6]. Cases are set such that case s_1 is representative of an isolated wind turbine, a result of the very large spacing between turbines, and it is used as reference in the following sections. On the other end of the spectrum, case s_7 corresponds to an extremely loaded case, with $s_x = s_y \approx 4.5D$.

IV. RESULTS

A. Wind farm density-dependent flow statistics

Figure 3 illustrates vertical slices of MKE for cases s_1, s_3, and s_5 under unstable, neutral, and stable atmospheric stratification. The MKE is computed as $K = \frac{1}{2}\overline{U_i}^2 = \frac{1}{2}(\overline{U}^2 + \overline{V}^2 + \overline{W}^2)$, with variables U, V, and W being the streamwise, spanwise, and vertical components of the wind vector, respectively. Statistics for the MKE are averaged over 4 h, and results are normalized with the square of the forcing geostrophic velocity.

From these vertical slices, two main characteristics are observed: (1) the MKE deficit increases with increasing wind farm density and (2) there is an increase in the length of the wind turbine wake with increasing thermal stability. From these results it is clear that the increased turbulent mixing during the unstable regime benefits wind turbine wake recovery, hence resulting in an overall smaller turbine footprint. Under neutral conditions thermally driven mixing is reduced and therefore there is a reduced recovery rate of the wind turbine wake. Finally, during the stable stratified case

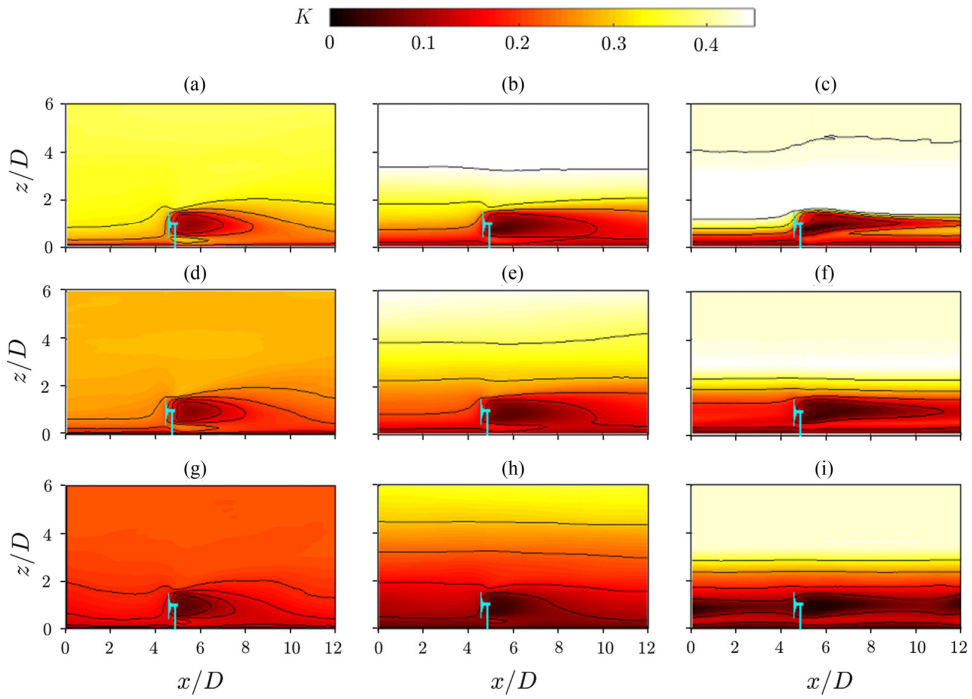

FIG. 3. Vertical slices of mean kinetic energy (K) normalized by the square of the geostrophic wind: (a), (d), (g) unstable stratified case, (b), (e), (h) neutral stratified case, and (c), (f), (i) stable stratified case. The first row (a)–(c) represents case s_1, the second row (d)–(f) represents case s_3, and the third row (g)–(i) represents case s_5.

the background turbulence is strongly attenuated and hence wakes persist for longer distances. These characteristic trends had already been observed in other earlier works [6,19,26,45–48]. Note for example the successive wake-turbine interactions illustrated in case s_5 under stable conditions [see Fig. 3(i)]. For the unstable case, it can be observed that the wake has a weak upward vertical displacement with downstream distance, with case s_1 showing the largest vertical displacement. This trend seems to weaken with increasing wind farm density. Contrarily, during the neutral regime turbine wakes seem to illustrate a weak downward vertical shift. It is also interesting to note the asymmetry of the wake during the stable period, being more intense at the top of the rotor disk and weaker near the ground. Interestingly, for the lightly loaded wind farm scenario, the wake deficit is mainly concentrated on the top half of the rotor-disk region, with a much faster wake recovery in the lower rotor-disk region. Another important result previously observed is the vertical shift of the low-level jet (LLJ) [4,16]. The LLJ is initially located at a height between 150 and 200 m for the s_1 case, and it is vertically displaced with increasing wind farm density, reaching a height of 200 and 300 m for cases s_3 and s_5, respectively. This vertical shift of the LLJ is also clearly detected in Fig. 4(c), where vertical profiles of MKE for all different study cases are presented. Note for example a vertical displacement of up to 200 m between cases s_1 and s_7. Overall, between cases s_2 and s_3, the vertical displacement is 50 m, thereby becoming much more reduced, reaching a certain stagnation between cases s_6 and s_7. A similar trend is observed for the MKE deficit in the wake region, specially at hub height. From the vertical profiles of MKE it is also interesting to note how the MKE deficit propagates vertically for the different wind farm cases. It is clear from the profiles in Fig. 4(a) that the influence of the wind farm propagates vertically up to the top of the boundary layer

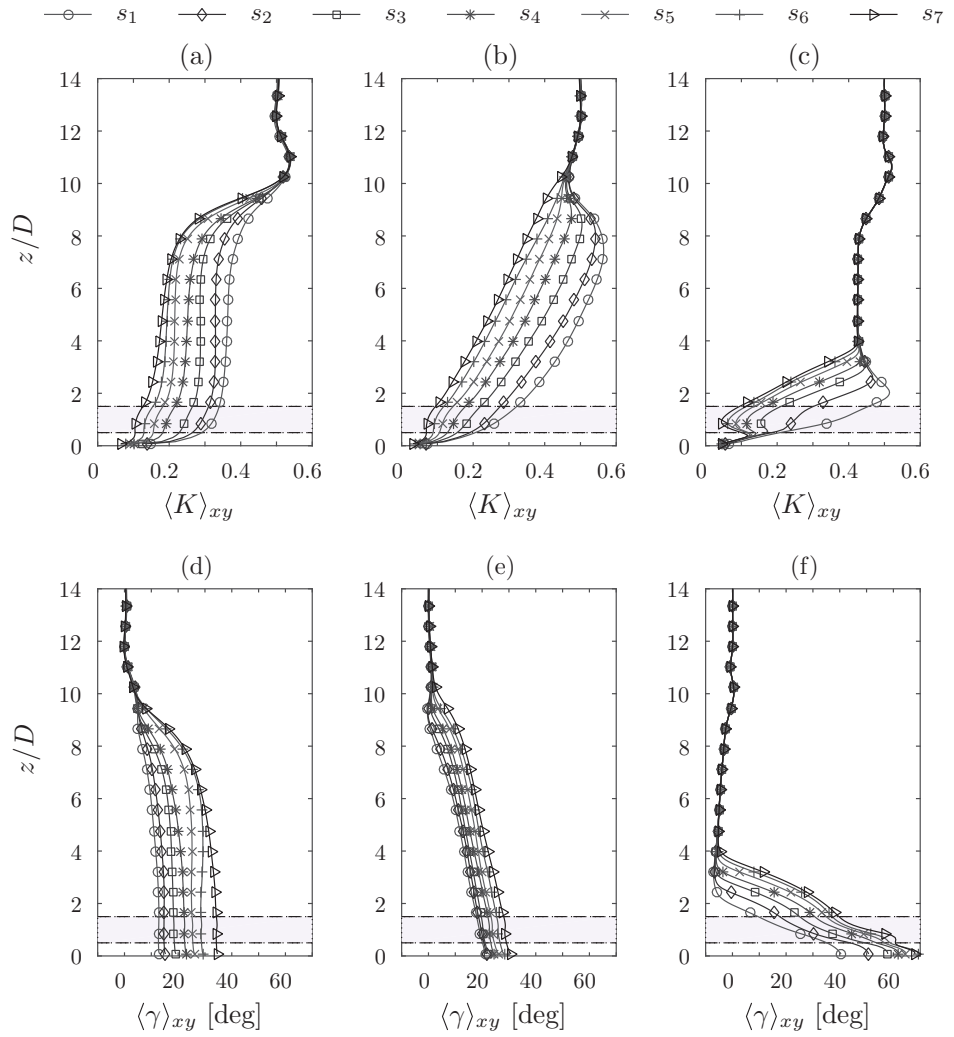

FIG. 4. The first row illustrates vertical profiles of MKE upon horizontal averaging over the LES domain, $\langle K \rangle_{xy}$, and normalized by the square of the geostrophic wind. The different lines represent results for the different wind farm density cases. Each thermal stratified regime is represented in a different column: (a) unstable, (b) neutral, and (c) stable. The bottom row represents vertical profiles of the wind veer ($\langle \gamma \rangle_{xy}$). The shaded area indicates the wind turbine rotor disk region, which ranges between $z = 0.5D$ and $z = 1.5D$.

(BL), hence affecting the entire ABL flow. For this study case, the imposed thermal inversion at the top of the BL is quite strong (3 K/100 m), and hence all cases seem to affect equally the entrainment region, regardless of wind farm loading. For the neutral case [see Fig. 4(b)], the MKE deficit follows a quasilinear profile as a function of height, with a proportional attenuation with increasing wind farm loading. In Fig. 4, we also illustrate the vertical profiles of wind veer [Figs. 4(d)–4(f)], which represent the rotation of the mean wind vector with height, related to the change in Coriolis balance as a result of the increase in wind farm loading. This is computed as $\langle \gamma \rangle_{xy} = \langle \tan^{-1}(\overline{V}/\overline{U}) \rangle_{xy}$, where $\overline{V}$ and $\overline{U}$ are the time-averaged spanwise and streamwise velocity components, respectively. The

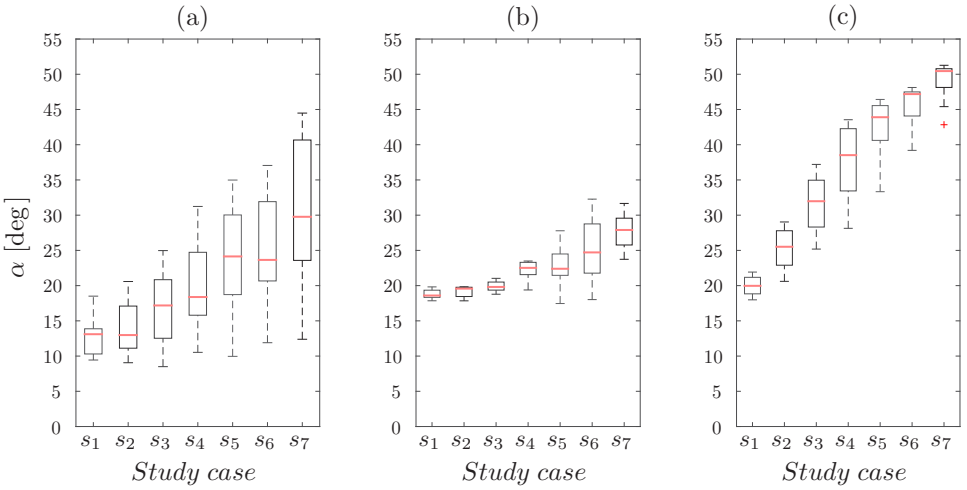

FIG. 5. Box plot based on a normal distribution of the wind turbines' yaw orientation for the different wind farm densities (from s_1 to s_7) and as a function of the atmospheric stability: (a) unstable, (b) neutral, and (c) stable.

lateral brackets denote horizontal averages over the LES domain. For all stratification cases, results illustrate an increase in wind veer with increasing wind farm loading, with a shift of $\sim$17°, 10°, and 30° between cases s_1 and s_7 for the unstable, neutral, and stable stratification regimes. The large increase during the stable regime is due to the fact that in this case most of the turbulent mixing occurring within the ABL is solely due to the wind turbines; hence the turbines' effect on the ABL is directly proportional to the wind farm density. For the unstable period, where the turbulent mixing is dominated by the convective eddies, the change in wind veer is reduced with an overall difference of 17°. Most important, however, is to note the vertical gradient in the wind veer through the rotor-disk region. This is very strong during the stable regime (24°/100 m), much reduced during the neutral regime (2.25°/100 m), and negligible during the unstable regime. This gradient in vertical veer induces strong loads on the wind turbine blades and towers and must be studied with care when assessing potential wind farm sites.

As mentioned earlier in Sec. II, the wind turbine model used in this work has the capacity to realign with the incoming wind vector, continuously correcting for the misalignment of the turbine's rotor disk with the incoming mean wind vector. Figure 5 illustrates the median of the turbine's yaw orientation for the different study cases together with the 25th and 75th percentiles of the yaw alignment. The distance between the top and bottom of the boxes is defined as the interquartile range, and the line in the middle of the box, represented in red, is the median of the yaw alignments. Note that in those cases where the median is not centered, it indicates a skewed distribution. Furthermore, the whiskers represent the furthest observations within the data. Finally, the outliers, marked with a red plus sign (+), display a value that is more than 1.5 times the interquartile range from the top or bottom of the box plot. From Fig. 5 it can be observed that the range of yaw alignments follows the wind veer values at the rotor-disk region illustrated earlier in Fig. 4. It is also interesting to note the increase in yaw angle with increasing wind farm loading. This progressive change in yaw angle is a result of the change in drag near the surface, affecting the geostrophic balance, and hence it is different for each stratification regime. More interesting though is the wide range in the quartiles of the yaw angle for the unstable case in comparison to the neutral and stable cases. For example, under convective conditions and for the highly loaded case s_7, the wind turbine yaw angle can change by more than 30°. This is a result of the active mixing that occurs during the convective regime. In contrast, during the neutral and stable regimes, the flow remains more steady with a reduced

requirement for the turbines to continuously readjust with the main wind. As a result, the continuous wake-to-wake interaction is very different between the different stratification regimes.

B. Mean kinetic energy budget analysis

After providing a qualitative description of the flow field for the different study cases, within this section we aim to determine the relationship between the turbines' harvested power, the atmospheric stratification, and the wind farm density. For this reason a local wind turbine MKE budget is performed for all study cases. In this respect, the corresponding MKE budget equation is written as follows:

$$\frac{\partial K}{\partial t} = -\overline{U_j}\frac{\partial K}{\partial x_j} - g\left(\frac{\overline{U_i}\,\overline{\theta}}{\theta_{\text{ref}}}\right)\delta_{i3} + f_c\epsilon_{ij3}\overline{U_i}\,\overline{U_j} - \frac{\overline{U_i}}{\rho}\frac{\partial \overline{P}}{\partial x_i} - \frac{\partial(\overline{\tau}_{ij}\overline{U}_i)}{\partial x_j} + \overline{\tau}_{ij}\frac{\partial \overline{U}_i}{\partial x_j} + \overline{U}_i\overline{f}_i^{\text{wt}}, \quad (1)$$

where K represents the MKE, $K = \frac{1}{2}\overline{U}_i^2 = \frac{1}{2}(\overline{U}^2 + \overline{V}^2 + \overline{W}^2)$, with $\overline{U}$, $\overline{V}$, and $\overline{W}$ being the streamwise, lateral, and vertical mean velocities, respectively, with the overbar denoting the time averaging operation (i.e., for the 4-h study periods; see Fig. 1). The mean pressure is given by $\overline{P}$, and $\overline{f}_i^{\text{wt}}$ represents the force imparted on the flow by the wind turbines. The gravitational constant is denoted by g, $\overline{\theta}$ is the mean temperature, and θ_{ref} is a reference temperature. The Coriolis parameter is denoted by f_c, and ϵ_{ij3} is the alternating unit tensor ($\epsilon_{ij3} = 0$ if $i = j$, and ± 1 otherwise). The sum of the Reynolds and the subgrid-scale (SGS) shear stress is denoted by $\overline{\tau}_{ij}$. Therefore, from left to right the terms of this equation are the storage of MKE, $(\partial\overline{K}/\partial t)$, the advection of MKE, A, the gravitational acceleration, G_a, the energy due to the Coriolis force, C_g, the work due to the pressure gradient, P, the flux of MKE, ϕ, the dissipation of MKE, ϵ, and the power harvested by the wind turbines, P^{WT}. On one side the MKE of the flow is depleted by the turbines and turbulence dissipation, and on the other side, the MKE is replenished by the pressure gradient and the Coriolis force, and transported by the advection and the turbulent flux of MKE. In a steady-state regime, the storage term is null, $(\partial\overline{K}/\partial t = 0)$, and hence the equation can be rewritten as

$$0 = A + G_a + C_g + P + \phi + \epsilon + P^{\text{WT}}, \quad (2)$$

where each term is defined as follows:

$$A = -\overline{U}_j\frac{\partial K}{\partial x_j}, \quad G_a = -g\left(\frac{\overline{U}_i\,\overline{\theta}}{\theta_{\text{ref}}}\right)\delta_{i3}, \quad C_g = f_c\epsilon_{ij3}\overline{U_i}\,\overline{U_j}, \quad P = -\frac{\overline{U}_i}{\rho}\frac{\partial\overline{P}}{\partial x_i},$$
$$\phi = -\frac{\partial(\overline{\tau}_{ij}\overline{U}_i)}{\partial x_j}, \quad \epsilon = \overline{\tau}_{ij}\frac{\partial\overline{U}_i}{\partial x_j}, \quad P^{\text{WT}} = \overline{U}_i\overline{f}_i^{\text{wt}}, \quad (3)$$

with $\overline{\tau}_{ij} = \overline{u_i'u_j'} + \overline{\tau}_{ij}^{\text{SGS}}$ being the sum of the Reynolds and the subgrid-scale shear stress.

1. *Wind farm effective power and wind turbine efficiency*

In the analysis of the different terms, we first focus on the turbine's harvested power ($P^{\text{WT}} = \overline{U}_i\overline{f}_i^{\text{WT}}$). For this purpose, Figs. 6(a) and 6(b) illustrate the wind farm effective power, EP, and the turbine's characteristic efficiency, η_{WT}, defined as

$$EP = \frac{\sum_{i=1}^{N} P_i^{\text{WT}}}{P_{s_1}^{\text{WT}}} \quad \text{and} \quad \eta_{\text{WT}} = \frac{\sum_{i=1}^{N} P_i^{\text{WT}}}{P_{s_1}^{\text{WT}}\,N}. \quad (4)$$

In Eqs. (4), N is the total number of turbines per study case (see Table I), P_i^{WT} denotes the power extracted by the turbines, and $P_{s_1}^{\text{WT}}$ is the corresponding power extracted by case s_1, which is used as a reference for normalization. This last one ($P_{s_1}^{\text{WT}}$) represents the maximum power harvested by a single wind turbine given the forcing conditions. The wind farm EP is a measure of efficiency as a function of wind farm density, illustrating how much power can be extracted by a given wind farm

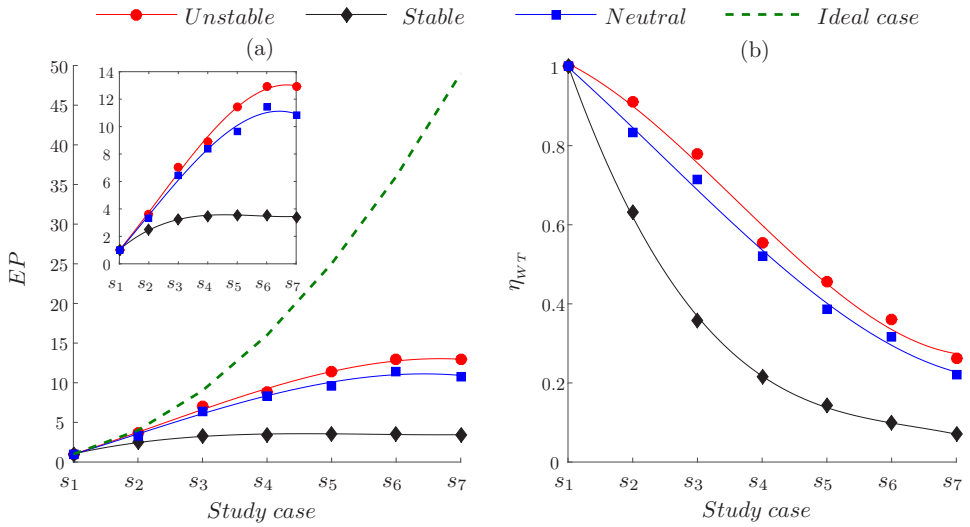

FIG. 6. (a) Effective power (EP) extracted by the wind turbines as a function of the wind farm density. (b) Characteristic efficiency of a wind turbine (η_{WT}) as a function of the wind farm density.

arrangement. For an idealized scenario EP should follow the dashed line represented in Fig. 6(a). Alternatively, the turbine's efficiency (η_{WT}) is a measure of the actual turbines' capacity to effectively harvest wind power, also as a function of farm arrangement. For an ideal case, this variable should be equal to 1, regardless of wind farm density and stratification. In Figs. 6(a) and 6(b) it can be observed that the denser the wind farm is, the larger the departure from the ideal case. For example, for case s_3 the wind farm produces an $EP \approx 7$ during the unstable and neutral regimes, meaning that there is a loss of about 30% in harvested power due to the enhanced wake interactions, a result of the wind farm density. This reduction is indeed much more accentuated for the stable regime, where for the same case s_3, EP reduces to approximately 4, representing a loss of about 60% with respect to the ideal case. From the turbines' efficiency perspective (η_{WT}), a similar behavior is observed in Fig. 6(b) for the stable stratified case, where in case s_3 each turbine only harvests about 35% of what it should if no wake interactions existed. Also of interest are the trends of EP and η_{WT} with increasing farm density and changes in atmospheric stability. For the unstable and neutral stratified cases EP increases quasilinearly with number of turbines up to case s_5, and closely following the ideal case up to case s_3. Furthermore, in case s_6, EP reaches a saturation level, where, regardless of the increase in wind farm density, EP does not increase any more; it even presents a slight decrease in case s_7. For the stable regime, saturation already occurs at s_3. These results strongly suggest that for a large wind farm under stable stratification, it might be better to turn off several turbines such to enhance EP and at the same time reduce turbine structural loads. A similar trend is correspondingly observed in the turbine efficiency [see Fig. 6(b)].

Along a similar line, an earlier experimental work of Hansen *et al.* [15] provided measurements of the power deficit at the Horns Rev wind farm as a function of wind turbine row and also under different atmospheric stability conditions. Their results already showed that the power deficit is strongly dependent on the wind turbine spacing and also concluded that, with increasing turbulence intensity, power deficit would decrease. In their work, the power deficit was presented for four different wind turbine spacings ($7D$, $9.4D$, $10.4D$, and $>20D$) and two different atmospheric stratification regimes. Results for the $10.4D$ turbine spacing case, which correlate well with the s_3 case, showed power deficit values (η_{WT}) of $\sim$0.40 and $\sim$0.70 for the stable and unstable cases, respectively. These results correspond well with the numerical results presented in Fig. 6(b): $\sim$0.37

and ∼0.71, respectively. Also, the $20D$ spacing case, corresponding to an intermediate spacing between cases s_1 and s_2, shows good correspondence, with wind turbine efficiencies ∼0.6 in Hansen *et al.*'s [15] work, and ∼0.63 in the results presented in Fig. 6(b). Finally, for the turbine spacing of $7D$, corresponding to a spacing between cases s_4 and s_5, Fig. 6(b) results overlap well with Hansen *et al.*'s data when accounting for the measured standard deviation. Therefore, it can be concluded that the numerical results approximate well the experimental data. Discrepancies could potentially arise due to the fact that the power deficit in Hansen *et al.*'s [15] work is computed by using the rated power of the wind turbines, contrary to the present analysis where turbine efficiency is derived from the power harvested from the mean flow, and in both cases the average wind velocity is below the rated wind speed. For a more thorough comparison power data should be corrected by using the corresponding turbine power coefficient. Discrepancies could also arise from the large wind farm approximation versus the finite size wind farm case of Hansen *et al.*'s [15] work.

2. MKE budget terms as a function of the wind farm density

This section provides a deeper insight into the other terms of the MKE budget. In this regard, Fig. 7 illustrates the contribution of the different MKE budget terms integrated over the streamwise and spanwise directions of the CV, and averaged over all the turbines of a given wind farm case (i.e., averaged over all the CVs, where the number of CVs is the same as the number of wind turbines for a given case). Notice that the CV approach is fundamental to unveil the corresponding MKE budget terms' behavior for the weakly loaded wind farm cases. Also, it should be noticed that in this case the CV extends from the ground up to a height of $5D$, providing a measure of the MKE redistribution for a characteristic turbine within a given wind farm arrangement as a function of height. This figure illustrates the differentiated behavior in wake recovery between cases s_1, s_3, and s_5.

Whereas for case s_5 [Figs. 7(g)–7(i)] the power harvested by the turbines mainly corresponds to the remaining balance between the MKE dissipation, the turbulent flux of MKE, and the advection of MKE, for the less loaded cases the harvested power is recovered mainly through the remaining balance between MKE dissipation, advection, and pressure redistribution. For the unstable and neutral cases the MKE is mainly recovered by a combination of advection and turbulent flux of MKE [see Figs. 7(a) and 7(b)]. Furthermore, upon closer analysis of all different cases, it is observed that advection and vertical flux of MKE are the dominant terms in the recovery of the wind turbines' harvested power. This trend is maintained equally regardless of stratification, with only small changes in the actual percentages. For example, for case s_1 the advection term represents 51%, 60%, and 73% with respect to the sum of the harvested power and dissipation for the unstable, neutral, and stable regimes, respectively. The same term only represents 35%, 38%, and 9% for case s_5. In this case, however, the turbulent flux of MKE accounts for 43%, 40%, and 26%. As we increase the wind farm density, the contribution of the turbulent flux increases. For example, in case s_7 it accounts for 70%, 85%, and 50%, which is comparable to the contribution of advection in case s_1. Therefore, it is easily concluded that by increasing wind farm density, recovery of MKE within the turbine region evolves from being advection dominated to being vertical flux dominated. From these results it is also interesting to note that while the background atmospheric stratification has a strong effect on the mechanisms to recover MKE within the turbine region for the lightly loaded cases, its effect is much reduced in the more densely packed wind farms. Finally, note that for the lightly loaded scenarios, the budget has a residual of 1.6%, 2.5%, and 1.2% for the unstable, neutral, and stable regimes, respectively, while for case s_5 the residuals decrease except for the stable case, being 1.4%, 1.5%, and 6.8%, with respect to the power extracted by the wind turbines.

In view of these results, it is questioned what would be the error associated if one was only to consider the turbines' harvested power as being replenished by advection and flux of MKE ($P^{\mathrm{WT}} \approx A + \phi$). If this error was found to be small, it could lead to the development of a reduced order model to diagnose the wind farm harvested power given a certain wind farm density and atmospheric stratification. For this purpose, Fig. 8 represents the associated absolute error $\Delta e = |(A + \phi) - P^{\mathrm{WT}}|$ for each study case. This is represented as a function of the wind farm density and

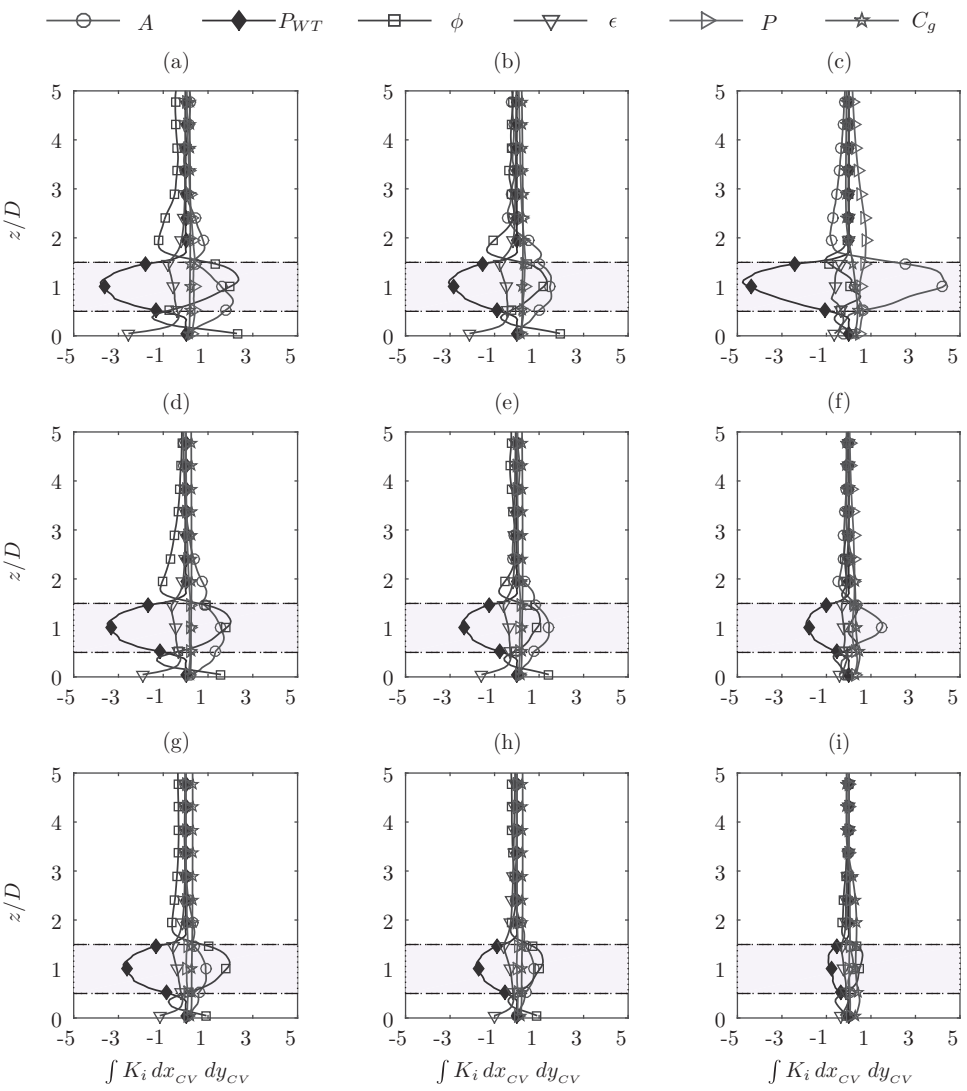

FIG. 7. Vertical profiles of the MKE budget terms (K_i), where index i denotes the different MKE budget terms: (a), (d), (g) the unstable case, (b), (e), (h) the neutral case, and (c), (f), (i) the stable regime. The first row depicts case s_1, the second row depicts case s_3, and the third row case s_5. The shaded area represents the wind turbine rotor disk from $z = 0.5D$ to $z = 1.5D$. The MKE terms are normalized by the wind turbine diameter and the cube of the geostrophic wind and, consequently, the values of the x axis should be scaled by a factor of 1×10^{-3}.

for the different atmospheric stratification conditions [unstable, neutral, and stable in Figs. 8(a), 8(b), and 8(c), respectively]. Results show small errors for the unstable and neutral cases, the largest error being equal to 0.2×10^{-3} (corresponding to a relative error of 10%), and 0.25×10^{-3} (corresponding to a relative error of 30%) for the neutral case. The stable case presents the largest errors, with a value of 0.6×10^{-3} in case s_2, corresponding to a relative error of 38%. These larger errors present in the stable case are the result of the contribution of the pressure and dissipation terms, which are

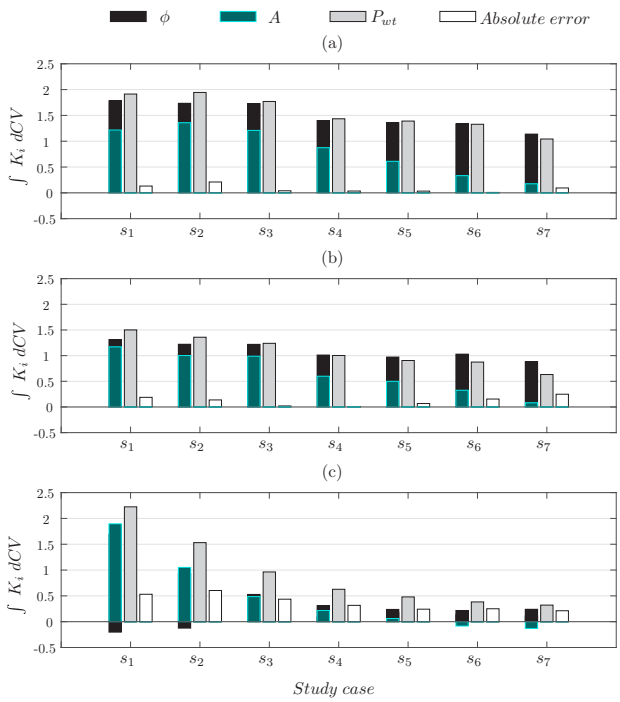

FIG. 8. Bar representation of the integration over the CV of the terms contributing to the recovery of the wind turbine power extraction (advection A and flux of MKE, ϕ, in green and black, respectively), next to the bar representation of the wind turbine power extraction (P^{WT}) in light grey. The white bar represents the absolute error $\epsilon = |(A+\phi) - P^{\mathrm{WT}}|$. (a) Unstable, (b) neutral, and (c) stable cases. The vertical axis should be scaled by a factor of 1×10^{-3}.

also important in the overall MKE budget. Despite this singular behavior of the stable case, it seems fair to assume on a first-order analysis that $P^{\mathrm{WT}} \approx A + \phi$ is a good approximation. Note that each MKE budget term depicted in Fig. 8 represents the integration of the respective term within the CV ($\int K_i\, dCV$), which now extends from $z = D/4$ to $z = 2D$ to only capture the main mechanisms that contribute to the recovery of the power extracted by the turbines.

In next section this approximation is used to develop a first order parametrization for the wind farms' harvested power as a function of the farm's density and atmospheric stratification.

V. LOW-ORDER MODEL FOR WIND FARMS' HARVESTED POWER

Upon analysis of the MKE budget presented in the previous section, as well as from earlier results [6], it seems that as a first-order approximation the wind farms' harvested power is mainly recovered through a combination of advection and flux of MKE. Therefore, one could envision an expression of the type

$$P_i \approx \lambda A_1 + (1-\lambda)\phi_N, \tag{5}$$

where P_i is the average wind turbine harvested power for any given wind farm density, i. Furthermore, A_1 is the advection term corresponding to a lone standing wind turbine (case s_1) and ϕ_N is the flux of MKE for the most intensely loaded wind farm case (s_7). In this approach, A_1 and ϕ_N represent the two most extreme values for advection and MKE flux given a geostrophic forcing. To express the

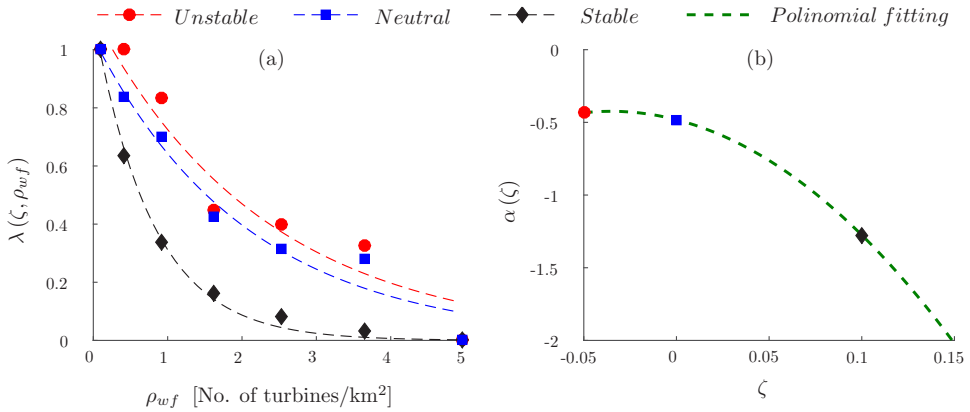

FIG. 9. (a) The weighting parameter, $\lambda(\zeta, \rho_{\text{wf}})$, as a function of the wind farm density (in units of number of wind turbines per unit surface, square kilometer) for the different atmospheric stability conditions. The dashed lines are fittings of the exponential function from Eq. (7). (b) The stability correction exponent as a function of the atmospheric stability. The fitting is performed using a second-order polynomial $\alpha(\zeta) = a\zeta^2 + b\zeta + c$, with the corresponding coefficients $a = -47$, $b = -3.3$, and $c = 0.48$.

mutual relationship between the three terms (power, advection, and flux of MKE), the parameter λ is a "weighting coefficient" that redistributes the corresponding weight to either advection or flux of MKE. Hence, when $\lambda = 1$, all the harvested power is recovered through advection of MKE, and when $\lambda = 0$ the recovery occurs solely through the vertical flux of MKE. Therefore, the rate of change between the advection of MKE (A_i) and the MKE flux (ϕ_i) is determined by the weighting parameter (λ), with the assumption that both together replenish the depleted MKE ($P^{\text{WT}} \approx A + \phi$). From the results, it is further evident that parameter λ should be a function of wind farm density (ρ_{wf}) and atmospheric stratification, represented here by $\zeta = z_1/\langle L \rangle_{xy}$; thus, $\lambda = \lambda(\zeta, \rho_{\text{wf}})$. Therefore, Eq. (5) provides an approximate value of a turbine's harvested power (P_i) given a wind farm density and an atmospheric thermal stratification. Because, in practice, the integral of the MKE budget terms within a CV surrounding a wind turbine is not a readily available value, two additional approximations can be performed. Next, it is further assumed that all the power depleted by a stand-alone wind turbine is equal to the advection term ($P_1 \approx A_1$), and that in a highly loaded case it is equal to the vertical flux ($P_N \approx \phi_N$). As a result, Eq. (5) can be rewritten as

$$P_i \approx \lambda P_1 + (1 - \lambda) P_N. \tag{6}$$

Note that P_1 and P_N are both functions of the atmospheric stratification, $P_1(\zeta)$ and $P_N(\zeta)$. On one end P_1 can be determined by the on-site flow velocity, and P_N is the turbine power for which the EP is maximized, which in practice is equal to the wind turbine power extracted when it is located in an extremely dense wind farm scenario. Here, P_1 is the power extracted by the stand-alone wind turbine (case s_1) and P_N is the power extracted by the wind turbine from case s_7. Note that for realistic wind farm applications, the problem can be further reduced by writing P_N as a function of P_1, where P_N represents a certain percentage of P_1. In Fig. 9(a) the parameter λ is represented as a function of the wind farm density ($\rho_{\text{wf}} = N/A_s$, where N is the number of wind turbines that enclose the wind farm and A_s is the surface extension of the wind farm) and for the different atmospheric stability conditions. From the numerical results an exponential fitting for λ is adjusted, represented in Fig. 9(a) by the dashed lines, and expressed as follows:

$$\lambda(\zeta, \rho_{\text{wf}}) = C_o \, \exp(\alpha \, \rho_{\text{wf}}), \tag{7}$$

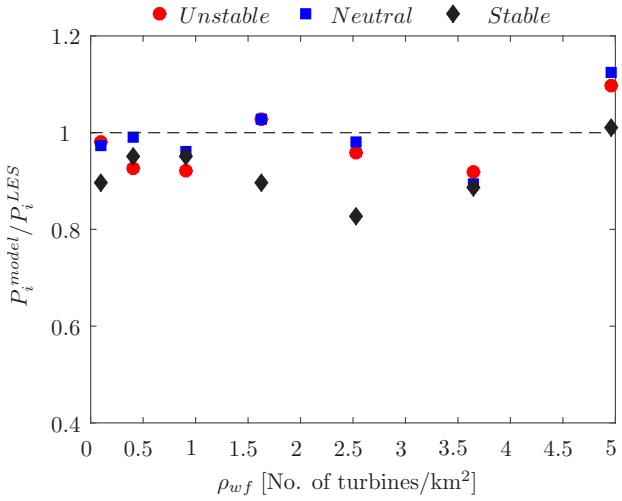

FIG. 10. Representation of the power ratio $P_i^{\text{model}}/P_i^{\text{LES}}$ as a function of the wind farm density (ρ_{wf}) in units of wind turbines per square kilometer. The variable P_i^{model} is the power obtained by the low-order model and P_i^{LES} is the power computed within the LESs; the index i denotes the different wind farm density cases (from $i = 1$ to $i = 7$).

where C_o is an adjustment coefficient and α is a stability correction exponent. In the three different fittings from Fig. 9(a), and for the sake of simplicity, C_o is taken equal to 1. The parameter α is called the stability correction exponent and it is represented in Fig. 9(b) as a function of the atmospheric stratification (ζ). It is shown that a different stability correction exponent is obtained for each corresponding stratification scenario considered. In the ideal case we could have run a larger set of stratification regimes, one could have filled additional points in Fig. 9(b). Given that this is not the case, we use the three α values we have available to fit a polynomial curve [$\alpha(\zeta) = a\zeta^2 + b\zeta + c$] that determines α as a function of the background atmospheric stratification. Because fitting a curve based on three points is far from ideal, in the next section we explore the sensitivity of hypothetical variations in α.

In summary, it can be concluded that from the curves provided in Figs. 9(a) and 9(b), it is hence possible to estimate in a first-order approximation the wind farms' harvested power given a wind farm density and given an atmospheric stability. For example, given a certain atmospheric stability, ζ, it is possible to extract the corresponding stability correction exponent, α, which in combination with ρ_{wf} provides a value for the λ parameter through Eq. (7). Next, using the parametrized power values for the two extreme cases, P_1 and P_N, in conjunction with Eq. (6), one obtains a value for the wind turbine's harvested power in a wind farm case i.

VI. ERROR ESTIMATION AND SENSITIVITY ANALYSIS FOR THE LOW-ORDER MODEL

A. Error estimation of the low-order model

In this section, the error committed when using the low-order model is evaluated by using the large-eddy simulations as a benchmark. Thus, Fig. 10 represents the power ratio $P_i^{\text{model}}/P_i^{\text{LES}}$, in the ordinate axis, and the wind farm density (ρ_{wf}) in the abscissa. The variable P_i^{model} is the power obtained by the low-order model [using Eqs. (6) and (7)] and P_i^{LES} is the power computed with the LES. The different markers denote the different atmospheric stratifications evaluated as a function of the different wind farm densities, and the horizontal solid line represents the null error with respect to the LES data.

It can be observed that the error that the model contributes varies as a function of the stability and wind farm density. On average, the overall relative error is 6%, 5%, and 8% for the unstable, neutral, and stable cases, correspondingly, where the relative error can be computed as $e = |(1 - (P_i^{\text{model}}/P_i^{\text{LES}})| \times 100)$. The maximum relative error is of the order of 10–12% for the unstable and neutral regimes, and around 17% for the stable stratified cases. Overall, the errors resultant of this parametrization are quite small, being able to predict with a good accuracy the amount of power that could be extracted from a given wind farm density under a given atmospheric stability. Again, from Fig. 10 it is demonstrated that the neutral and unstable cases have a much better predictability of the power output than the stable cases.

B. Sensitivity analysis and error propagation

In this section, and for the sake of discussion, a sensitivity analysis is performed regarding α and its effect on λ. Thus, using propagation of error theory [49], we evaluate the error committed in computing P_i given a certain uncertainty in the stability correction exponent ($\delta\alpha$). The wind turbine power uncertainty (δP_i) is based on the uncertainty in the parameter λ, which at the same time is a function of the stability correction exponent (α). Thus,

$$\delta P_i = \left.\frac{\partial \mathcal{F}_1}{\partial \lambda}\right|_{\overline{\lambda}} \delta\lambda, \tag{8}$$

where $\mathcal{F}_1 = \lambda P_1 + (1 - \lambda) P_N$, which yields the final equation for the uncertainty in the harvested power, $\delta P_i = (P_1 - P_N)\delta\lambda$. In this fashion, the associated error on λ given a small variation on alpha ($\delta\alpha$) is written as

$$\delta\lambda = \left.\frac{\partial \mathcal{F}_2}{\partial \lambda}\right|_{\overline{\alpha}} \delta\alpha. \tag{9}$$

In this expression $\mathcal{F}_2 = \exp(\alpha\rho_{\text{wf}})$, which leads to $\delta\lambda = \rho_{\text{wf}} \exp(\alpha\rho_{wf})\delta\alpha$. Finally, assuming $\delta\alpha = 10\%$, an average power error of $e_P \approx 2\%$, $\approx$3%, and $\approx$5% will result for the unstable, neutral, and stable cases, correspondingly, where the relative uncertainty has been obtained by computing $e_P = \delta P_i / \overline{P_i}$ for the different stratifications and wind farm densities.

VII. SUMMARY AND CONCLUSIONS

This work presents an LES study of wind turbine wake recovery processes as a function of wind farm density and atmospheric stratification. For this purpose the CV approach of Cortina *et al.* [6] has been used to characterize in detail the MKE recovery processes and turbines' harvested power.

Results illustrate that the turbines' harvested power is mainly recovered by two main dominant mechanisms, advection and flux of mean kinetic energy. These two MKE recovery mechanisms are modulated by the background thermal stratification and are dependent on the wind farm density. Specifically, it has been shown that for the low-density arrangements advection dominates, while for the highly loaded wind farms the mean kinetic energy recovers through fluxes of mean kinetic energy. Of relevance from this work is the fact that for the intermediate-density cases results illustrate a smooth transition between both mechanisms. Results further illustrate that when advection dominates, the wind farm tends to be more efficient than when the MKE flux recovery dominates. Also, under stable conditions, harvested power in dense wind farms is strongly penalized due to the lack of mixing mechanisms. The results obtained on wind farm efficiency are compared with the experimental data of Hansen *et al.* [15], illustrating strong agreement.

Finally, from the LES data a low-order model for the wind farms' harvested power as a function of thermal stratification and wind farm density has been developed. This model predicts, with relatively small errors (5–15%), the power that a given wind farm under a given stability stratification could harvest. The main simplification assumption intrinsic to this model is the fact that the MKE harvested by the turbines is only recovered by advection and vertical flux. Therefore, in a first-order

approximation the contribution of the remaining MKE budget terms is neglected. Based on the experimental data, the model further assumes an equilibrium between advection and vertical flux controlled by a weighting function that depends on the wind farm density and the background thermal stratification [$\lambda = \lambda(\zeta, \rho_{wf})$], for which an experimental relationship is provided. Results show that the model works best under unstable and neutral atmospheric stratifications. Under stable regimes, the pressure distribution term also plays a relevant role in the wind turbine wakes' recovery process, hence producing larger divergences in the results from the model. This simple model has the potential to be employed as an order-of-magnitude estimation tool, which could help quickly determine the number of wind turbines that should be disconnected to optimize the harvested power provided a time changing background stratification.

ACKNOWLEDGMENTS

This research has been supported with the startup funds provided by the Mechanical Engineering Department at University of Utah to M.C. The support and resources from the Center for High Performance Computing at the University of Utah are gratefully acknowledged. V.S. thanks the support received through the Swiss National Science Foundation (Projects No. 200021134892/1 and No. 20020 125092), ETH Domain Centre for Competence in Environmental Sustainability, and the NSERC Discovery Grant (MBP) Scientific IT and Application Support (SCITAS) group at EPFL.

[1] *Renewable Energy Technologies: Cost Analysis Series* (International Renewable Energy Agency, Abu Dhabi, UAE, 2012), Vol. 1.

[2] C. Mon, T. Stehly, B. Maples, and E. Settle, 2014 cost of wind energy review, National Renewable Energy Laboratory, Report No. NREL/TP-6A20-64281, 2014.

[3] S. Rockel, J. Peinke, M. Hölling, and R. B. Cal, Wake to wake interaction of floating wind turbine models in free pitch motion: An eddy viscosity and mixing length approach, Renew. Energy **85**, 666 (2016).

[4] V. Sharma, M. B. Parlange, and M. Calaf, Perturbations to the spatial and temporal characteristics of the diurnally-varying atmospheric boundary layer due to an extensive wind farm, Boundary-Layer Meteorol. **162**, 255 (2017).

[5] S. Lee, M. Churchfield, P. Moriarty, J. Jonkman, and J. Michalakes, Atmospheric and wake turbulence impacts on wind turbine fatigue loadings, in *Proceedings of the 50th AIAA Aerospace Sciences Meeting Including the New Horizons Forum and Aerospace Exposition* (American Institute of Aeronautics and Astronautics, Reston, VA, 2012), p. 540.

[6] G. Cortina, M. Calaf, and R. B. Cal, Distribution of mean kinetic energy around an isolated wind turbine and a characteristic wind turbine of a very large wind farm, Phys. Rev. Fluids **1**, 074402 (2016).

[7] R. J. A. M. Stevens, Dependence of optimal wind turbine spacing on wind farm length, Wind Energy **19**, 651 (2016).

[8] R. J. A. M. Stevens, B. F. Hobbs, A. Ramos, and C. Meneveau, Combining economic and fluid dynamic models to determine the optimal spacing in very large wind farms, Wind Energy **20**, 465 (2017).

[9] X. Yang, S. Kang, and F. Sotiropoulos, Computational study and modeling of turbine spacing effects in infinite aligned wind farms, Phys. Fluids **24**, 115107 (2012).

[10] V. Sharma, G. Cortina, F. Margairaz, M. B. Parlange, and M. Calaf, Evolution of flow characteristics through finite-sized wind farms and influence of turbine arrangement (unpublished).

[11] R. J. Stevens, D. F. Gayme, and C. Meneveau, Effects of turbine spacing on the power output of extended wind-farms, Wind Energy **19**, 359 (2016).

[12] J. Meyers and C. Meneveau, Optimal turbine spacing in fully developed wind farm boundary layers, Wind Energy **15**, 305 (2012).

[13] M. Calaf, C. Meneveau, and J. Meyers, Large eddy simulation study of fully developed wind-turbine array boundary layers, Phys. Fluids **22**, 015110 (2010).

[14] E. Son, S. Lee, B. Hwang, and S. Lee, Characteristics of turbine spacing in a wind farm using an optimal design process, Renew. Energy **65**, 245 (2014).

[15] K. S. Hansen, R. J. Barthelmie, L. E. Jensen, and A. Sommer, The impact of turbulence intensity and atmospheric stability on power deficits due to wind turbine wakes at Horns Rev wind farm, Wind Energy **15**, 183 (2012).

[16] A. C. Fitch, J. K. Lundquist, and J. B. Olson, Mesoscale influences of wind farms throughout a diurnal cycle, Mon. Weather Rev. **141**, 2173 (2013).

[17] W. Zhang, C. D. Markfort, and F. Porté-Agel, Wind-turbine wakes in a convective boundary layer: A wind-tunnel study, Boundary-Layer Meteorol. **146**, 161 (2013).

[18] M. Abkar and F. Porté-Agel, The effect of free-atmosphere stratification on boundary-layer flow and power output from very large wind farms, Energies **6**, 2338 (2013).

[19] M. Abkar and F. Porté-Agel, Influence of atmospheric stability on wind-turbine wakes: A large-eddy simulation study, Phys. Fluids **27**, 035104 (2015).

[20] A. Peña and O. Rathmann, Atmospheric stability-dependent infinite wind-farm models and the wake-decay coefficient, Wind Energy **17**, 1269 (2014).

[21] A. Peña, P.-E. Réthoré, and O. Rathmann, Modeling large offshore wind farms under different atmospheric stability regimes with the park wake model, Renew. Energy **70**, 164 (2014), special issue on aerodynamics of offshore wind energy systems and wakes.

[22] A. Peña, P.-E. Réthoré, and M. P. van der Laan, On the application of the Jensen wake model using a turbulence-dependent wake decay coefficient: The Sexbierum case, Wind Energy **19**, 763 (2016).

[23] K. Bhaganagar and M. Debnath, Implications of stably stratified atmospheric boundary layer turbulence on the near-wake structure of wind turbines, Energies **7**, 5740 (2014).

[24] K. Bhaganagar and M. Debnath, The effects of mean atmospheric forcings of the stable atmospheric boundary layer on wind turbine wake, J. Renew. Sustainable Energy **7**, 013124 (2015).

[25] M. Abkar, A. Sharifi, and F. Porté-Agel, Wake flow in a wind farm during a diurnal cycle, J. Turbul. **17**, 420 (2016).

[26] W. El-Askary, I. Sakr, A. M. AbdelSalam, and M. Abuhegazy, Modeling of wind turbine wakes under thermally-stratified atmospheric boundary layer, J. Wind Eng. Ind. Aerodyn. **160**, 1 (2017).

[27] R. J. Stevens and C. Meneveau, Flow structure and turbulence in wind farms, Annu. Rev. Fluid Mech. **49**, 311 (2017).

[28] M. Méchali, R. Barthelmie, S. Frandsen, L. Jensen, and P.-E. Réthoré, Wake effects at Horns Rev and their influence on energy production, in *Proceedings of the European Wind Energy Conference and Exhibition* (CiteSeer, 2006).

[29] M. Harris, D. Bryce, A. Coffey, D. Smith, J. Birkemeyer, and U. Knopf, Advance measurements of gusts by laser anemometry, Wind Eng. Ind. Aerodyn. **95**, 1637 (2007).

[30] K. Kragh, M. Hansen, and T. Mikkelsen, Improving yaw alignment using spinner based lidar, in *Proceedings of 49th AIAA Aerospace Sciences Meeting Including the New Horizons Forum and Aerospace Exposition* (American Institute of Aeronautics and Astronautics, Orlando, FL, 2011), paper 2011-264.

[31] E. Simley, L. Pao, R. Frehlich, B. Jonkman, and N. Kelley, Analysis of wind speed measurements using continuous wave lidar for wind turbine control, in *Proceedings of the 49th AIAA Aerospace Sciences Meeting Including the New Horizons Forum and Aerospace Exposition* (American Institute of Aeronautics and Astronautics, Orlando, FL, 2011), paper 2011-263.

[32] G. Iungo, W. Yu-Ting, and F. Porté-Agel, Field measurements of wind turbine wakes with lidars, J. Atmos. Ocean. Technol. **30**, 274 (2012).

[33] K. Kragh and P. Fleming, Rotor speed dependent yaw control of wind turbines based on empirical data, in *Proceedings of the 50th AIAA Aerospace Sciences Meetings and Exhibit* (American Institute of Aeronautics and Astronautics, Nashville, Tennessee, 2012), paper 2012-1018.

[34] T. Mikkelsen, N. Angelou, K. Hansen, M. Sjöholm, M. Harris, C. Slinger, P. Hadley, R. Scullion, G. Ellis, and G. Vives, A spinner-integrated wind lidar for enhanced wind turbine control, Wind Energy **16**, 625 (2013).

[35] G. Cortina, V. Sharma, and M. Calaf, Investigation of the incoming wind vector for improved wind turbine yaw-adjustment under different atmospheric and wind farm conditions, Renew. Energy **101**, 376 (2017).

[36] G. Cortina and M. Calaf, Turbulence upstream of wind turbines: A large-eddy simulation approach to investigate the use of wind lidars, Renew. Energy **105**, 354 (2017).

[37] P. A. Fleming, P. M. O. Gebraad, S. Lee, J. W. van Wingerden, K. Johnson, M. Churchfield, J. Michalakes, P. Spalart, and P. Moriarty, Evaluating techniques for redirecting turbine wakes using SOWFA, Renew. Energy **70**, 211 (2014).

[38] P. M. O. Gebraad and J. W. van Wingerden, A control-oriented dynamic model for wakes in wind plants, J. Phys.: Conf. Ser. **524**, 012186 (2014).

[39] M. J. Churchfield, P. Fleming, B. Bulder, and S. M. White, Wind turbine wake-redirection control at the fishermen's atlantic city windfarm, National Renewable Energy Laboratory, Report No. NREL/CP-5000-63575, 2015.

[40] R. B. Cal, J. Lebrón, L. Castillo, H. S. Kang, and C. Meneveau, Experimental study of the horizontally averaged flow structure in a model wind-turbine array boundary layer, J. Renew. Sustainable Energy **2**, 013106 (2010).

[41] C. VerHulst and C. Meneveau, Altering kinetic energy entrainment in large eddy simulations of large wind farms using unconventional wind turbine actuator forcing, Energies **8**, 370 (2015).

[42] R. Stull, *An Introduction to Boundary Layer Meteorology*, Atmospheric Science Library (Springer, Berlin, 1988).

[43] G. S. Poulos, W. Blumen, D. C. Fritts, J. K. Lundquist, J. Sun, S. P. Burns, C. Nappo, R. Banta, R. Newsom, J. Cuxart, E. Terradellas, B. Balsley, and M. Jensen, CASES-99: A comprehensive investigation of the stable nocturnal boundary layer, Bull. Am. Meteorol. Soc. **83**, 555 (2002).

[44] V. Sharma, M. Calaf, M. Lehning, and M. B. Parlange, Time-adaptive wind turbine model for an LES framework, Wind Energy **19**, 939 (2016).

[45] M. Magnusson and A.-S. Smedman, Influence of atmospheric stability on wind turbine wakes, Wind Eng. **18**, 139 (1994).

[46] L. P. Chamorro and F. Porté-Agel, A wind-tunnel investigation of wind-turbine wakes: Boundary-layer turbulence effects, Boundary-Layer Meteorol. **132**, 129 (2009).

[47] L. P. Chamorro and F. Porté-Agel, Effects of thermal stability and incoming boundary-layer flow characteristics on wind-turbine wakes: A wind-tunnel study, Boundary-Layer Meteorol. **136**, 515 (2010).

[48] R. J. Barthelmie and L. E. Jensen, Evaluation of wind farm efficiency and wind turbine wakes at the Nysted offshore wind farm, Wind Energy **13**, 573 (2010).

[49] H. H. Ku, Notes on the use of propagation of error formulas, J. Res. Natl. Bur. Stand. Sect. C **70C**, 263 (1996).

CHAPTER 6

CONCLUSIONS

The research presented in this document has focused on creating new understanding about the mechanisms of interaction between wind farms and the atmospheric boundary layer to help developing more efficient wind energy harvesting systems. In detail, the objectives that have been achieved within this work are: (i) development of new understanding regarding wind turbines' inflow conditions as they relate to optimal time alignment of the turbines; (ii) determination of the dominant turbine wake recovery processes under different atmospheric stratification conditions; (iii) development of an analytical predictor model to estimate large scale wind farms power output as a function of the wind farm density and atmospheric stability. These objectives have been accomplished by means of high-resolution numerical simulations of the atmospheric boundary layer, also resolving the wind turbines. Next, the most relevant conclusions of this work are summarized.

The main goals of the second and third chapters were to investigate the possible existence of an optimal upstream scanning distance and readjustment-time to accurately learn about the incoming wind vector and turbulence when using wind LIDARs mounted on the wind turbine's nacelle. To answer this question, we considered the canonical scenarios of a very large wind farm, and a largely spaced wind farm, or equivalently seen as a single wind turbine, under continuously changing atmospheric conditions. The numerical results of two consecutive diurnal cycles revealed that during unstable regimes, as a result of the enhanced vertical and lateral mixing, there exists a larger variation in the incoming wind vector angle compared to the stable period. However, results revealed no significant differences when measuring the incoming wind vector at different upstream distances, regardless of the atmospheric stratification. This is a very important result because it will allow wind LIDARs to learn about the incoming wind vector at far upstream distances, hence providing longer readjustment times to change turbine setups. In this study, each

wind turbine was independently controlled by a wind LIDAR. However, wind LIDARs represent a large portion of the overall wind turbine cost. At the same time, results demonstrated no significant differences in alignment among the different upstream distances, and no major differences were observed between the alignments of the different wind turbines configuring the wind farm. Consequently, in a future work, it would be interesting to investigate if the strategical installation of wind LIDARs in one or several wind turbines could help forecast the wind vector for the entire farm. In light of these results, another line of future research could be the study of using wind LIDARs to develop better anemometer and wind vane transfer functions. The transfer functions are corrections applied to the wind turbine anemometer and wind vane to properly measure the wind vector. By using wind LIDARs mounted at the top of the nacelle during a certain time period, *i.e.*, one year, different corrections could be determined as a function of the on-site atmospheric stability and wind farm configuration.

In a second stage, we studied the effectiveness in measuring incoming turbulence by wind LIDARs mounted on the turbine's nacelle. Results illustrated that when the upstream scanning distance is increased the probability with which turbulence can be confidently predicted substantially decreases. Minimum turbulence correlations were observed for the furthest evaluated upstream distance (200 m), and maximum correlations were observed when measuring at the closest distance (25 m). Interestingly, a quasi linear decay in the maximum correlation value was observed for the different upstream scanning distances. At all upstream scanning distances, stronger correlations were observed during the convective regimes, when turbulence levels are much more intense and sustained in time, in comparison to stable cases; note that this plays in favor of using wind LIDAR technology to timely learn about incoming strong turbulent events. We concluded that the upstream scanning distance should always be chosen the shortest possible in relation to the wind turbine reaction time (time to feather the wind turbine blades). In this regard, the use of wind LIDARs to forecast the wind direction and wind gusts can be further optimized depending on the wind turbine inflow velocity. In other words, the wind turbine power curve illustrates three important characteristic velocities: the cut-in speed, the rated speed and the cut-out speed. When wind speeds range between the cut-in and the rated wind speed is when wind LIDARs could be optimized to help to determine the

proper yaw adjustment. Within this region, wind velocities range approximately from 3 to 12 m/s, and thus a small change in wind velocity corresponds to a large change in power output. Hence, the yaw-alignment plays an important role in order to minimize the loss in harvested energy, and for this reason, a proper wind turbine yaw-alignment is crucial within this region of the power curve. The region between the rated wind speed and the cut-out speed (where velocities range from 12 to 25 m/s) is when wind LIDARs have to be optimized to predict the incoming wind gusts, since a better yaw-alignment will not imply larger power outputs and velocity aberrations would be more intense.

In a second step, we have developed a model for predicting the wind turbine's incoming turbulence, based on a truncated normal probability distribution function to provide a measure of the correlation between the incoming turbulence and that measured at the turbine's rotor-disk. By modelling the turbulent correlations, it is now possible to help decide the best upstream scanning distance to learn about the incoming turbulence, and to determine the time at which the turbine settings should be modified to minimize structural loading. Finally, results have shown that upstream scanning distances should always be chosen the shortest possible in relation to the wind turbine reaction time. The best turbulent correlations are measured during unstable periods, which is very important because it is when the largest turbulent events occur. During stable periods, turbulence is generally weak, or sporadic and intense, and foreseeing incoming turbulence remains a challenge.

In Chapter 4, we applied a control volume analysis technique to allow evaluating the budget of mean kinetic energy in very different scenarios, such as in the surroundings of an isolated wind turbine or in the surroundings of a wind turbine located in a very large wind farm. In Chapter 5, the control volume technique has been used to study the wind turbine wake recovery processes as a function of wind farm density and atmospheric stratification. With the main goal of developing a power predictor model that accounts for different wind farm densities and atmospheric stability conditions. Results illustrated that the turbines' harvested power is mainly recovered by two dominant mechanisms, advection and flux of mean kinetic energy. It has been shown that these two MKE recovery mechanisms are modulated by the background thermal stratification and are dependent on the wind farm density. Specifically, it has been shown that for the low-density arrangements advection

dominates, while for the highly-loaded wind farms the MKE recovers through the vertical fluxes. Of relevance from this work is the fact that for the intermediate density cases results illustrate a smooth transition between both mechanisms. Later results have also shown that this balance can also apply in finite size wind farms, where in the first rows of wind turbines advection dominates. On the other hand, further downstream in the wind farm the flux of MKE is the mechanism that dominates the wake recovery. Since the MKE redistribution within the wind turbine array boundary layer has been shown to be dependent on the arrangement of the wind turbines, next, it would be interesting to numerically investigate how the MKE is redistributed on finite size wind farms for different atmospheric stratification conditions. One of the most important findings would be to uncover how this transition between both MKE transport mechanisms, from advection dominated to flux dominated, would change depending on the atmospheric stratification and as a function of the wind farm length. This could help to estimate the optimal wind farm length depending on the atmospheric stratification, or could reveal the fact that most optimal wind farm designs would have to change the spacing between turbines as a function of the wind farm length, *i.e.*, where the first rows of wind turbines will have small streamwise spacing that will need to be exponentially increased for downstream rows of turbines in order to keep a proper MKE balance that would maximize the overall wind farm power output. Finally, with the LES data we have developed a low-order model for the wind farms' harvested power as a function of thermal stratification and wind farm density. This new model predicts, with relatively small errors (5% - 15%), the power that a given wind farm under a given stability stratification could harvest. The main simplification assumption intrinsic to this new model is the fact that the MKE harvested by the turbines is only recovered by advection and vertical flux. Therefore, in a first-order approximation the contribution of the remaining MKE budget terms is neglected. This simple model has the potential to be employed as an order of magnitude estimation tool, which could help quickly determine the number of wind turbines that should be disconnected to optimize the harvested power provided a time changing background stratification. The research proposed in this document sought new understanding and findings where current literature was lacking. To achieve the goal of the project we dedicated much of our efforts to develop new knowledge on the turbulent atmospheric

flow and its interaction with arrays of wind turbines. This work strived to fill the gaps of the current understanding on the capabilities of a new technology to better control the settings of the wind turbines by learning from the upstream inflow conditions, and at the same time, this work strived to improve the wind energy harvesting process to increase wind farms' power output, and thus, their overall efficiency.

Finally, I would like to note that LES still remains a computationally expensive tool, with current use limited to academia and research groups. Therefore, it is of capital relevance to keep developing alternative simplified approaches (such as low-order models) that can provide accurate results at a much lower numerical cost.